Magnetothermal Multiplexing for Biomedical Applications

by

Michael G. Christiansen

B.S. Physics, Arizona State University, 2012

Submitted to the Department of Materials Science and Engineering
in Partial Fulfillment of the Requirements for the Degree of

Doctor of Philosophy

at the

MASSACHUSETTS INSTITUTE OF TECHNOLOGY

June 2017

Signature of Author……
Department of Materials Science and Engineering
May 25, 2017

Certified by……
Polina Anikeeva
Professor of Materials Science and Engineering
Thesis Advisor

Certified by……
Donald R. Sadoway
Chairman, Department Committee on Graduate Students

Magnetothermal Multiplexing for Biomedical Applications

by

Michael G. Christiansen

Submitted tot eh Department of Materials Science and Engineering
on May 25, 2017 in Partial Fulfillment of the Requirements for the Degree of
Doctor of Philosophy in Materials Science and Engineering

ABSTRACT

Research on biomedical applications of magnetic nanoparticles (MNPs) has increasingly sought to demonstrate noninvasive actuation of cellular processes and material responses using heat dissipated in the presence of an alternating magnetic field (AMF). By modeling the dependence of hysteresis losses on AMF amplitude and constraining AMF conditions to be physiologically suitable, it can be shown that MNPs exhibit uniquely optimal driving conditions that depend on controllable material properties such as magnetic anisotropy, magnetization, and particle volume. "Magnetothermal multiplexing," which relies on selecting materials with substantially distinct optimal AMF conditions, enables the selective heating of different kinds of collocated MNPs by applying different AMF parameters. This effect has the potential to extend the functionality of a variety of emerging techniques with mechanisms that rely on bulk or nanoscale heating of MNPs. Experimental investigations on methods for actuating deep brain stimulation, drug release, and shape memory polymer response are summarized, with discussion of the feasibility and utility of applying magnetothermal multiplexing to similar systems. The possibility of selective heating is motivated by a discussion of various models for heat dissipation by MNPs in AMFs, and then corroborated with experimental calorimetry measurements. A heuristic method for identifying materials and AMF conditions suitable for multiplexing is demonstrated on a set of iron oxide nanoparticles doped with various concentrations of cobalt. Design principles for producing AMFs with high amplitude and ranging in frequency from 15kHz to 2.5MHz are explained in detail, accompanied by a discussion of the outlook for scalability to clinically relevant dimensions. The thesis concludes with a discussion of the state of the field and the broader lessons that can be drawn from the work it describes.

Thesis Supervisor: Polina Anikeeva
Title: Professor of Materials Science and Engineering

Contents

Acknowledgements

I am often struck by how profoundly lucky I have been, particularly when I think of the many individuals, both past and present, who have helped me. Whenever I reflect back upon their many lessons, assistance, and acts of kindness, I am overwhelmed by a deep and abiding sense of gratitude. I owe an inestimable debt to these people, including not only those who have helped me throughout the work represented in this thesis, but also the many others who put me on a path toward it.

I first wish to acknowledge my advisor, Prof. Polina Anikeeva, for the opportunities and impetus she provided to develop not only my skills as a scientist, but also to cultivate resilience and fortitude. I have grown tremendously in my time at MIT and I am grateful for the role she has played in that.

I would like to thank all of my colleagues within the Bioelectronics Group for their support, particularly those among the magnetics subgroup with whom I worked most frequently, including Dr. Ritchie Chen, Dr. Danijela Gregurec, Junsang Moon, and Alexander Senko. I feel especially indebted to Dr. Gabriela Romero Uribe, from whose instruction, prodigious skill, moral support, and quiet example I greatly benefited. It was gratifying to work so productively together during her brief time at MIT.

Working with highly capable and conscientious undergraduates was a deeply rewarding and mutually instructive experience, and often a source of personal friendship that outlasted projects or internships. I am especially grateful to Christina Howe, Ligia Stocche Barbosa, Colleen Loynachan, Francisco Garcia, Michelle Qui, Albert Okundaye, and Christopher DeCola.

I have been fortunate enough engage in productive collaborations with researchers from outside the MIT Bioelectronics Group. Working with Dr. Simone Schürle and Jaideep Dudani on magnetically actuated protease sensors was a source of great intellectual and personal enjoyment. I consider myself exceptionally privileged that our paths intersected. I wish to also acknowledge Prof. Qi "Kevin" Ge of the Singapore University of Technology and Design, who has consistently amazed us all with his remarkably beautiful 3D printed structures since we began collaborating. Our guests from the Netherlands, Dr. Sarah Hescham and Dr. Milaine Roet, came to MIT for a difficult experiment that required me to scale up alternating magnetic field setups in ways that I was unsure were even feasible. I admire their determination and hope they are able to carry on the work we started together.

The electronics work represented in this thesis would not have been possible without the help of the DMSE Undergraduate Lab Manager, David Bono, who regularly assisted me with remarkable energy and discernment. He is truly a master of his craft and I was fortunate for the opportunity to learn from him. I am also grateful to Prof. David Perreault whose keen insights on high frequency PCB layouts and power electronics came at a critical juncture.

My interactions with the technical instructors of DMSE, particularly Mike Tarkanian, Tara Fadenrecht, Chris Di Perna, and James Hunter were a consistent source of pleasure to me. I enjoy making things and found kindred spirits in them.

From 2013 to 2016 I received funding from the National Defense Science and Engineering Graduate Fellowship Program. The research projects to which I contributed were supported variously by Sanofi, the Defense Advanced Research Projects Agency, National Science Foundation, and the National Institutes of Health. We are fortunate to live in a time and a place where significant resources are allocated toward furthering understanding of the natural world and developing new technologies. I hope my research activities have served the greater good.

I owe much to the influence of my early scientific mentors, Dr. Richard Stucky and Prof. Jeff Drucker. The moments when I feel I am channeling them are my finer moments as a scientist. I could not have asked for better role models.

Finally, I wish to thank my parents, who have instructed, encouraged, and supported me from my earliest days. Whether it was accompanying me at museum science classes before I was old enough to read or patiently teaching me how to use tools to build and create, I hope you both see a bit of yourselves reflected in this work.

1 Introduction

1.1 Nanomaterials as Minimally Invasive Actuators for Biomedical Applications

The concept of reaching into the body noninvasively to influence biological processes is an appealing idea driving both the development of novel medical technologies and research methods alike. The native biological machinery of neurons, including the channel proteins that cause depolarization to propagate, enables them to amplify the effects of relatively weak stimuli, making them well suited as a preliminary focus for such methods. Noninvasive neuromodulation would offer therapeutic benefits; a variety of diseases may be treated or managed with targeted stimulation in structures deep inside the brain.[1, 2] The current state-of-the-art in medical practice for targeted neural stimulation requires implantation of devices with electrodes that pass through healthy tissue to reach their intended targets.[3] Such an approach is expensive and invasive, and can lead to a variety of complications.[4] Simultaneously, there is growing demand among neuroscientists for techniques that can precisely stimulate the brains of animal models in experiments that further understanding of the nervous system. For instance, the method of optogenetics, in which transgenic expression of light-sensitive channel proteins enables neuromodulation with light, has found widespread use.[5] The investigation of alternative neuromodulation methods analogous to optogenetics is worthwhile if they can facilitate the testing of new hypotheses by neuroscientists or perhaps one day lower the barrier to medical intervention.

The need for noninvasive and minimally invasive stimulation techniques is sufficiently widely recognized that the topic is currently being approached from multiple routes and disciplines. From the perspective of the materials scientist, it is most intuitive to view attempts at noninvasive neuronal stimulation as forms of targeted delivery of energy into the body, and to

categorize them accordingly.[6, 7] These include electromagnetic radiation,[8] mechanical vibration (ultrasound),[9] electric fields,[10] and magnetic fields (static,[11] alternating,[12] and pulsed[13]). Many of these methods avoid the introduction of foreign substances into the body, attempting to produce an effect upon tissue by applying forces or fields in a manner that elicits the intended response.[9, 14] Others consider the possibility of viral transfection to artificially sensitize cells to some external stimulus.[11, 15] Still others develop highly miniaturized and wirelessly powered biocompatible devices. The approach of greatest relevance to the topics discussed in this thesis is the introduction of inorganic nanomaterials suited for biocompatibility, which then play a mechanistic role in stimulation. Such an approach is inherently spatially selective, and often converts a noninvasive stimulus into a form that acts directly upon biological systems. Examples include the translation of magnetic fields to localized electric fields via magnetoelectric composites[16-18] or alternating magnetic fields (AMFs) into localized heating by single domain magnetic nanoparticles (MNPs).[12, 19, 20]

This thesis seeks to contribute to the development of emerging applications that make use of the heat dissipated by MNPs in AMFs to noninvasively trigger either neuromodulation or other therapeutic actions. In particular, it conceptually motivates a method that allows for *selective* heating of different types of MNPs. That such a possibility exists does not appear to have been widely appreciated prior to this work, and the technique could be used to extend the functionality of the wide variety of emerging applications based on heating MNPs.

1.2 Historical Overview of Magnetic Materials in Biomedical Applications

The idea of using magnetic materials for biomedical applications goes back at least a half century.[21] One of the longest studied concepts is cancer hyperthermia, in which the selective heating of magnetic material introduced into a tumor raises its temperature with the goal of

selectively inducing necrosis or apoptosis.[22, 23] Originally this included macroscopic metallic targets that could be heated with eddy currents as well as fine powders of magnetic material.[24] Presently, the focus has shifted almost entirely toward the use of MNPs.[22] This is due at least partly to biocompatibility considerations, since MNPs are of a scale that allows them to be phagocytosed and can be comprised of materials such as iron oxide that the body is well equipped to break down.[25] Cancer hyperthermia has been the subject of thousands of papers, recently including clinical trials with glioblastoma and prostate cancer patients.[26, 27] Some researchers have pointed out fundamental hurdles that may impede practical implementation of hyperthermia, ranging from physical limits on the minimum size for treatable tumors to issues with scaling up AMF sources.[28]

Mechanical manipulation of MNPs with applied magnetic fields is another longstanding trend in research.[23] Starting in the late 1970s, MNPs incorporated into drug carrier systems were investigated with the intention of attracting them to tumors through forces exerted by magnetic field gradients.[29] Preferential accumulation of anticancer drugs at the site of tumors is desirable because it reduces off-target effects resulting from systemic injection. Magnetic beads incorporating MNPs have also been used with magnetic tweezer techniques for precise manipulations of cells and biomolecules.[30] Although such approaches seem appealingly simple, there are significant limitations on manipulating very small MNPs with forces generated by magnetic field gradients. For sufficiently small magnetic objects, the relative influence of viscous forces is high and guiding MNPs becomes infeasible as they decrease in size, especially for applications that require a readily scalable field gradient.[31] Mechanical guidance or actuation methods based on torques rather than forces offer intriguing and comparatively feasible alternatives.[32]

Recent efforts toward targeted noninvasive stimulation using MNPs can be interpreted as an extension of this previous work on heat dissipation and mechanical manipulation, often enabled by new genetic tools. The earliest published occurrence of the speculation that the action of magnetic fields on MNPs could open ion channels can perhaps be found in a paper focused on small quantities of magnetite and maghemite nanoparticles discovered in the human brain.[33] Later, it was suggested that torques and forces on magnetic nanomaterials could be used deliberately for therapeutic stimulation, particularly for tissue engineering.[34] The idea of using heat dissipated by MNPs to trigger a response from the temperature sensitive channel protein and capsaicin receptor TRPV1 (transient receptor potential cation channel subfamily V member 1[35]) for noninvasive stimulation was first published in 2011 by a team led by Pralle.[12] This work provided evidence for nanoscale heating and demonstrated a stimulatory effect *in vitro* in human embryonic kidney cells and hippocampal rat neurons, and *in vivo* in the nematode *C. elegans*.

Subsequent efforts have also claimed stimulation caused by the heating of MNPs in AMFs combined with transgenic expression of heat sensitive channel proteins.[19, 20, 36] A growing trend has been toward a fully "magnetogenetic" approach that makes use of genetically encoded ferritin, sometimes incorporated into to TRPV1 or TRPV4, and such claims have rapidly proliferated in recent years, employing both AMFs and magnetostatic fields for stimulus.[11, 15, 19, 37, 38] A cogent critique of the plausibility of the mechanisms asserted in these studies has pointed out serious conceptual oversights.[39] For these various mechanisms, the energy of interaction between ferritin and applied magnetic fields are typically as much as eight orders of magnitude lower than ambient thermal energy, rendering the proposed mechanisms implausible. In at least one case, methodical independent efforts have failed to reproduce the originally reported

results.[40] In light of this, much of this intriguing work should be viewed with healthy skepticism. Even if the effects prove to be real, their origin seems to be poorly understood.

1.3 Physiological Limits for Applying Alternating Magnetic Fields

Suitability of AMFs for noninvasive actuation assumes that AMFs cause acceptably low levels of off-target effects. In principle, various forms of magnetic interaction with the body are possible. Although the overall character of human tissue is known to be weakly diamagnetic, due largely to its high water content, its constituent materials vary in their magnetic properties. For instance, the hemoglobin in blood is paramagnetic,[41] the cores of ferritin are antiferromagnetic ferrihydrite or ferric oxyhydroxide,[42] and there is even evidence suggesting the presence of small quantities of endogenous ferrimagnetic magnetite and maghemite nanocrystals in the human brain.[33, 43] These ferrite nanocrystals occur in an exceedingly small mass fraction on the order of parts per billion,[33] so the dominant concerns of applying AMFs to healthy tissue do not arise from magnetic properties, but rather weak, ionically-based electrical conductivity.

Time changing magnetic flux in a conductive object can cause eddy currents to arise due to Faradic induction. In tissue, these currents are too weak to produce magnetic fields that significantly counteract the applied AMFs in deep tissue, but the associated heat dissipation cannot be ignored. Off-target heating averaged over time depends on numerous factors including duty cycle, geometry of the exposed region, and field profile. However, for problems of various dimensionalities, dissipated power can be expressed as a function of $H_0 f$, where H_0 is the AMF amplitude and f is its frequency. For this reason, a commonly adopted constraint in cancer hyperthermia research is a fixed maximum permissible field amplitude-frequency product, $H_0 f$. A frequently cited value for this constraint, $H_0 f \leq 5 \times 10^9\ \mathrm{Am^{-1}s^{-1}}$,[44] typically restricts

maximum useful operating frequencies to the low MHz range for heating MNPs in biomedical applications.

Several useful criticisms can be made of the simple $H_0 f$ product limit. One is that the conductivity of tissue varies with bodily location and frequency. Specifically, conductivity tends to increase with frequency, particularly in the MHz range.[45] At low frequencies, the possibility for indiscriminate neural stimulation exists, limiting amplitudes to lower values than the $H_0 f$ product limit might suggest.[22]

1.4 The Basic Concept of Magnetothermal Multiplexing

The previous sections in this chapter have together offered a context for viewing the heating of MNPs in an AMF as a possible form of minimally invasive, targeted delivery of energy, suitable for actuating a variety of emerging biomedical technologies. In this sense, the AMF can be viewed as delivering a simple signal ("on" or "off") with spatial and temporal specificity. This thesis is focused on developing the concept of magnetothermal multiplexing,* which could extend this functionality by offering a means for selectively heating different types of MNPs by applying distinct AMF conditions. In the case of applications based on bulk heating, this allows for different regions of a target to be heated selectively, while in the case of applications based on nanoscale heating, it permits selective actuation of MNP populations even when they are collocated. Subsequent chapters that discuss applications developed during this thesis work will emphasize how these methods might be meaningfully extended by robust magnetothermal multiplexing.

* "Multiplexing" in typical usage refers to the ability of a communication line to carry multiple signals simultaneously. The term is somewhat differently applied to this technique for selective heating, since a superposition of the selective AMFs would not necessarily heat both particle types.

To illustrate the utility of such a technique, consider the abstract representation shown in Figure 1.1. For the moment, the details and mechanisms of MNP heating and its action on the cell may be neglected. It is easy to imagine, given the number of cell types and variety of structures in the human body, that it could be advantageous to selectively stimulate different cells that are in close proximity. Particularly in the brain, where targeted structures are situated deep below the surface, offering multiple stimulatory handles is an appealing possibility.

Such a vision of selective neural stimulation with MNPs provided the impetus for the work on this topic discussed in this thesis, though it may prove useful for other applications that would benefit from noncontact selective heating. For instance, a different technique using selectively heated macroscopic induction targets has been shown to adjust the resonant frequency of dynamic vibration absorbers,[46] and something similar might be accomplished with multiplexed ferrofluids. This simply serves to underscore the fact that magnetothermal multiplexing is a materials concept with sufficient generality that developing and studying it in the kinds of systems discussed here could also make it available for other types of applications.

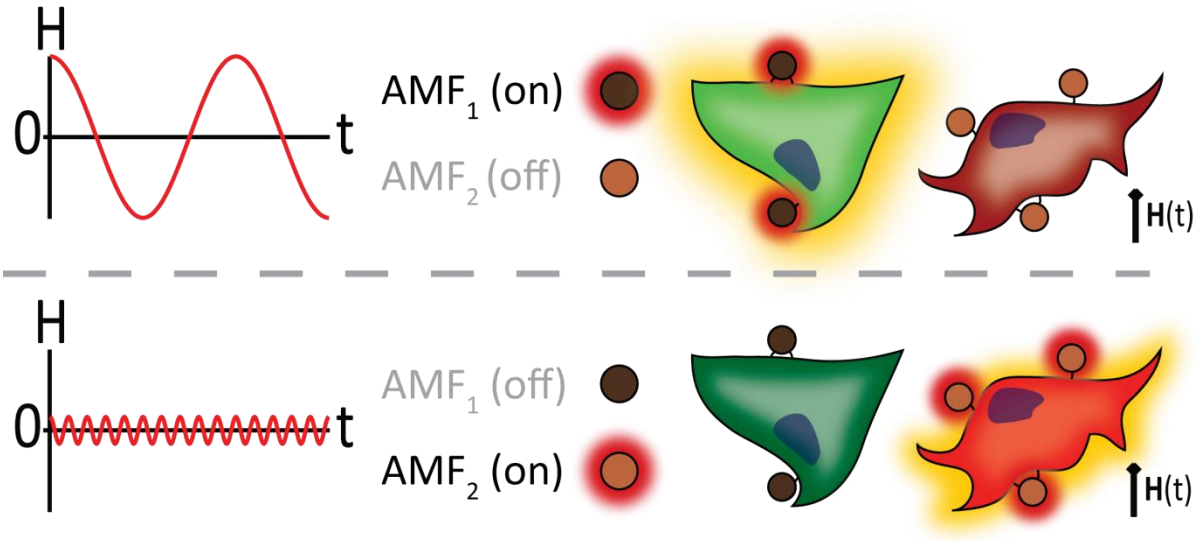

Figure 1.1 The basic concept of magnetothermal multiplexing is depicted abstractly. By changing the frequency and amplitude of an AMF, different types of MNPs are selectively heated, providing a means to elicit independent responses from two different types of cells.

1.5 Figures of Merit and Scoring Functions

It is often useful to establish "figures of merit" to assess the effectiveness of an engineered design in meeting some technological aim. Not only can this facilitate an objective, quantitative comparison of different approaches, but, perhaps more importantly, it clearly articulates desired performance in a way that can guide design. In order to gain a clearer understanding of the attributes of an effective magnetothermal multiplexing system, it is useful to consider how such a quantity might be defined.

A logical starting point is the prevailing figure of merit used in literature to describe the efficiency of MNP heat dissipation in the presence of an AMF, specific loss power (SLP), an

intensive quantity stated in watts of dissipated power per gram of metal ion content.[†] (For a description of the methods used in the work conducted for this thesis to measure SLP, please see Sections 4.4 and 4.5). SLP is most useful for applications that rely on bulk heating, such as cancer hyperthermia,[44] ferrofluid stimulation,[20] or actuation of shape memory polymer composites.[47] In these cases, a higher SLP either allows for more rapid heating, higher steady state temperature, or a reduction of the concentration needed to produce similar effects, all of which are potentially desirable outcomes.

One criticism that can be made of SLP centers on the fact that it does not account for AMF conditions, a shortcoming that is especially problematic when comparing SLPs reported in literature, which rarely use the same AMF conditions. Indeed, some of the highest reported SLPs make use of AMF conditions with $H_0 f$ products significantly larger than similar literature.[48] From a physical perspective, AMFs store energy, some fraction of which is dissipated as heat by MNPs. One example of a more generalized comparison that has been suggested is to divide SLP by ${H_0}^2 f$, yielding a quantity dubbed "intrinsic loss power."[49] The rationale offered for this choice is based on the functional dependence suggested by linear response theory (discussed in Section 2.3) at low field amplitudes. The resulting units of $\mathrm{nH\,m^2\,kg^{-1}}$, do not offer a particularly intuitive representation of loss power.[49] A similar, but more straightforward approach that does not appeal to results of any particular model might be to consider a unitless ratio of two energy densities:[50] 1) the population and time-averaged dissipated energy density in the MNPs per cycle of the AMF and 2) the time-averaged energy density of the magnetoquasistatic field $\langle u_B \rangle$ in the absence of MNPs.

[†] The term specific absorption rate (SAR) is sometimes used for the same quantity, however in some contexts, the concept of SAR is also applied more generally to heat dissipation in tissue e.g. from absorption of radiofrequency radiation. To avoid confusion, specific loss power (SLP) is used throughout this thesis.

$$\frac{SLP\ \rho_m}{f}\left(\frac{1}{\langle u_B \rangle}\right) = \frac{4\ SLP\ \mu_0\ \rho_m}{{H_0}^2 f} \qquad 1.1$$

Here, ρ_m is the mass density of the material comprising the MNPs and μ_0 is the permeability of free space. This results in the same functional dependence on H_0 and f as intrinsic loss power, but unsurprisingly the comparison yields a tiny unitless fraction, even for very high reported heating rates. Neither intrinsic loss power, nor any similarly generalized quantity has been widely adopted. Clinical viability depends less on strict efficiency of energy transfer than it does on minimizing dosing and ensuring a safe level of off-target effects. The interaction of the body with the AMF, which results in off-target heat dissipation at high frequencies and possibly neural stimulation at low frequencies, is a nuanced issue depending on both intrinsic and extrinsic factors, and it is therefore inadvisable to attempt to incorporate it directly into a general figure of merit.

In applications that rely on nanoscale heating, such drug release from liposomes, an estimate of individual particle loss power (IPLP) may be more relevant than SLP.[51] This is an extensive property rather than an intensive one that can be estimated for monodisperse MNPs by multiplying the SLP by the approximate volume of an individual MNP, typically resulting in quantities on the order of fW. As will be discussed in Chapter 2, IPLP has a convenient theoretical interpretation as well: it is the area of a hysteresis loop for a population-averaged MNP, multiplied by the frequency of the AMF.

Since magnetothermal multiplexing is, in principle, applicable to situations whether bulk or nanoscale heating is most relevant, comparisons of magnetothermal multiplexing performance must be compatible with either SLP or IPLP, depending on the particular application. The sketch provided in Figure 1.2 conceptually illustrates effective magnetothermal multiplexing at two AMF conditions, contrasting it with a representation of ineffective magnetothermal multiplexing.

Let $LP_{x,1}$ be the loss power of MNP type X at AMF condition 1, and so forth. The key desirable features can be broken down into quantitatively describable aims: efficiency, selectivity, and parity. Systematic comparison between multiplexing sets in enabled by defining scoring functions that vary between 0 and 1 to assess the extent to which these aims are met, where 1 corresponds to the ideal case.

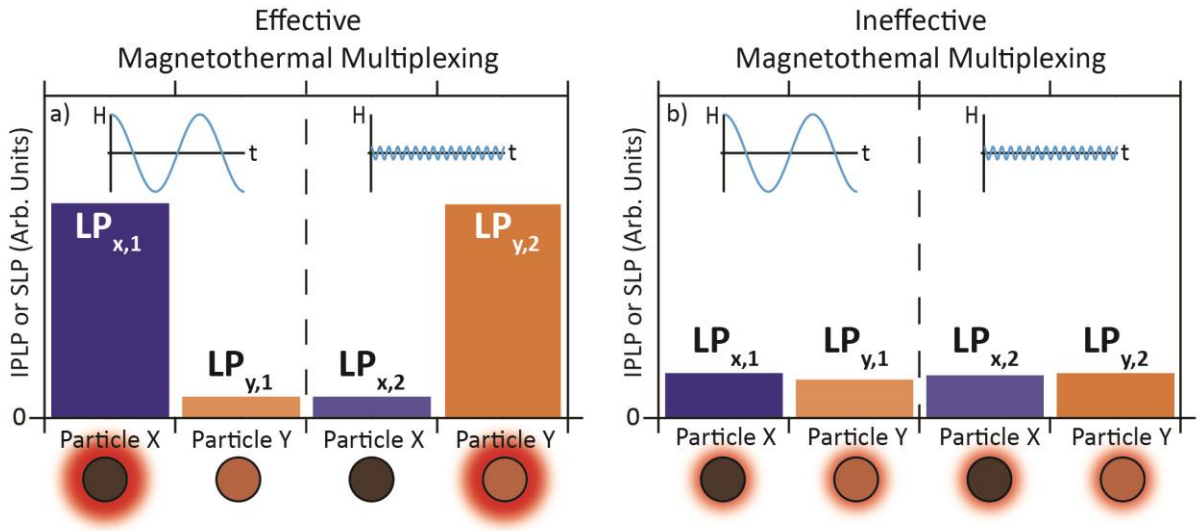

Figure 1.2 A sketch contrasting (a) idealized magnetothermal multiplexing performance with (b) highly unsatisfactory magnetothermal multiplexing performance. This graphic is intended to facilitate understanding of the definitions of the proposed scoring functions for magnetothermal multiplexing.

1. **Efficiency**

   Efficient heat dissipation by MNPs is generally desirable for magnetothermal applications, and this requirement should not be relaxed for effective multiplexing. Usually heating efficiency of a single set would be stated simply in terms of a loss power like SLP or IPLP. However, limiting the scope of the comparison to a set of empirically tested options, efficiency can be reframed in terms of the extent to which the materials are being utilized relative to maximum available loss powers allowed by constraints on acceptable AMF

conditions.[44] (See Figure 1.3(a).) Ideally, both materials would exhibit comparable heating near this maximum value at their preferred AMF conditions. Defining a efficiency function for multiplexing with two types of MNPs that varies from 0 to 1, and does not depend on knowing which type of MNPs is meant to be favored at each condition,

$$\text{efficiency} = \frac{LP_{x,1} + LP_{y,2}}{2LP_{max}} \tag{1.2}$$

2. **Selectivity**

In an effective multiplexing system, one AMF condition should selectively heat one type of MNPs as compared to its heat dissipation at the other AMF conditions. To quantify adherence to this principle, a simple function is desirable, ranging from 0 to 1, that is maximized when, e.g., $LP_{x,1} \gg LP_{x,2}$. It is also desirable for the function to be symmetric with respect to exchanging its two arguments. An example of such a function is as follows:[‡]

$$\text{selectivity} = 1 - \frac{LP_{x,1}LP_{x,2}}{\left(\frac{LP_{x,1} + LP_{x,2}}{2}\right)^2} \tag{1.3}$$

This should be evaluated for both types of MNPs at a given set of AMF conditions, retaining the minimum of the two in order to most accurately reflect limitations in performance. Figure 1.3(b) illustrates the dependence of this function on $LP_{x,1}$ and $LP_{x,2}$. Selectivity might have instead been defined in terms of $LP_{x,1}$ and $LP_{y,1}$, but the possibility of adjusting concentration in bulk heating situations effectively allows these loss powers to be scaled by a constant. The form of Equation 1.3 is invariant under this transformation, but it is necessary

[‡]The inspiration for this simple function is geometric. The second term represents a ratio between the area of a rectangle with side lengths $LP_{x,1}$ and $LP_{y,1}$ and a square constructed from the same perimeter. Thus this term approaches a maximum of 1 when $LP_{x,1} = LP_{y,1}$ and tends to 0 in the limit of great dissimilarity.

to add the further requirement that MNP types x and y exhibit different preferred AMF conditions. This can be expressed mathematically as follows

$$\frac{LP_{x,1} - LP_{x,2}}{LP_{y,2} - LP_{y,1}} > 0 \qquad 1.4$$

Setting the selectivity to 0 in cases when this condition is not met ensures that the sets being compared are indeed selectively heated at different AMF conditions.

3. **Parity (Nanoscale Heating Applications Only)**

An additional characteristic desired in magnetothermal multiplexing is comparable heating rates by the different types of MNPs at their favored conditions. In bulk heating applications, this can be brought about by choosing appropriate concentrations, but in nanoscale heating, it relies on intrinsic properties. Without this characteristic, systems exhibiting high selectivity as defined in Equation 1.3 could actuate responses at substantially different rates or with different efficacy. A simple function similar to the one defined for selectivity can be used to ensure that IPLPs are comparable:

$$\text{partiy} = \left[\frac{IPLP_{x,1} IPLP_{y,2}}{\left(\frac{IPLP_{x,1} + IPLP_{y,2}}{2}\right)^2}\right]^8 \qquad 1.5$$

Figure 1.3(c) illustrates the dependence of this function on $IPLP_{x,1}$ and $IPLP_{y,2}$. The basic expression in Equation 1.5 has been raised to a power of 8 in order to manipulate the shape of the function. It should be noted that because each of the functions in Equations 1.2, 1.3,

and 1.5 have been defined so that they range between 0 and 1, adjusting the power to which they are raised is a way of adjusting their shape.

In the interest of clarity, the above discussion has been restricted to multiplexing with two types of MNPs. Appendix A addresses how these principles may be straightforwardly extended to situations in which three or more multiplexing materials are desired. In practice, it may be useful to construct a weighted average of these three figures of merit to describe overall performance. The needs of particular applications should influence the weights. See Sections 5.4 and 6.5 for examples of these principles applied to select materials for multiplexing.

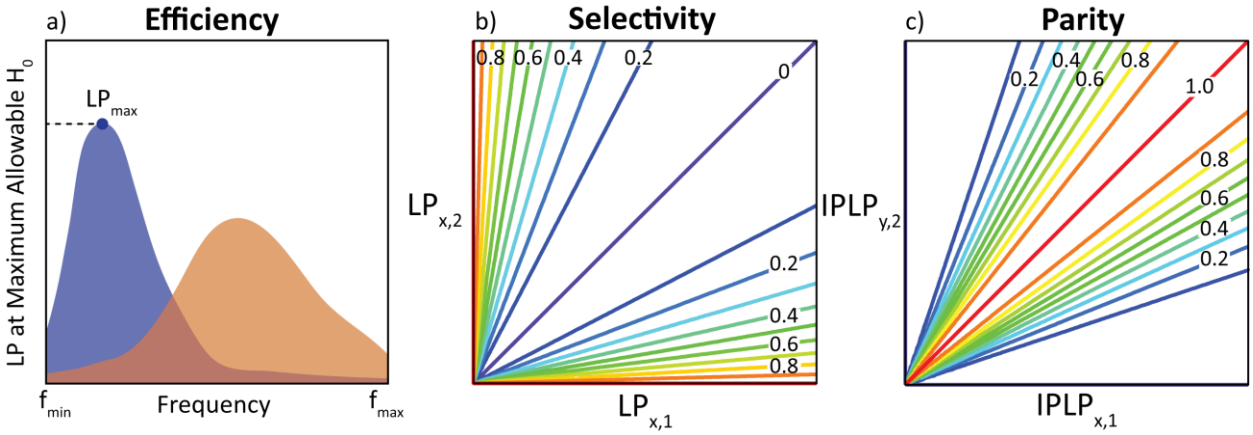

Figure 1.3 (a) The scoring function for efficiency takes an average of loss powers at favored conditions and normalizes it to the maximum achievable loss power for the types of MNPs under consideration, subject to the AMF constraints, as suggested in Equation 1.2. (b) A contour plot shows the scoring function for selectivity expressed in Equation 1.3. Selectivity is maximized when the loss powers of an MNP type differ significantly at two AMF conditions. (c) Parity is the tendency for the favored modes to exhibit comparable individual particle loss powers at their favored conditions, and is relevant to applications based on nanoscale heating. A contour plot of Equation 1.5 is shown.

1.6 Structure of the Thesis

The content and structure of this document have been created with the intent that it might serve as a useful starting point for anyone wishing to continue this research. To that end, an

effort has been made to keep the main text reasonably concise and direct, and appendices have been used extensively. By adopting this structure, it is hoped that the main text will remain readable, while greater depth and more detailed explanations of relevant topics are still made available to the curious reader.

The present chapter has provided broader context for the work presented in this thesis and a conceptual introduction for magnetothermal multiplexing. Chapter 2 reviews and discusses approaches for modeling heat dissipation by MNPs in the presence of an AMF, focusing on their differing predictions for the feasibility of magnetothermal multiplexing. Chapter 3 explains design principles and techniques for setups that generate AMFs. Such apparatuses are essential for experimental evaluation of magnetothermal multiplexing and for the experiments conducted in the body of work described in this thesis. The underappreciated difficulty of enlarging such setups to clinically relevant scales is emphasized. Chapter 4 describes characterization techniques, with an emphasis on a heuristic, empirically-based approach for identifying materials suitable for magnetothermal multiplexing.

Chapters 5 and 6 summarize collaborative studies that explored possible biomedical applications of MNPs heated by AMFs. These have been divided according to the relevant length scale of heating involved in their mechanism of action, with Chapter 5 addressing those based on bulk heating effects and Chapter 6 addressing those based on nanoscale heating effects. Rather than recapitulating details adequately described in published work on these topics, their main points are succinctly stated and results are discussed. Both of these chapters consider how multiplexing might be used to extend such techniques. Chapter 7 concludes by offering a perspective on the lessons that should be drawn from the body of work presented in this thesis.

2 Chapter 2. Modeling Magnetic Nanoparticle Heating

2.1 Hysteresis as Thermodynamic Framework for Modeling Nanoparticle Heating

This chapter examines several models that describe the heating of MNPs in AMFs, with various initial assumptions and differing levels of complexity. Superficially, these methods can seem so distinct from each other that it is elucidating to emphasize the thermodynamic context connecting them. Essentially, these are all models for predicting hysteresis and from it deducing dissipated energy. This approach is clearly not unique to magnetic systems; viscoelastic response and dielectric loss are direct analogues.

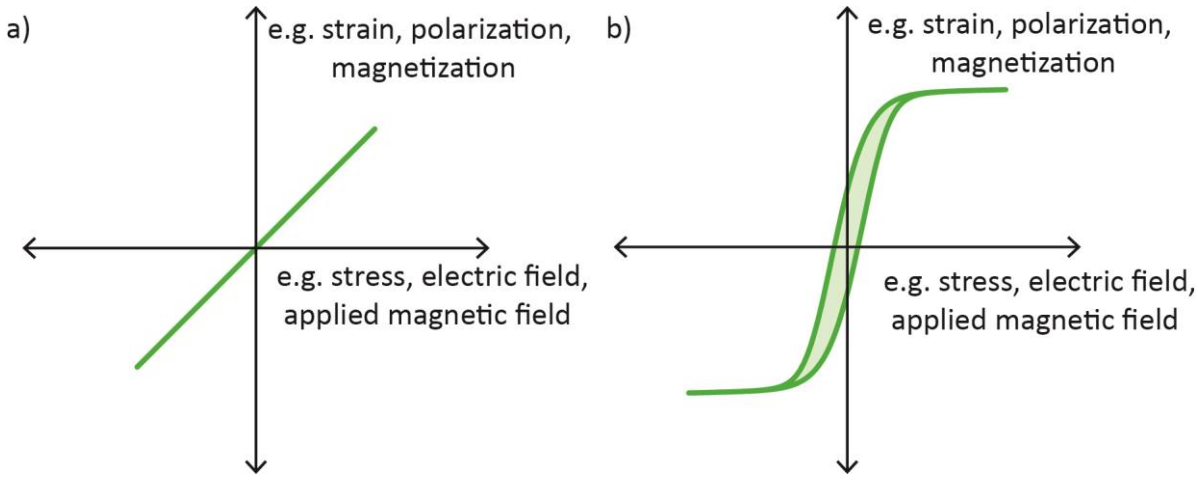

Figure 2.1 (a) Representation of a (linear) state function in which energy is stored reversibly. (b) History dependent state function, leading to energy dissipation represented by the area of the loop.

In cases of simple state functions of conjugate variables such as stress and strain, electric field and polarization, or magnetic field and magnetization, a cyclically applied force describes a path that simply retraces itself (Figure 2.1(a)). Energy is reversibly stored in the cycle, represented by the area under the curve. Such behavior idealizes real systems, which inevitably dissipate some energy, even if they may store energy very efficiently. The result is that the material state depends not only on the instantaneous value of an applied force, but also on the

history of the system. For cyclic driving forces in steady state, the path forms a closed loop with an area proportional to the energy dissipated per cycle of the field (Figure 2.1(b)). A more rigorous thermodynamic justification of this interpretation can be found in Appendix C.

Conceptualizing dissipation with hysteresis is useful because it allows the problem to be framed in terms of the kinetic processes that influence the dynamical response of magnetization under the influence of an AMF. This provides a route for making predictions relevant to the design of such materials that does not require working out the detailed microscopic mechanism by which heat is dissipated. The situation is analogous to making use of phenomenological models of friction without having to delve into the details of interfacial science that lead to its effects. Another useful consequence is the availability of graphical interpretations of hysteresis loops resulting from different models that facilitate intuitive comparison.

2.2 Magnetic Nanoparticles: Basic Physical Picture

The dynamical behavior of fine or nanoscale magnetic nanoparticles (MNPs) is a topic of long standing scientific and technical interest, ranging from interpreting evidence of paleomagnetism[52] to designing patterned media for memory storage in hard drives.[53] Decades of theoretical and empirical studies have developed a picture of the behavior of these MNPs at the nanoscale that differs in intriguing ways from bulk materials, a picture that is a necessary starting point for understanding models of MNP heating.

Exchange or superexchange interactions drive magnetic ordering, and these quantum effects operate in much the same way regardless of whether a crystal is composed of 10^5 atoms or occurs in bulk. However, many bulk materials exhibit magnetic order microscopically, yet have no net magnetic moment in the absence of an applied magnetic field. This is because they are able to form local domains that reduce magnetostatic energy. [54] In MNPs below an

approximate size that depends on their magnetic properties, the exchange energy penalty arising from the formation of a domain wall would far exceed the reduction in stray field energy. This has the important consequence that such MNPs exhibit a single domain and can often be regarded as uniformly magnetized, though even at small sizes, surface effects can lead to spin canting[55] and larger sizes they can begin to exhibit intermediate "pseudo-single domain" behavior.[56] For iron oxide MNPs, the onset of the latter has been estimated to be 80nm, significantly larger than the MNPs studied in this work.[57]

Even when a MNP can often be considered uniformly magnetized, the orientation of its moment fluctuates, often quite rapidly, as has been shown directly in microscopic magnetometry experiments that observe stochastic reversal.[58] Despite fluctuating, the moment of an MNP will tend, on average, to be directed along certain preferred directions. These are called "easy axes" and they are separated by energy barriers. Magnetic anisotropy, the energy landscape that leads to this preference, can originate from spin-orbital interactions at the atomic level,[59] the shape of the MNP,[60] surface effects,[61] or potentially strain fields in magnetostrictive materials (Appendix B). Stochastic fluctuation of the moment relative to the physical structure of the MNP is termed Neél relaxation after the French geophysicist who first proposed it.[62] The characteristic timescale of stochastic coherent reversal over the anisotropy energy barrier τ_N can be approximated by assuming a constant attempt rate υ_0 and assuming that the moments overcome the barrier proportionally to a Boltzmann distribution of the energies of the moments.

$$\tau_N = \frac{1}{\upsilon_0} \exp \frac{K_{eff} V_m}{k_B T} \qquad 2.1$$

K_{eff} is the effective anisotropy energy, V_m is the magnetized volume, k_B is the Boltzmann constant, and T is the absolute temperature. Other expressions have been suggested for τ_N that incorporate dependence of the attempt rate on the applied field.[63] However, the exponential term

dominates all of these expressions, the typical attempt rate assumed is really an order of magnitude estimate, and K_{eff} is typically difficult to predict for real MNPs (Appendix B). These considerations limit the practical benefit of adopting a more complex form for the attempt rate.

MNPs suspended in a fluid are also expected to physically rotate ("Brownian relaxation"), providing an additional source of fluctuation of the direction of the magnetic moment even in cases where the anisotropy barrier is large compared to the ambient thermal energy.[64] In the absence of an applied magnetic field, this occurs at a timescale τ_B estimated by the hydrodynamic volume V_H as well as the viscosity η of the medium.[63]

$$\tau_B = \frac{3\eta V_H}{k_B T} \tag{2.2}$$

One of these stochastic processes typically occurs much faster than the other and is thus expected to dominate behavior. Since they occur in parallel, the overall characteristic timescale τ can be expressed as follows:

$$\tau = \frac{1}{1/\tau_N + 1/\tau_B} \tag{2.3}$$

Interparticle interactions can play a significant role in the behavior of MNPs in some cases. For MNPs with a high saturation magnetization and high local concentration, the interaction effects can be so pronounced that they lead to forms of magnetic ordering observable by electron holography.[65] Even in dilute dispersions of materials with a lower saturation magnetization, structures such as rings or chains can be formed to reduce energy.[66] Most attempts to model the heating of MNPs neglect this interaction—a choice that is well motivated only for dilute and well dispersed suspensions. This applies to many of the specific applications explored in this

thesis, as evidenced by low overall concentrations and dynamic light scattering data that does not indicate the presence of aggregates.

2.3 Linear Response Theory

A magnetic material is said to be linear and isotropic when magnetization $\vec{M}$ and applied magnetic field $\vec{H}$ can be related by a constant, the magnetic susceptibility χ.

$$\vec{M} = \chi\vec{H} \tag{2.4}$$

This framework can be extended to include sinusoidally varying applied magnetic fields when the response of the magnetization is also sinusoidal, with an amplitude that scales linearly with applied field amplitude and a phase that possibly lags behind. Mathematically, this can be described simply by allowing the susceptibility to assume complex values.

$$M = \tilde{\chi}H_0 e^{i\omega t} = |\tilde{\chi}|H_0 e^{i(\omega t+\phi)} \tag{2.5}$$

Where $\omega = 2\pi f$, t is time, $|\tilde{\chi}| = \sqrt{\tilde{\chi}^*\tilde{\chi}}$, and $\phi = \arctan\left[\frac{\mathrm{Im}(\tilde{\chi})}{Re(\tilde{\chi})}\right]$. Complex susceptibility can be viewed equivalently as a way of describing elliptical hysteresis loops. The in phase (real) component of the magnetization stores energy, whereas the out of phase (imaginary) component dissipates energy. Appendix D offers a more detailed explanation of this point. A model that seeks to determine $\tilde{\chi}$ as a function of frequency and material properties should, in principle, offer insight into the physical behavior of the system and influence design or selection MNPs that heat well in the presence of an AMF.

Multiple models of this kind have been proposed, and perhaps it is most appropriate to collectively refer to them as "linear response theories," but the term is now used most frequently

in reference to a particular approach articulated by Rosensweig in 2002.[63] This work drew upon existing models for susceptibility, but the way in which it presents a simple analytical expression for dissipated heat has led to its eager and ubiquitous adoption by the field of cancer hyperthermia.[22] Conceptually, this work is derived from the efforts of Debye and others in the early twentieth century to explain frequency dependent dielectric properties of molecular substances with electric dipole moments.[67] Although physics determining timescales of the relaxation processes differs, the underlying rationale and the functional dependence of $\tilde{\chi}$ on frequency are identical. In linear response theory with MNPs, the key dynamical equation can be stated as follows

$$\frac{\partial M}{\partial t} = \frac{1}{\tau}\left(M_{eq} - M\right) \tag{2.6}$$

Noting that when $M = M_{eq}$, $\frac{\partial M}{\partial t} = 0$, and that when $M > M_{eq}$, $\frac{\partial M}{\partial t} < 0$, this equation can be readily understood to describe reversion to equilibrium magnetization M_{eq} at a rate set by τ that is characteristic of stochastic reversal. By assuming a sinusoidal driving field, and substituting a solution of the form in Equation 2.5, an expression for the complex susceptibility that solves Equation 2.6 can be found algebraically.

$$\frac{\partial(\tilde{\chi}H_0 e^{i\omega t})}{\partial t} = \frac{1}{\tau}\left(\chi_{eq}H_0 e^{i\omega t} - \tilde{\chi}H_0 e^{i\omega t}\right) \tag{2.7}$$

$$i\omega\tilde{\chi} = \frac{1}{\tau}\left(\chi_{eq} - \tilde{\chi}\right) \tag{2.8}$$

Solving for $\tilde{\chi}$,

$$\tilde{\chi} = \frac{\chi_{eq}}{1 + i\omega\tau} \tag{2.9}$$

To straightforwardly interpret this result, $\tilde{\chi}$ can be written in terms of its real and imaginary components.

$$\mathrm{Re}(\tilde{\chi}) = \chi_{eq}\left[\frac{1}{1+(\omega\tau)^2}\right] \qquad 2.10$$

$$\mathrm{Im}(\tilde{\chi}) = \chi_{eq}\left[\frac{\omega\tau}{1+(\omega\tau)^2}\right] \qquad 2.11$$

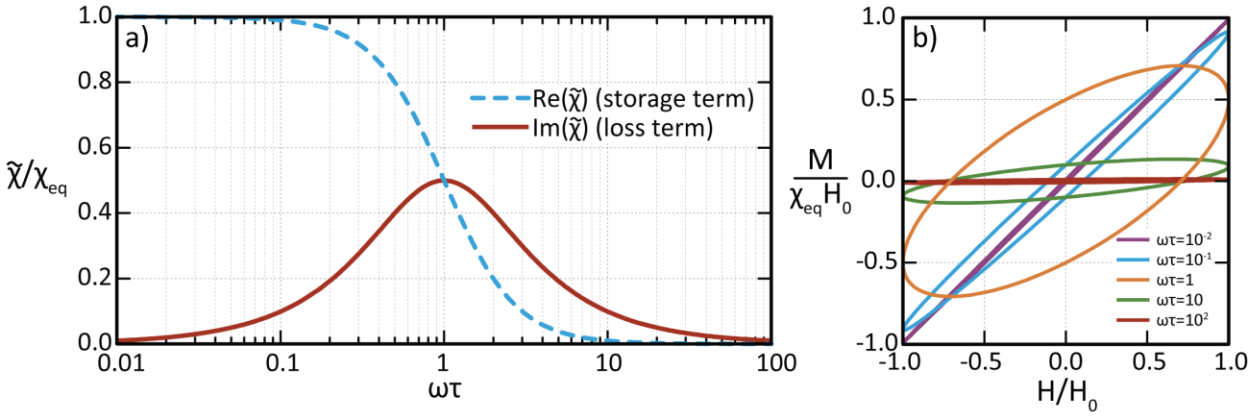

Figure 2.2 (a) Real and imaginary parts of susceptibility are shown in a physically generalized way for linear response theory by normalizing them to static (i.e. equilibrium) susceptibility $\boldsymbol{\chi_{eq}}$ and adopting the unitless frequency coordinate $\boldsymbol{\omega\tau}$ that normalizes the frequency to the rate of stochastic reversal. Note that is plot identically describes both Debye theory and the most frequently cited version of linear response theory for MNP suspensions, the only difference being whether $\boldsymbol{\chi}$ is taken to describe electric or magnetic susceptibility, respectively. (b) The family of elliptical hysteresis loops represented in (a) is shown.

Noting that the imaginary part of $\tilde{\chi}$ (loss term) is maximized at the crossover point between $\mathrm{Re}(\tilde{\chi})$ and $\mathrm{Im}(\tilde{\chi})$, and setting Equations 2.10 and 2.11 equal to each other, it can be found that this condition is met when

$$\omega\tau = 1 \qquad 2.12$$

This is a statement that captures the essential physical message of linear response theory. It predicts that, regardless of applied field amplitude, maximal heating will occur at a frequency corresponding to the timescale of stochastic reversal. In the "superparamagnetic regime," where

$\omega\tau \ll 1$, the magnetization is able to keep pace with equilibrium and dissipation is negligible. In the "ferromagnetic regime,"[§] where $\omega\tau \gg 1$, magnetization is unable to appreciably respond to the field and dissipation is negligible. When this is combined with the fact that τ varies strongly with MNP diameter, especially when Neél relaxation dominates, the result is a sharp maximum at a particular MNP diameter. This has frequently been interpreted as an impetus to "tune" MNP size or effective anisotropy to maximize heating effects.

Unfortunately, while the logic of linear response theory is valid and instructive, its basic premises are arguably flawed in most of the cases to which it is applied. To see this clearly, it is useful to contrast the physical situation to Debye relaxation, an almost identical model with justifiable premises. In the case of dielectric response of polar molecules, the energy barriers to reversal can be an order of magnitude larger than $k_B T$, whereas the energy of the dipole moment of a single molecule in an electric field of reasonable magnitude is far smaller than $k_B T$.[67] In such a case, it is reasonable to approximate the rate of stochastic reversal as being unaltered by the applied electric field. On the other hand, MNPs are comprised of ~10^5 atoms with magnetic ordering, with the result that the energy of its magnetic moment in an applied field can exceed $k_B T$ at readily accessible conditions. (Indeed, this is the basis of the term "superparamagnetism.") Because the energy scale of the moment in the field can be comparable to the energy scale of the anisotropy barriers, τ ought to depend strongly on H, but this is conspicuously neglected in linear response theory. None other than Neél himself considered the effects of small fields on altering the forward and backward rates of reversal in the work cited as the origin of Neél relaxation,[62] and this was for the geomagnetic field, which is thousands of

[§] This term is somewhat unfortunate because it likewise applies to ferrimagnetic materials and could give the false impression that the exchange forces producing magnetic ordering are not also at work in the superparamagnetic regime. Some researchers have described this regime alternatively as one in which "quasistable hysteresis" occurs.

times smaller than applied field amplitudes typical for hysteretic heating.[**] Although behavior can be expected to converge to linear response theory in the limit of anisotropy energy scales much larger than energy scales of interaction with the applied field, it is not sufficient to merely attempt to adjust the expression for τ and substitute into the old formulas. If τ depends on H, and indeed it can range several orders of magnitude during a cycle of the AMF, sinusoidal functions will no longer solve Equation 2.6. Clearly, alternative models are required.

2.4 Dynamic Hysteresis

The model referred to as "dynamic hysteresis" in this thesis reflects an attempt to retain as many of the simple premises on which linear response theory is based, while accounting for the influence of the applied field amplitude on rates of coherent reversal.[68] For the azimuthally symmetric case of easy-aligned MNPs with uniaxial anisotropy under the influence of an applied magnetic field, the combined energy landscape is shown in Figure 2.3. In order to compare the relative magnitude of these two contributions to each other and to the influence of thermal fluctuations, it is natural to define the unitless parameters σ for anisotropy and ξ for Zeeman energy.

$$\sigma \equiv \frac{K_{eff} V_m}{k_B T} \tag{2.13}$$

$$\xi \equiv \frac{\mu_0 H M_s V_m}{k_B T} \tag{2.14}$$

This allows for the combined energy to be expressed in the following form:

$$\frac{E(\theta, t)}{k_B T} = \sigma \sin^2 \theta - \xi \sin(\omega t) \cos \theta \tag{2.15}$$

[**] This paper is written in French. I am indebted to my colleague Eléonore Tham for her help in translating a few key parts and our subsequent discussion.

Notably, when $|\xi| = 2\sigma$, the effective barrier to reversal vanishes, as explained in Appendix E. This suggests a natural normalization of applied field to the critical value at which the barrier vanishes, the "anisotropy field" H_k. Note that this is *not* the same as "coercive field" H_c, which is simply the field at which $M = 0$ in a hysteresis loop.

$$H_k \equiv \frac{2K_{eff}}{\mu_0 M_s} \rightarrow \frac{\xi}{2\sigma} = \frac{H}{H_k} \tag{2.16}$$

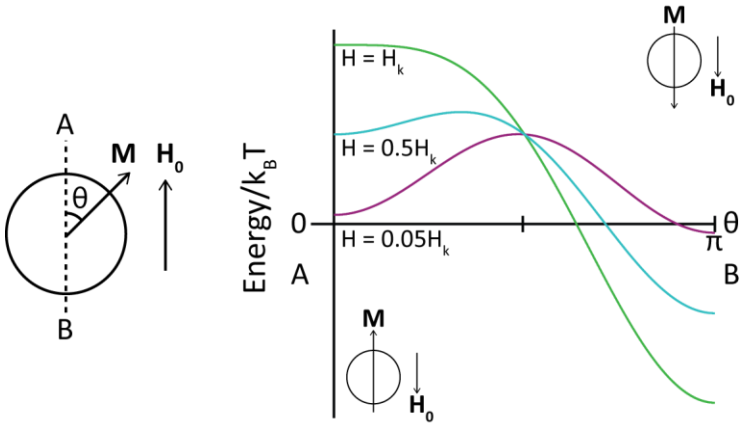

Figure 2.3 The energy landscape resulting from the summation of easy aligned uniaxial anisotropy and the Zeeman energy of the MNP moment in the applied magnetic field is shown, for three field magnitudes. These are normalized with respect to the anisotropy field $\boldsymbol{H_k}$, at which the barrier to reversal vanishes. A sketch is included for clarity. Note that azimuthal symmetry permits this representation, because the energy depends only on the polar angle $\boldsymbol{\theta}$.

A consequence of focusing on the easy aligned uniaxial case is that the energy minima do not change orientation under the application of a magnetic field. Let P_A represent the proportion of moments confined to the minimum at $\theta = 0$, and P_B represent the proportion of moments confined to the minimum at $\theta = \pi$. Though the formulation of escape rates depends on a statistical distribution of orientations, for the purpose of approximating the net magnetization of an ensemble of such MNPs, these moments can be considered restricted to the minima.

$$M \approx P_A \cos 0 + P_B \cos \pi = P_A - P_B \tag{2.17}$$

A modification of this treatment to partially account for thermal spreading can be found in Appendix E. Equation 2.6 implicitly assumes symmetry in the instantaneous forward and backward rates of moments over the anisotropy barrier, an assumption in accordance with the idea that the barrier remains essentially unperturbed. Taking the energy of interaction with the field into account, this symmetry is lost, and a system of equations is required to describe forward and backward rates.

$$\frac{d}{dt}\begin{bmatrix} P_A \\ P_B \end{bmatrix} = \begin{bmatrix} -\nu_A & \nu_B \\ \nu_A & -\nu_B \end{bmatrix}\begin{bmatrix} P_A \\ P_B \end{bmatrix} \qquad 2.18$$

Consistent with the reasoning that motivated Equation 2.6, the instantaneous rates of escape over the barrier can be expressed in terms of an assumed attempt rate weighted by the proportion of moments expected by a Boltzmann distribution to surmount the energy barrier. ν_A, the instantaneous escape rate from $\theta = 0$, can be expressed in terms of the energy barrier U_A.

$$\nu_A = \nu_0 e^{\frac{-U_A}{k_B T}} \qquad 2.19$$

Analytical expressions for $\frac{U_A}{k_B T}$ and $\frac{U_B}{k_B T}$ as functions of σ and ξ can found by analyzing Equation 2.15, as described in Appendix E. Recognizing that ξ varies sinusoidally in time, Equation 2.19 can be substituted back into Equation 2.18. The resulting system of differential equations is numerically solvable, and the solutions, $P_A(t)$ and $P_B(t)$ can be substituted into Equation 2.17 to find $M(t)$. As demonstrated by Figure 2.4, the forms of $M(t)$ and $\frac{\partial M}{\partial t}$ are clearly not sinusoidal.

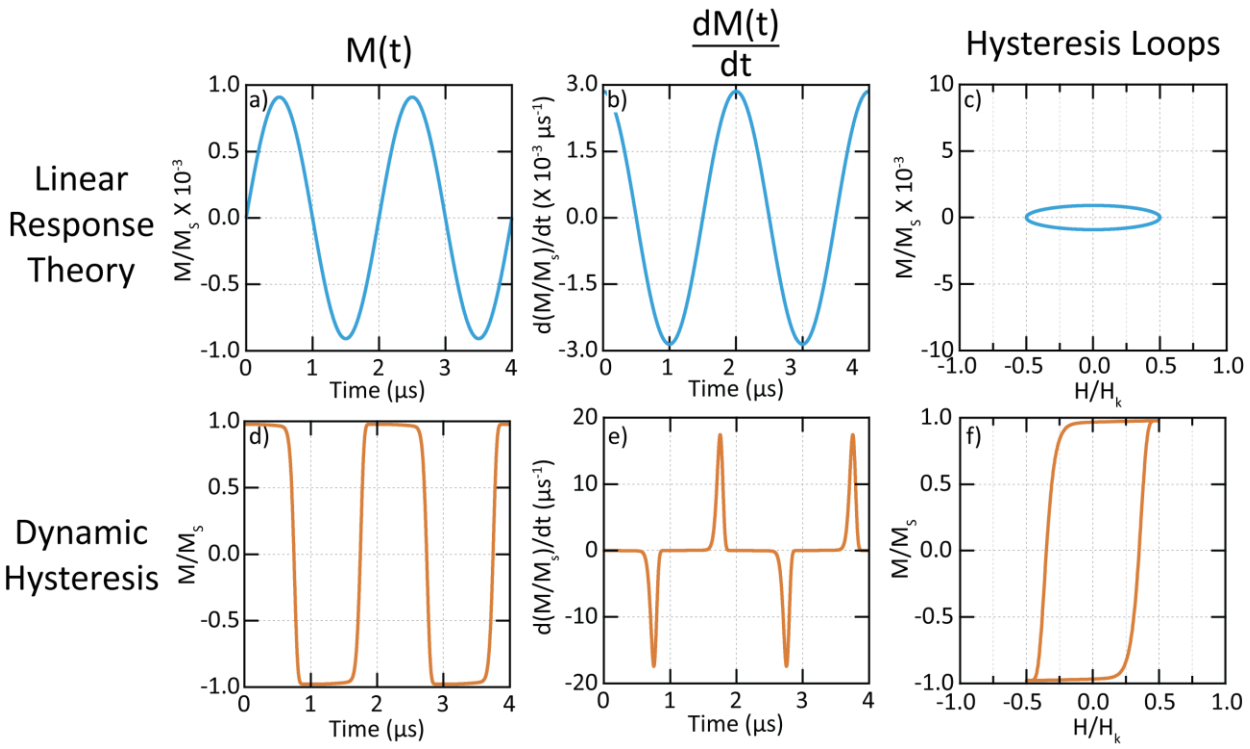

Figure 2.4 The predictions of linear response theory and dynamic hysteresis are contrasted for a case in which they exhibit major discrepancies. An MNP with $\boldsymbol{\sigma}$ = 15 is driven by an AMF with $\boldsymbol{H_0 = 0.5H_k}$ and $\boldsymbol{f = 500\text{kHz}}$. Linear response theory predicts sinusoidal (a) $\boldsymbol{M(t)}$ and (b) $\frac{\boldsymbol{dM}}{\boldsymbol{dt}}$, both with small amplitude. The corresponding hysteresis loop in (f) that is described parametrically by $\boldsymbol{M(t)}$ and $\boldsymbol{H(t)}$ is a tiny ellipse with $\boldsymbol{H_c \approx H_0}$. Dynamic hysteresis predicts non-sinusoidal (d) $\boldsymbol{M(t)}$ and (e) $\frac{\boldsymbol{dM}}{\boldsymbol{dt}}$, with a corresponding hysteresis loop that is square-like with $\boldsymbol{H_c < H_0}$.

Plotting hysteresis loops reveals a departure from the elliptical loops predicted by linear response theory, particularly at high field amplitudes (Figure 2.5). In the superparamagnetic regime, the result is curves that resemble the expected equilibrium magnetization curves of easy aligned MNPs with uniaxial anisotropy (Figure 2.5(c)). In the "ferromagnetic" regime, elliptical loops indicating limited response to low applied field amplitudes grow into large square-like loops as field amplitude is increased (Figure 2.5(e)). For the purpose of anticipating trends in MNP heating, the latter trend is especially important and contradicts the physical directive offered by linear response theory to tune the timescale of stochastic reversal to match the frequency of the AMF. In dynamic hysteresis, the MNPs that heat most effectively are in the

ferromagnetic regime and should be driven at amplitudes near the coercive field of the square like loops at the highest allowable frequency. This runs contrary to the perceived need for highly monodisperse, size-tuned MNPs because, within these models, H_k does not depend on volume (Equation 2.16). Combined with a systematic constraint such as the $H_0 f$ product limit, it is also highly suggestive of multiplexing. MNPs that can be designed with significantly different coercive fields should have distinct optimal driving conditions.

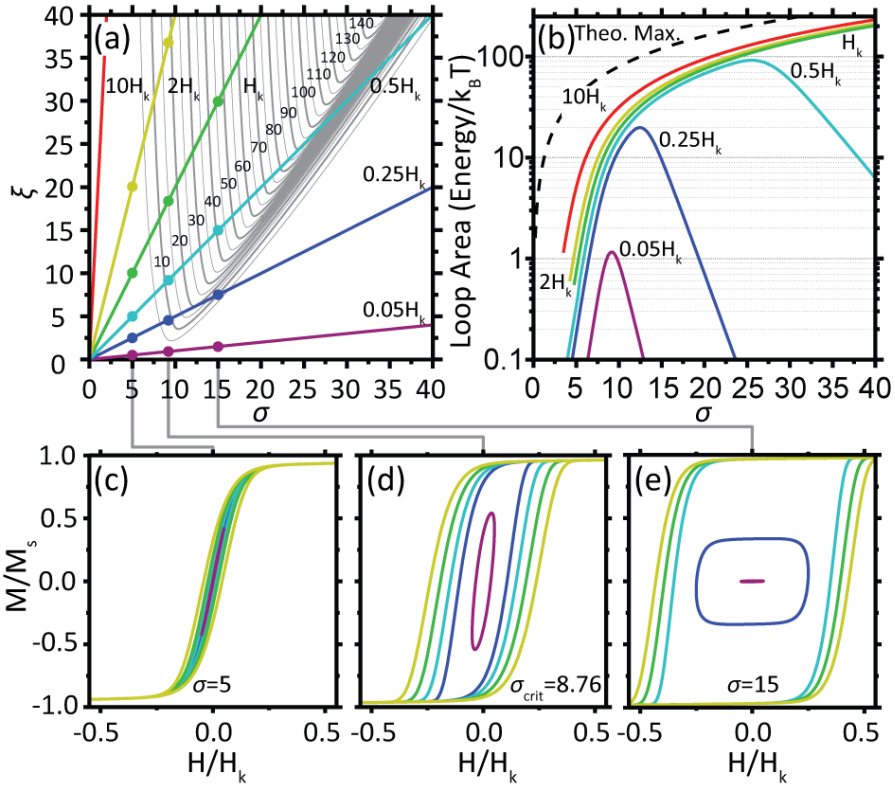

Figure 2.5 (a) Contour plot of hysteresis loop area as a function of σ and $\boldsymbol{\xi}$ for uniaxial anisotropy at 500kHz, superimposed with paths representing AMF amplitudes of different magnitude relative to $\boldsymbol{H_k}$. (b) Hysteresis loop area as a function of σ plotted along the paths in (a). The dashed line represents 8σ, the theoretical maximum predicted by Stoner-Wohlfarth theory at $\boldsymbol{T = 0K}$. (c)-(e) Simulated hysteresis loops for points in $\boldsymbol{\sigma}$-$\boldsymbol{\xi}$ space for representative $\boldsymbol{\sigma}$ values from the superparamgentic regime (c), ferromagnetic regime (e), and the $\boldsymbol{\sigma_{crit}}$ dividing them (d), which varies with frequency. Adapted from Christiansen et al.[51]

A further interpretation of the hysteresis loops in Figure 2.5 is that, while the growth to square-like hysteresis loops predicts higher heating rates in the ferromagnetic regime, it also

ultimately serves to bound the coercive field. One of the indirect effects of ignoring Zeeman energy in linear response theory is that the predicted power dissipation grows without bound as H_0 increases. In dynamic hysteresis, H_c is bounded to always be less than H_k, and is often considerably less. The commonly cited version of linear response theory only corrects susceptibility to ensure that the magnetization does not exceed the saturation magnetization (Appendix D), causing SLP to grow quadratically with H_0 for low amplitudes and linearly for high amplitudes.[63] These trends have straightforward geometric interpretations when the bounding on the axes of hysteresis loops is considered.

In order to gain a more generalized understanding of a model, it is sometimes helpful to develop an abstract representation on to which many material systems can be mapped. Such a representation for the results of dynamic hysteresis can be termed a "σ-ξ space." Figure 2.5 shows a σ-ξ space for 500 kHz and easy aligned MNPs with uniaxial anisotropy, a contour plot with its ordinate representing σ and its abscissa representing ξ_0. The values represented in the plot are areas of M/M_s vs ξ hysteresis loops, which can be interpreted as individual particle loss energy per cycle normalized to k_BT (Appendix E). Lines extending from the origin can be interpreted as paths of constant H_0/H_k along increasing σ values.

2.5 Stochastic Landau-Lifshitz-Gilbert Equation

A detail that was omitted from the basic physical picture of MNPs presented in Section 2.2, is that in addition to thermal fluctuation, their magnetic moments are thought to precess at high frequencies.[69, 70] One approach for modeling the AMF amplitude dependent dynamic response of MNPs is to consider a form of the Landau-Lifshitz-Gilbert (LLG) equation that incorporates the influence of thermal noise in its dynamical description of the precession of the magnetization vector $\vec{M}$ of an individual MNP.[60, 71]

$$\frac{d\vec{M}}{dt} = -\gamma_1 \vec{M} \times \left(\vec{H}_{eff} + \vec{H}_{th}\right) - \frac{\kappa\gamma_1}{M_s}\vec{M} \times \left[\vec{M} \times \left(\vec{H}_{eff} + \vec{H}_{th}\right)\right] \quad 2.20$$

Where

$$\gamma_1 \equiv \frac{\gamma}{1+\kappa^2} \quad 2.21$$

$\vec{H}_{eff}$ is the effective field, $\vec{H}_{th}$ is the thermal field, κ is a unitless damping constant, γ is the gyromagnetic ratio and can be expressed in terms of fundamental quantities as shown in Appendix F. Vector cross products are a common feature of dynamical equations for physical systems involving rotation, and the most intuitive way to understand Equation 2.20 is to separately consider the role of each term on the right-hand side. The first term drives simple precessional motion and the second term is responsible for damping. Including damping is essential because it allows the moment to be brought into alignment with the field and it also serves as a phenomenological mechanism of energy dissipation. By acting only through torques that are constructed by cross products to remain orthogonal to $\vec{M}$, this equation conserves the magnitude of $\vec{M}$. This coincides with the basic physical picture described in Section 2.2 of a single domain MNP undergoing coherent fluctuation and reversal.

$\vec{H}_{eff}$, the effective magnetic field, lumps together the influence of the externally applied field and magnetic anisotropy, which is usually assumed to be uniaxial. Though not made apparent by Equation 2.20, the influence of anisotropy dominates $\vec{H}_{eff}$ when H_0 is less than H_k, as should be expected for consistency between the models. (Appendix F offers additional details.) Acting to randomly jostle $\vec{H}_{eff}$ in a physically well-motivated way, the thermal field $\vec{H}_{th}$ varies stochastically and is defined according to its statistical properties. Treated as an initial value problem and propagating numerically, the net effect of these contributions is noisy

hysteresis loops for individual MNPs (Figure 2.6(c)) which can be averaged over a large population to produce hysteresis loops similar in shape to the ones predicted by dynamic hysteresis models (Figure 2.6(d)).

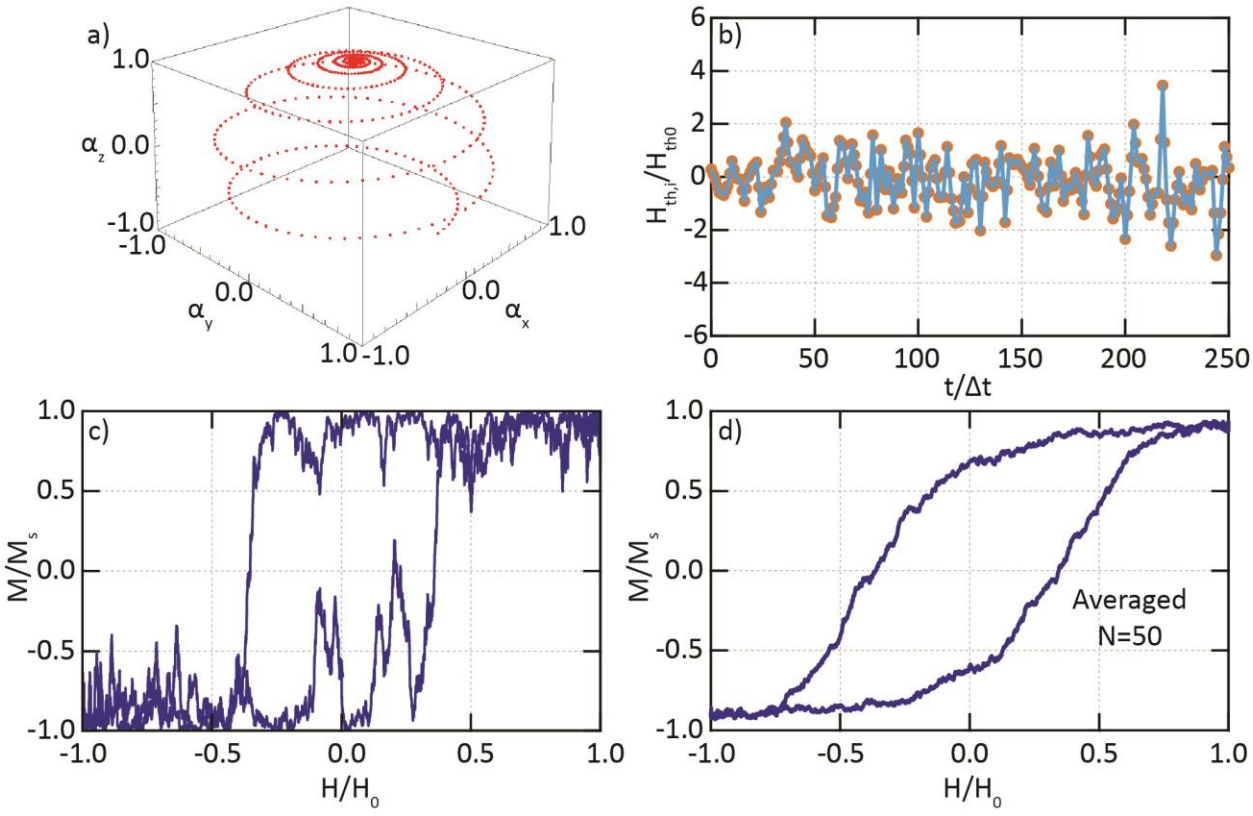

Figure 2.6 (a) Damped precession ($\boldsymbol{\kappa = 0.1}$) of the unit magnetization vector $\vec{\boldsymbol{\alpha}}$ of an MNP is shown as its moment is brought into alignment with an applied field in the $\boldsymbol{z}$ direction. This path was used to check the code for the numerical propagation using Equation 2.20 and does not include anisotropy or thermal noise. (b) An example of stochastic variation of the thermal field in the ith direction is shown, normalized to a quantity defined in Appendix F. (c) An example of a hysteresis loop produced under the influence of this stochastic fluctuation is shown, along with an average of 50 such loops in (d).

Recent work by Usov has shown that this model can be extended to include interparticle interaction by simulating large pseudorandom clusters of MNPs, including a term for their dipole-dipole interactions in $\vec{H}_{eff}$, and solving numerically.[72] By varying the packing fraction of MNPs and K_{eff}, this work suggests the existence of a strong interacting regime, in which

interparticle interactions dominate, a weak interacting regime in which they can be safely neglected, and an intermediate region between the two extremes. This can be understood intuitively in terms of Equation 2.20 by considering which contributions will dominate $\vec{H}_{eff}$. Based on this logic, it has been argued that the unitless quantity $K_{eff}/{M_s}^2$ is important for assessing the significance of interactions between MNPs. If this quantity is large, MNPs may effectively behave as weakly interacting, even at high concentrations.

2.6 Kinetic Monte Carlo Methods

An alternative model for studying the effects of interparticle interactions on hysteresis in clusters of MNPs employs kinetic Monte Carlo simulations.[73] Unlike the Stochastic LLG equation, this method does not describe precession or make use of a similarly explicit dynamical equation. A kinetic Monte Carlo approach consists of randomly seeding a space with non-overlapping MNPs, and then evolving the system stepwise in time pseudorandomly applying a weight function motivated by statistical mechanics that depends on the energy of the system. In this way, the energy scale of interaction is balanced by the entropic effects of thermal fluctuation. The energetic contributions considered in these models include interaction with the applied magnetic field, magnetic anisotropy, and dipole-dipole interactions between MNPs.

Unsurprisingly, square-like hysteresis loops are predicted in some conditions,[74] as with other theories that take into account both anisotropy and the energies of the MNP moments in the field. The influence of dipole-dipole interactions on these hysteresis loops can be counterintuitive. For instance, one kinetic Monte Carlo simulation, simulating the contents of a liposome, suggests that MNPs at the edge of an interacting cluster may heat differently than MNPs at the interior.[74] It might seem reasonable to suppose for some geometric distributions that the introduction of moderate dipole-dipole interactions could have an effect similar to increasing

the effective magnetic anisotropy. This can be shown straightforwardly in the case of two interacting MNPs (Appendix B), and there are some cases simulated by Monte Carlo methods where increased MNP concentration does this seem to produce similar behavior to increasing K_{eff}. However, in the limit of strong interactions, where concepts of long range order between MNPs begin to be relevant, the situation is sufficiently complex that conclusions should not be hastily drawn. Kinetic Monte Carlo methods offer a powerful tool for systematically investigating such systems.

2.7 Discussion of Relative Merits and Limitations of the Models

Despite its widespread use, special care must be taken to employ linear response theory only within its domain of validity. Experimental evidence for significant departures from linear response theory can be readily observed from trends in specific loss power as a function of applied AMF amplitude (Figure 2.7),[51] as well as direct observation of non-elliptical hysteresis loops through methods such as AC magnetometry.[75, 76] Nevertheless, linear response theory provides a valuable starting point for making sense of the behavior anticipated by improved models.

The similarity in the square-like shapes of the hysteresis loops predicted by stochastic LLG, dynamic hysteresis, and kinetic Monte Carlo treatments at high applied field amplitudes should not be interpreted as arbitrary or accidental. Key parallels between these models are discernable in the features that describe a barrier to reversal being reduced through the influence of an applied AMF and overcome through thermal fluctuation. In this sense, these models can perhaps be interpreted as dynamical elaborations of the classic Stoner Wohlfarth problem[77] at nonzero temperatures. Depending on the particular physical circumstances under investigation, some models may be more appropriate than others. Dynamic hysteresis is limited to low MNP

concentrations and frequencies where precession can be safely neglected. Kinetic Monte Carlo methods are similarly appropriate in cases where precession can be neglected, but interactions between MNPs are a prime concern. Most general, yet still deeply phenomenological, is the use of the LLG equation with a stochastic thermal term, which is valid in principle up to frequencies where a description of precession is necessary.

The internal and mutual consistency of these models is interesting, and further elaboration on their convergence upon one another would be intriguing from a theoretical perspective.[68, 69] However, in this work, these models are used with the explicit intent of informing engineering decisions, and their relative merits should be considered in that context. Dynamic hysteresis, despite its somewhat narrower yet still relevant domain of validity, is sufficiently simple that it can easily and quickly be implemented over a σ-ξ space as discussed in Section 2.4. Fu8ndamentally, this is because dynamic hysteresis models already incorporate results from statistical mechanics. In contrast, kinetic Monte Carlo or stochastic LLG require averaging over repeated numerical simulation for each hysteresis loop.

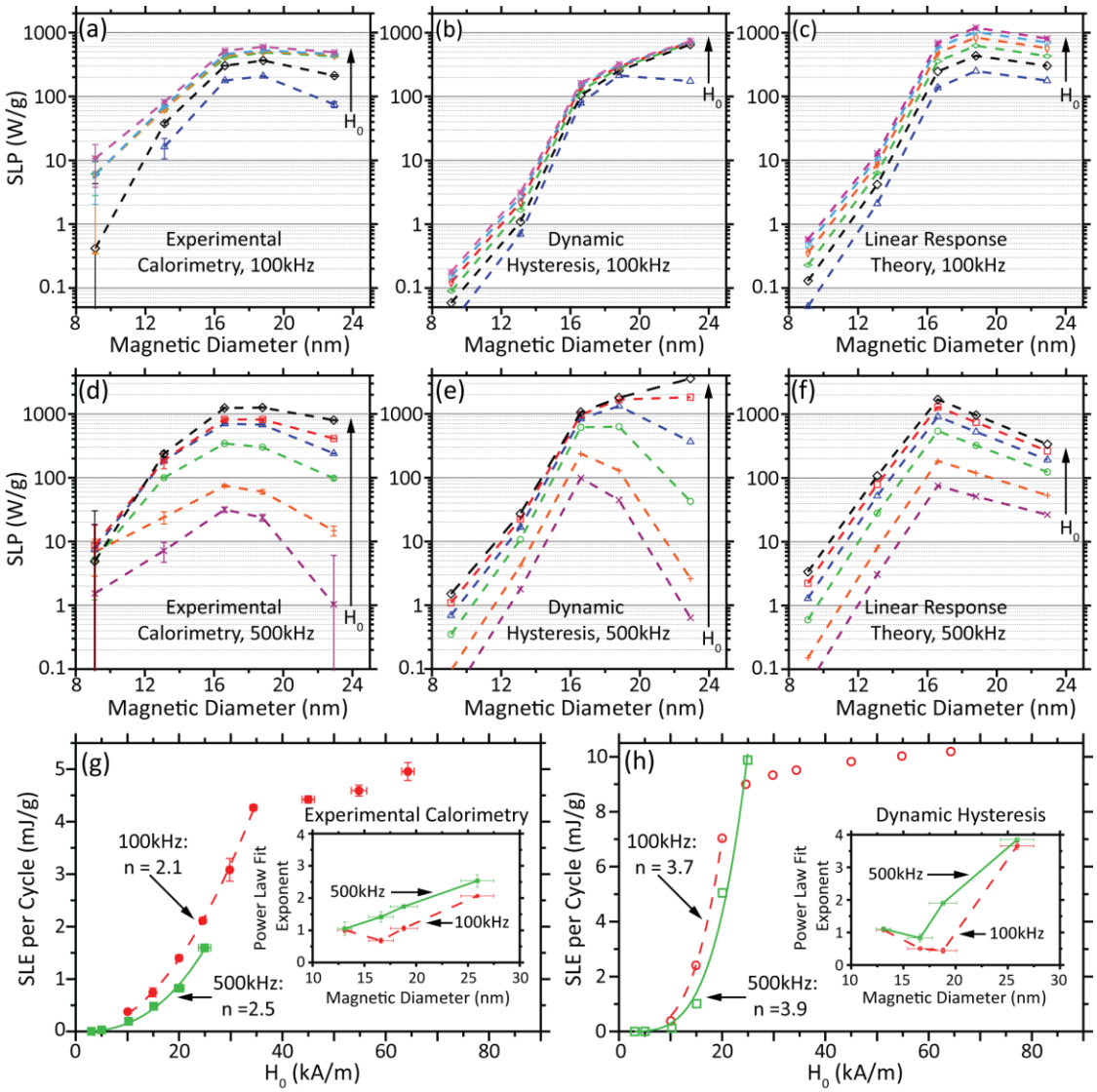

Figure 2.7 (a) Experimental calorimetry data for SLP vs. diameter with increasing field amplitude is compared against the predictions of dynamic hysteresis and linear response theory simulations. (a)-(c) are for various field amplitudes at 100kHz, and (d)-(f) are for 500kHz. × 3kA/m, + 5kA/m, ○ 10kA/m, △ 15kA/m, □ 20kA/m, ◇ 25kA/m, ⬠ 35kA/m, ⧫ 45kA/m, ▷ 55kA/m, and ✳ 65kA/m (all ±<3% in experiment). (a) and (b) show experimental calorimetry data, with vertical error bars representing the standard deviation of five trials. (b) and (e) represent the results of a dynamic hysteresis simulation taking into account measured magnetic diameter and assuming a Gaussian distribution of diameters with the same variance as the physical diameters. (c) and (f) represent the result of a linear response theory simulation with the same measured input parameters. (g) and (h) show specific loss energy versus AMF amplitude data for the MNP from (a)-(f) with the largest diameter, measured experimentally and modeled with a dynamic hysteresis simulation, respectively. Note the appearance of a plateau in both plots that is not predicted by linear response theory. The inset plots of (g) and (h) compare power law fits of initial SLE vs. H_0 curves. Adapted from Christiansen et al.[51]

2.8 Predicted Feasibility of Magnetothermal Multiplexing with Different Models

Considering loss powers subject to the constraint provided by physiological limitations on the AMF that can be safely applied to the body results in the prediction of a unique maximum, regardless of the particular model being used. This can be deduced from several observations:

1. All of the models predict that, at any given frequency, loss energy per cycle should increase monotonically with field amplitude. A model predicting shrinking hysteresis loop area in response to increasing AMF amplitude would be nonphysical.
2. For a given loss energy per cycle, loss power is proportional to frequency. Thus in the limit as frequency goes to zero, so too must loss power.
3. Although this thesis makes use of a particularly simple statement of the physiological limit in the form of a $H_0 f$ product, it may be more generally asserted that such a constraining function necessarily stipulates lower amplitudes at higher frequencies. Thus, in the limit of high frequencies, when combined with observation 1, allowable loss powers must decrease.

Together these observations imply that by constraining AMF conditions to physiologically acceptable field amplitudes, loss powers tend to zero in the limit of both low frequencies and high frequencies. Somewhere in between these limits, a maximum or maxima must occur, and given the monotonic increase of specific loss energy with AMF amplitude and monotonic decrease of acceptable AMF amplitudes with frequency, there should exist a simple maximum. Both linear response theory and dynamic hysteresis predict the existence of such maxima (Figure 2.8), but the reasoning that predicts them differs substantially between the two models, with direct consequences for the projected feasibility of magnetothermal multiplexing.

An essential characteristic of MNPs suitable for multiplexing is *selectivity*, as defined in Section 1.5. As will be discussed in Section 5.4, for bulk heating applications it is useful to consider a definition of selectivity that is concentration invariant. This greatly simplifies analysis of the functional dependence on H_0 and f to assess the possibility for selectivity with the two models, because it allows the SLP curves to be normalized. As is explained in Appendix G, for linear response theory, optimization subject to these constraints consists of selecting distributions of MNPs with σ values centered on the two frequencies. If even a small amount of polydispersity in σ is accounted for, far less than most real MNPs samples would exhibit,[78] the outlook for selective heating is dim (Figure 2.8(a)). In contrast, dynamic hysteresis suggests that a multiplexing set should make use of MNPs in the ferromagnetic regime, but their σ values could be similar or even identical provided that their coercive fields are substantially different. Even permitting a wider distribution of σ values than the linear response case, the possibility of multiplexing predicted by dynamic hysteresis is substantially unaltered (Figure 2.8), largely due to the fact that its principle of optimization is based on H_c rather than σ (Appendix G). Figure 2.9 shows experimental calorimetry data corroborating the assertion that selective bulk heating is possible.

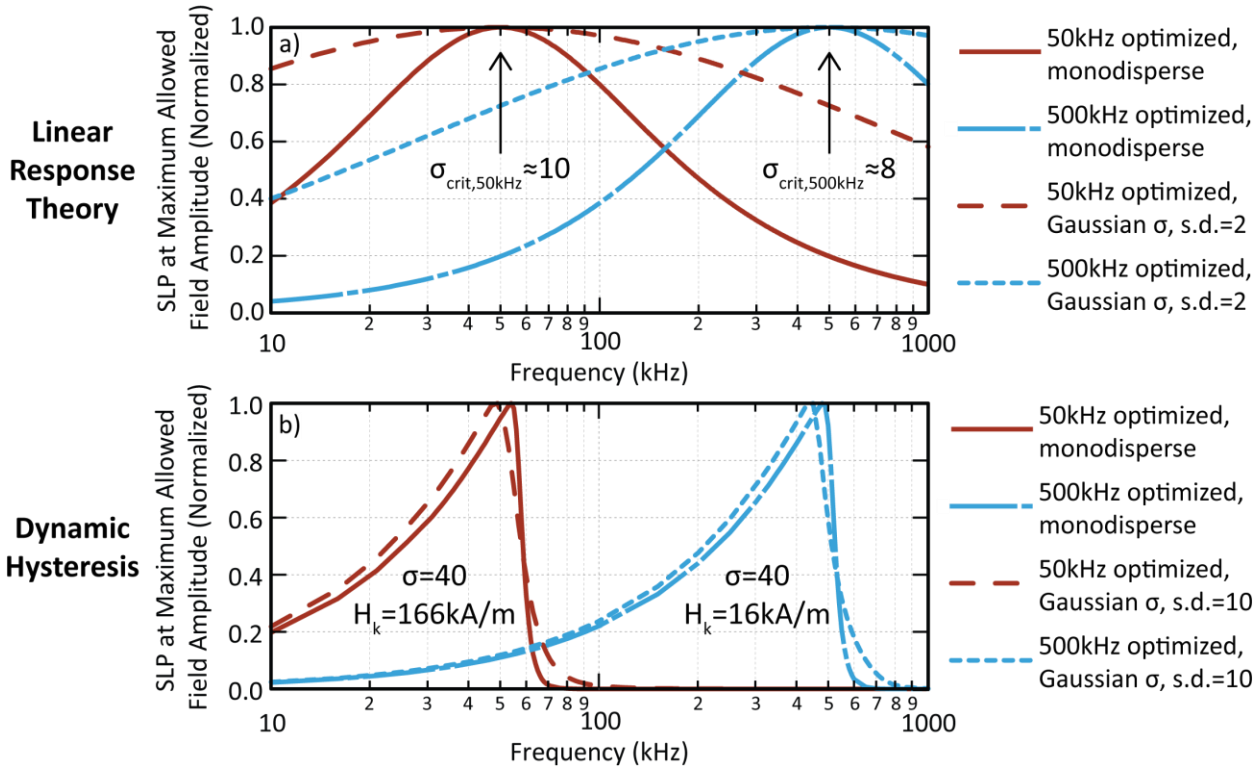

Figure 2.8 The differences between linear response theory and dynamic hysteresis in predicting the feasibility of selective bulk heating are shown. (a) Using the principles of optimization suggested by linear response theory, idealized monodisperse MNP sets are selected for preferred operation at 50kHz and 500kHz. Considering the influence of polydispersity by assuming Gaussian distribution functions in $\boldsymbol{\sigma}$ centered at these values with a standard deviation of 2 dramatically reduces the feasibility of multiplexing. (b) MNP sets with identical distributions of $\boldsymbol{\sigma}$, but distinct $\boldsymbol{H_k}$ values are predicted by a dynamic hysteresis model to offer a comparatively feasibly option for selective heating. Introducing polydispersity by assuming Gaussian distribution functions with a standard deviation of 5 does not substantially alter the feasibility of selective heating.

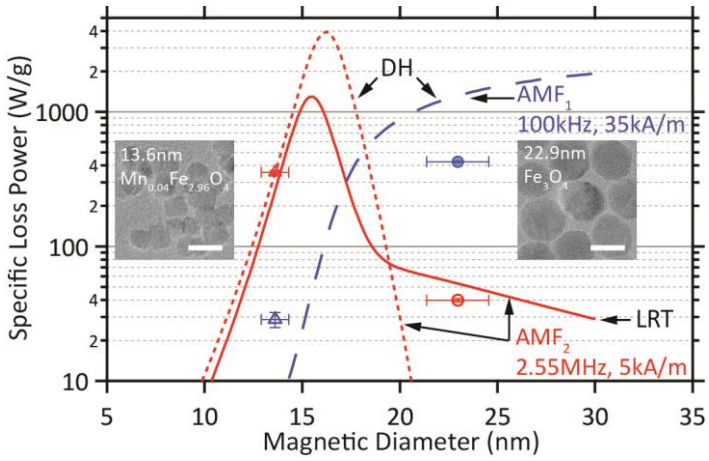

Figure 2.9 A preliminary demonstration of multiplexed SLP values, unconstrained by the $\boldsymbol{H_0 f}$ product is shown. The samples consisted of superparamagnetic $Mn_{0.04}Fe_{2.96}O_4$ MNPs with $\boldsymbol{d_m = 13.6nm}$ (▲ for AMF_1 and △ for AMF_2) and a "ferromagnetic" Fe_3O_4 MNPs with $\boldsymbol{d_m = 22.9nm}$ (○ for AMF_1 and ● for AMF_2). The solid line is a linear response theory simulation for Fe_3O_4 MNPs of varying diameter driven by AMF_1 including Brownian relaxation. The dashed lines correspond to DH simulations for the same SDMNPs driven by AMF_1 (long dash) and AMF_2 (short dash). TEMs of the samples are shown. Scale bars are 20nm. Adapted from Christiansen et al.[51]

The doubt that Figure 2.8 casts on the ability of linear response theory to predict the feasibility of selective bulk heating may be safely extended to nanoscale heating as well. The underlying issue, a need to sensitively tune σ combined with polydispersity, would have the same effect in this situation as well. However, the argument and evidence pertaining to selective bulk heating as predicted by dynamic hysteresis cannot necessarily be extended to nanoscale heating without further analysis because nanoscale heating does not benefit from the possibility of adjusting concentration. Fortunately, the reasoning is made straightforward by considering hysteresis loops in M/M_s versus ξ, which have an area proportional to individual particle loss energy per cycle (Appendix E). When $H_0 < H_c$, the magnetization is unable to respond appreciably and negligible heat dissipation is expected. When $H_0 > H_c$, loops have a roughly consistent area, regardless of the frequency. Figure 2.10(a)-(c) demonstrates that dynamic hysteresis models predict the feasibility of multiplexed IPLPs with substantially distinct H_k.

Figure 2.10(d)-(f) uses hysteresis loop representations to show the underlying logic. By scaling the ξ axis by the frequency, the visual area of the loops is proportional to loss *power* rather than loss *energy* per cycle. In short, this representation shows that magnetothermal multiplexing with IPLPs can be interpreted as a straightforward scaling relationship imposed by the $H_0 f$ constraint in hysteresis loops with different H_c values.

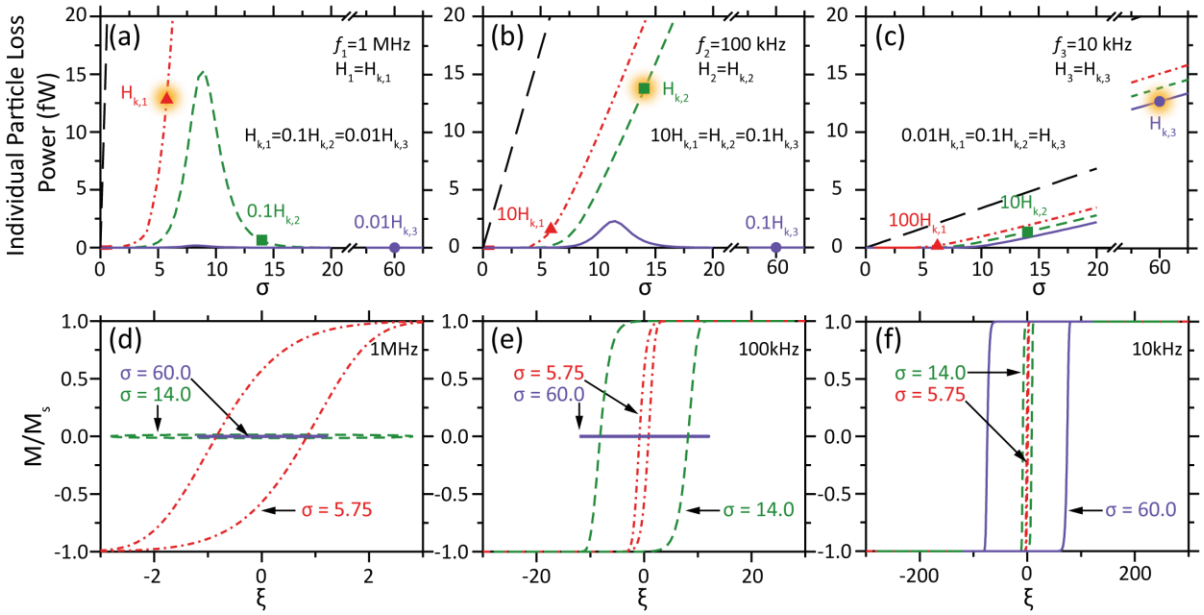

Figure 2.10 (a) Simulated IPLP for SDMNPs driven by an AMF at 1MHz and amplitude $\boldsymbol{H_0 = H_{k,1} = 0.1H_{k,2} = 0.01H_{k,3}}$. Dash-dot-dash, dashed, and solid lines correspond to low ($\boldsymbol{H_{k,1}}$), medium ($\boldsymbol{H_{k,2}}$), and high ($\boldsymbol{H_{k,3}}$) coercivity materials, respectively. Markers represent σ values of SDMNPs selected from each set for multiplexing. The long black dashed line represents 8σ, the theoretical maximum. (b) Analogous plot for an AMF of amplitude $\boldsymbol{H_0 = H_{k,2}}$ at 100kHz. (c) Analogous plot for an AMF of amplitude $\boldsymbol{H_0 = H_{k,3}}$ at 10kHz. (d)-(f) Simulated hysteresis loops for the SDMNPs selected for multiplexing at the AMF conditions corresponding to the plots in (a)-(c), respectively. Numerical area of the $\boldsymbol{M/M_s}$ vs. ξ loops is equal to individual particle loss energy per cycle normalized to ambient thermal energy. The axes are rescaled such that the graphical area is proportional to IPLP. From Christiansen et al.[51]

3 Design of Alternating Magnetic Field Coils and Associated Electronics[††]

3.1 Challenges in Generating Alternating Magnetic Fields

In conducting biological experiments or materials characterization involving heat dissipated by MNPs, generating an AMF is a crucial experimental hurdle. Commonly, researchers conducting these experiments either buy systems to do this or have them custom made. The result typically resembles induction furnaces with large power requirements and fixed operating frequency.[37, 79] Designing AMF setups for the experiments described in this thesis played a role in helping to guide the thought process that led to the idea of magnetothermal multiplexing and averted adoption of the discouragingly prominent misconception that such setups irradiate samples with radiofrequency electromagnetic waves.[19] For a detailed justification of the well-motivated applicability of the magnetoquasistatic approximation of the setups discussed here, see Appendix H.

Given the magnetoquasistatic character of these setups, it may seem counterintuitive that reaching amplitudes meeting the $H_0 f$ product limit can be challenging; after all, static magnetic fields with magnitudes far exceeding the desired AMF amplitudes are readily and routinely produced in the laboratory. Such a view neglects the role of inductance and the basic consequences of alternating magnetic flux. Many of the proven strategies that offer strong static magnetic fields in the laboratory, such as designs with many turns of wire or yokes made of soft ferromagnetic alloys having high saturation magnetization, would utterly fail if they were forced to operate at 100s of kHz. Their high inductance would necessitate tremendous voltages for even modest currents, potentially exceeding the dielectric breakdown strength of their components. Even before this point of failure could be reached, the heating of the conductive yoke would

[††] The structure and content of this chapter is based largely on a manuscript submitted to *Review of Scientific Instruments*. Some aspects of the discussion have been condensed or expanded where appropriate.

severely limit accessible amplitudes. Generating suitable AMF conditions is feasible, but design strategies must be appropriately adapted to respond to these challenges.

Generating a static magnetic field in a small working volume is far easier than doing so for a large working volume, and this trend is even more pronounced for AMFs (Section 3.6). The comparative feasibility of small setups permits simple, inexpensive strategies to be employed at the scale required for materials characterization or *in vitro* work (Figure 3.1). Enlarging working volumes to encompass *in vivo* animal models requires markedly different design strategies, such as resonant tank circuits (Figure 3.1). There is only one published setup that generates an AMF at the scale of humans intended to reach similar amplitudes, and its performance and design arguably leave room for significant improvement.[80] Though only occasionally acknowledged,[28] the difficulty of scaling up AMFs ought to receive greater attention. Left unaddressed, the problem could act as a bottleneck in translating a wide variety of research on MNPs to a clinical setting. From a systems level perspective, materials design of the MNPs and AMF setup design could potentially inform one another. Indeed, the idea of magnetothermal multiplexing arose partly from these kinds of considerations.

The intent of this chapter is to communicate design principles with sufficient clarity to enable others to reproduce and improve upon the setups that have supported the work presented in this thesis, and to provide a useful conceptual starting point for bringing AMFs to clinically relevant scales (Figure 3.1). The keenly interested reader should refer to the appendices where indicated for useful details.

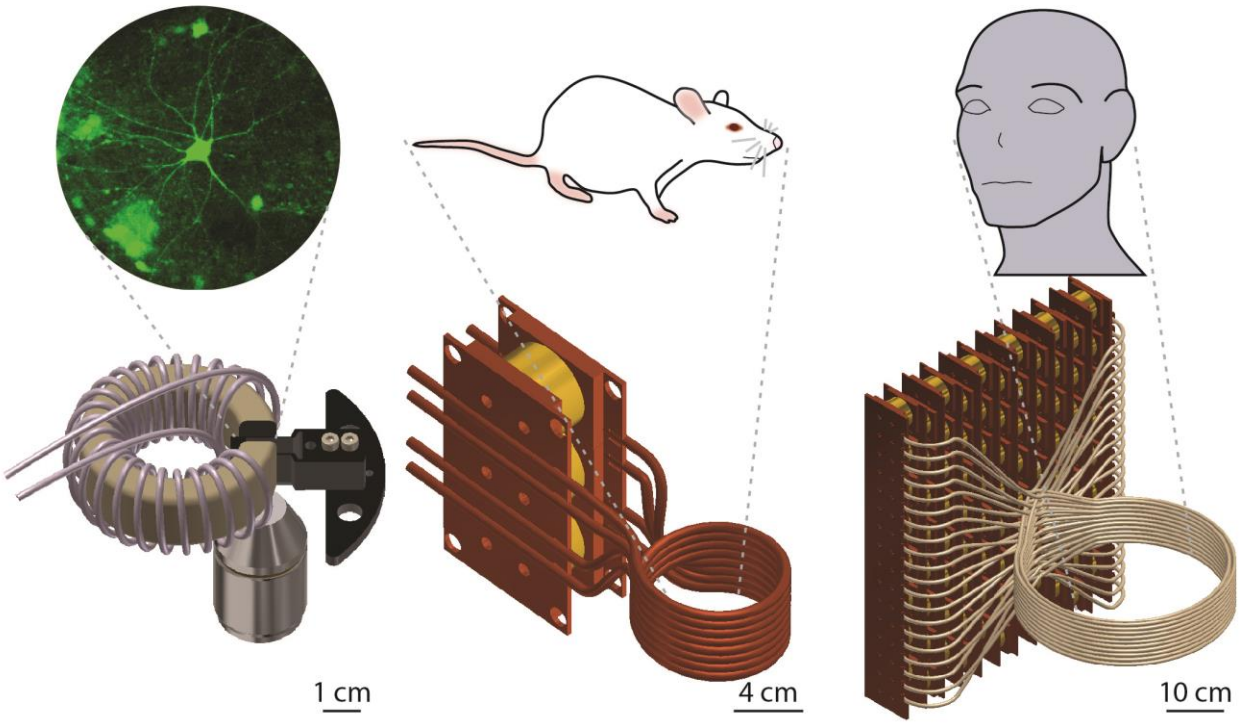

Figure 3.1 Design strategies vary with the scale of the intended working volume. A graphical overview of the progression of designs explored in this chapter is shown.

3.2 Justifying the Use of Cored Electromagnets

In an electromagnet, the introduction of a soft ferromagnetic core allows wire to be wrapped around a long, highly permeable section of a flux path. If this path forms a closed loop broken only by a small air gap, such as a gapped toroid, then its overall reluctance will dominated by that gap. Provided that the gap is small compared to the path length of the core, the magnitude of the magnetic field is reasonably uniform (Figure 3.2(a)) and closely approximated by a simple expression.

$$H_g \approx \frac{NI}{w} \qquad 3.1$$

Here, H_g is the field in the gap, N is the number of turns, I is the current, and w is the gap width. (Appendix I explains the basis of this approximation for a toroidal geometry.) To clarify how this can reduce the power required to reach a desired magnetic field amplitude, this dependence can be compared to the familiar case of a long current-carrying solenoid and the field that it produces H_s, which is also reasonably uniform within the working volume. This field is proportional to the number of turns per unit length N/L and the current I.[81]

$$H_s = \frac{NI}{L} \tag{3.2}$$

One can imagine bending the long solenoid and slipping it over the gapped toroidal core to serve as the windings of an electromagnet, while keeping its current constant (Figure 3.2 (b)). The simplicity and similarity of the expressions in Equations 3.2 and 3.3 allow for a comparison of the field resulting from the two designs in the form of a ratio.

$$\frac{H_g}{H_s} = \frac{L}{w} \tag{3.3}$$

For a gap that is small compared to the circumference of the toroid, this ratio is large. The magnetic field magnitude has therefore been strengthened, though restricted to a smaller volume. In order to reach a targeted magnetic field magnitude, the necessary current is reduced by the same factor, which also reduces the required power. The same is true of other gapped flux path geometries, and the design advantage can be visualized as the core providing a mechanism by which the integrated current required to reach a particular magnetic field magnitude can be spread over a larger area, reducing current density and with it the dissipated power.

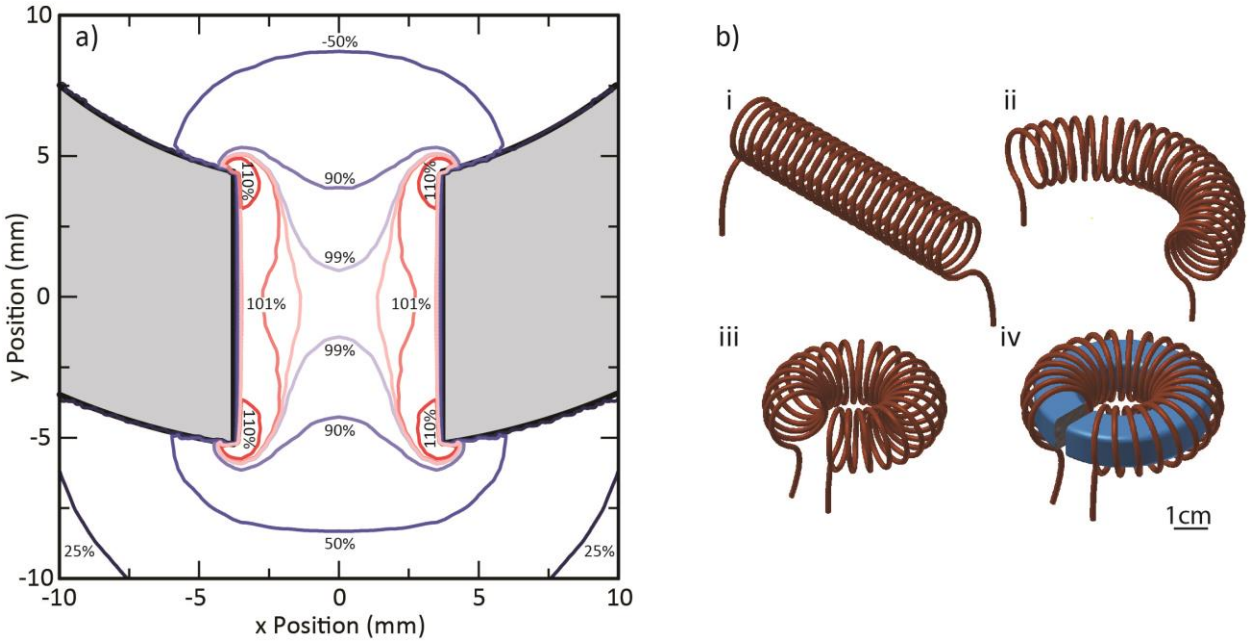

Figure 3.2 Detail of the gap region of a magnetostatic planar finite element model of an electromagnet with a 7.5mm gap and nonlinear B vs H manufacturer data for 3F3 at 25˚C. Magnetic field magnitude is shown relative to the mean magnetic field in the gap (25kA/m) to assess uniformity. (b) A representation of an imagined stepwise deformation of a long solenoid into the windings of gapped toroidal electromagnet is shown.

In the magnetostatic case, for field magnitudes below the saturation magnetization of a core, the advantage of using a core for an electromagnet is clear. The situation can be less straightforward at high frequencies. One consequence of an alternating flux is significant waste heat dissipated in the core through hysteresis or eddy currents, often far more than the Joule heating of the wires. A core can still offer an advantage, but this is contingent on the scale of the electromagnet, proper selection of core material, and the design of the flux path.

3.3 Practical Considerations for Small Scale Coils

Undesirable heating of the core is the main source of practical limitation in attempting to operate AMF electromagnets, especially when experiments are sensitive to heat. The dependence of power dissipation on flux, combined with the poor thermal conductivity of ferrites, can lead to

observable hot spots for uneven flux distributions (Figure 3.3). The impact of heat dissipation in the core can be mitigated through a combination of design and experimental practice. Active cooling with water circulated from an ice bath can help offset the dissipated heat. Combined with consistent duty cycling and a well-insulated sample holder, these electromagnets can be used for sensitive measurement of MNP heating rates with low background. (See Section 4.4 for additional details.) A wide variety of ferrite ceramic materials suited for power magnetics is readily available, and careful material selection can reduce dissipated heat.[82] Of the options tested, it was concluded that Epcos' N87 dissipated the least heat in the frequency range 100kHz to 750kHz (Appendix J).

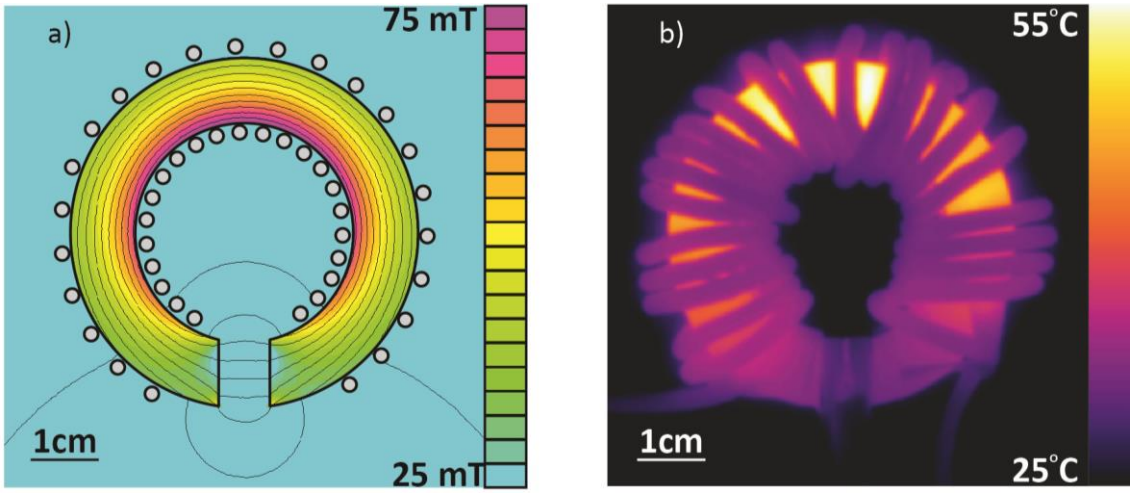

Figure 3.3 (a) Magnetostatic planar finite element model of flux distribution in the core of a Ferroxcube 3F3 toroid (TX51/32/19) with a 7.5mm gap and magnitude 16kA/m at center of gap. (b) Infrared thermograph of uncooled electromagnet operating with 16kA/m amplitude in the gap at 500kHz after 30 seconds. Note correlation of core temperature with flux density.

Figure 3.4(a) summarizes the maximum field amplitude used in standard operation as a function of frequency for several designs, as compared to the $H_0 f$ product clinical limit discussed earlier. For electromagnets based on metal powder cores, operation was limited to the low tens of kilohertz, due to eddy current losses. Though falling below the $H_0 f$ limit, the electromagnet shown in Figure 3.4(b) can reach amplitudes of up to 130kA/m at 16kHz. In the

hundreds of kilohertz, power ferrite cores like the one shown in Figure 3.4(c) can easily meet or exceed the limit. Although suitable ferrites for similar designs that operate near or above 1 MHz do exist[82] and were tested up to 2.5MHz, it was found that the benefits of using of a core diminish at these frequencies. As the required current to reach the conditions suggested by the $H_0 f$ product limit shrinks, so too does the power savings realized by using a core, and soon a litz wire design becomes favorable because it can be cooled more effectively. One such geometry is shown in Figure 3.4(d) and Figure 3.4(e) and is intended to maintain the same field direction and homogeneity as the designs incorporating cores while reaching frequencies as high as 2.5MHz. It employs a conical spiral of litz wire held by a 3D printed wire guide with a pitch selected to make it a geometric approximation of superimposed Helmholtz coils with increasing diameter.

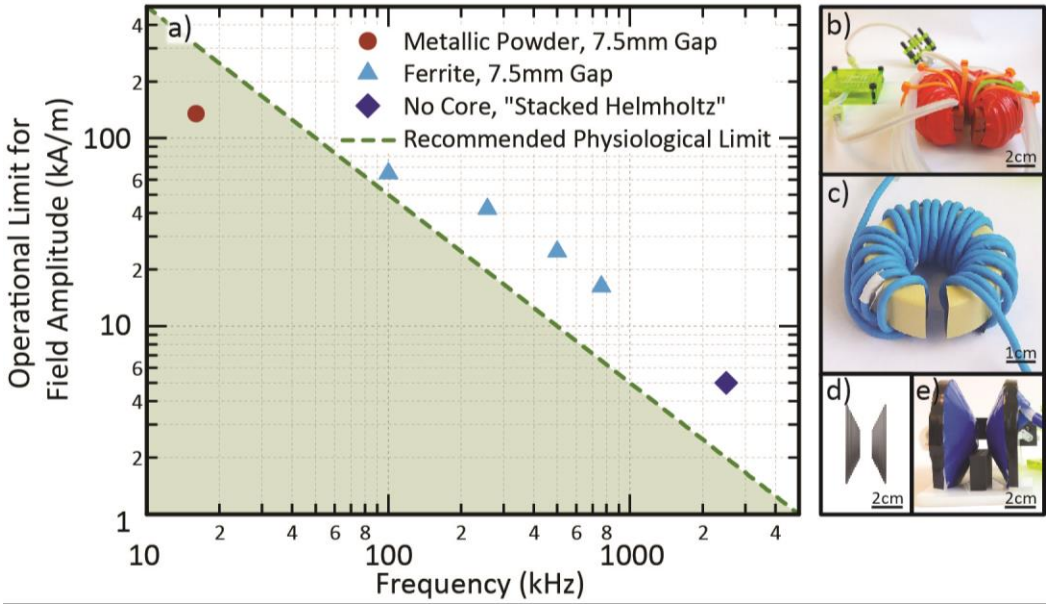

Figure 3.4 (a) Summary of normal operating conditions relative to one commonly stated $\boldsymbol{H_0 f}$ product limit, $\boldsymbol{5 \times 10^9 A\, m^{-1} s^{-1}}$ (b) Electromagnet for 16kHz operation with two stacked Magnetics Inc. MPP cores (Part number C055866A2) with a 7.5mm gap (c) A Ferroxcube 3F3 ferrite core (TX51/32/19-3F3) with a 7.5mm gap wrapped with insulated litz wire (d) Sketch of wire geometry for a stacked Helmholtz coil (e) Stacked Helmholtz coil incorporating 3D printed wire guides.

3.4 Series Resonant Circuits for Cored Electromagnets

Straightforward resonant circuits can be used to drive the AMF electromagnets pictured in Figure 3.4. Since incorporating a core both increases inductive reactance and reduces the required current for a design incorporating many turns of litz wire, this suggests the need for series rather than parallel resonance. For this purpose, arrays of surface mounted high voltage mica capacitors with negligible equivalent series resistance may be used. The withstanding voltage required by this array can be estimated by accounting for the current required by Equation 3.1, the resonance frequency, and the overall capacitance value.

A circuit similar to the one shown by LaCroix et al.[83] can be used to step up the current supplied by a broadband amplifier designed for 50Ω loads. (An Electronics and Innovation 1020L amplifier was used in this thesis.) A schematic with simplified nonideal component models is shown in Figure 3.5(a), along with a representative photograph of the circuit in Figure 3.5(b), and a nonideal transformer model in Figure 3.5(c). Simulations based on this model with measured component values appear to reproduce measured impedance values at low fluxes (Figure 3.5(d)). The resonant frequency can be adjusted over a wide range by selecting different capacitance values for the resonant capacitor C in the secondary circuit (Figure 3.5(e)).

One of the advantages offered by a series circuit is the feasibility of rapidly switching between different operating conditions. This is an essential capability for preliminary multiplexing characterization and demonstration experiments in which a sample is exposed to one AMF condition and then another in rapid succession. Through the use a dual set of relays, the circuit can be made to rapidly switch between transformer ratios and resonant capacitances. (Figure 3.5(f)).

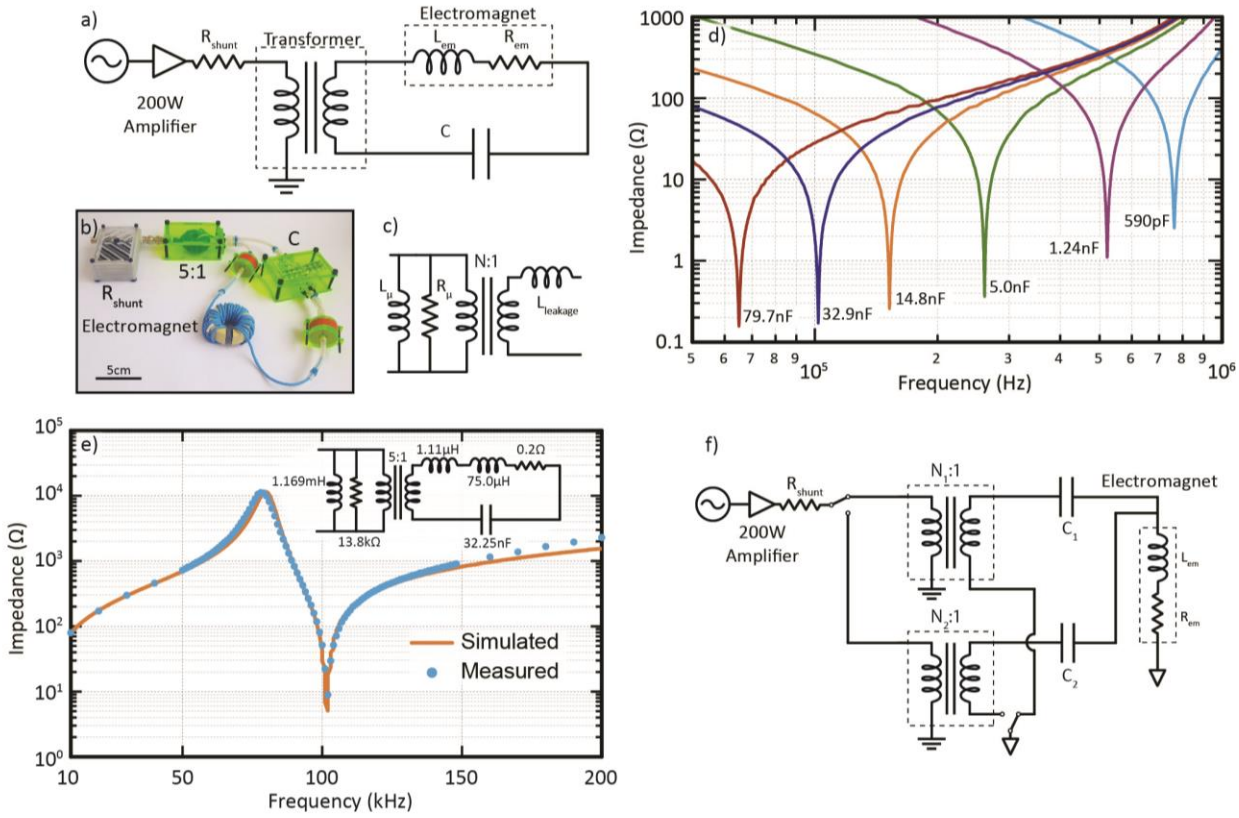

Figure 3.5 (a) Simplified schematic for circuit driving AMF electromagnets with cores (b) Photograph of representative circuit (c) Model of nonideal transformer (d) Resonances of the same electromagnet placed in series with various capacitor arrays (e) Simulated low current impedance of a model based on measured component values is compared to impedance versus frequency measurements. (f) A schematic shows how relays can be used to rapidly switch resonant capacitors and transformers. This is valuable for any experiment investigating multiplexing that requires exposing samples to multiple AMF conditions in quick succession.

3.5 A Design for *In Vivo* Experiments in Anesthetized Rodents

For applications such as calorimetry or optical microscopy *in vitro*, experiments where a uniform field within the working volume is desirable and concentrating waste heat far from the gap is not problematic, the flux distribution and associated heating shown in Figure 3.3 is acceptable. Other designs can use wider gaps to extend working volume to superficial targets in small animal models as shown in Figure 3.6(a). Widening the gap sacrifices uniformity and amplitude (Equation 3.1), but the field drops off more gradually with distance from the core as shown in Figure 3.6(b).

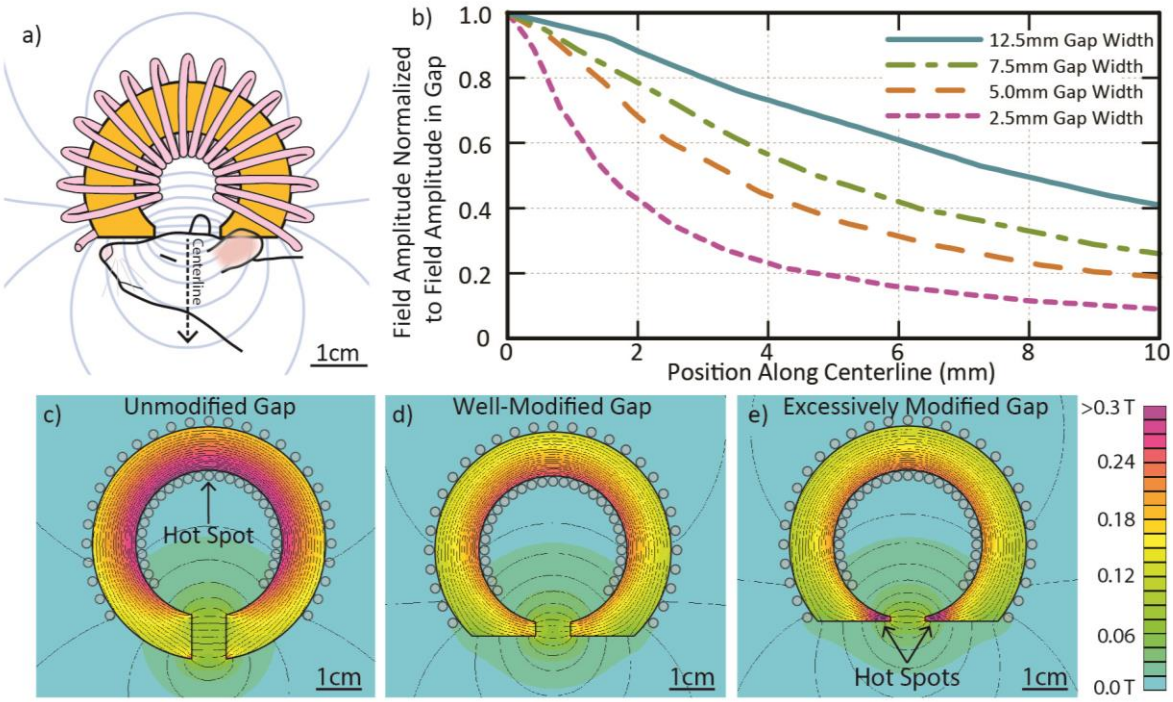

Figure 3.6 (a) Sketch of design incorporating wider gap to access shallow targets, e.g. in small anesthetized animals. (b) Magnetic field amplitude along centerline away from gap normalized to magnetic field magnitude at center of gap (c) Flux distribution for unmodified 7.5mm gap in 3F3 core (TX51/32/19-3F3) with 65kA/m amplitude at center. (d) Flux distribution for a core with an optimally placed additional cut operation, but otherwise identical. (d) Flux distribution resulting from a cutting operation removing more than the optimal amount of material.

In such cases, it is also worthwhile to consider further modifying the core in order to favorably influence the distribution of flux. Homogenizing flux in the core at high amplitudes reduces overall power dissipation, allowing for more aggressive duty cycles. The flux in the core can be made more uniform in the case of a gapped toroid simply by adding an additional cut perpendicular to the gap, indicated in Figure 3.6(c)-(e). The best position for this additional cut varies with gap width; removing an optimal amount of material from the gap increases its reluctance sufficiently to reduce the flux on the opposite side of the electromagnet (Figure 3.6(d)). Removing too much material concentrates flux near the gap, resulting in an increased heating in the vicinity of the working volume (Figure 3.6(e)). An alternative method to homogenize the flux in the core of an electromagnet with a gap is to employ symmetric flux

paths such as E cores in which the material closest to the gap is likely to experience the largest flux (Appendix J).

3.6 Scalability Limitations to Cored Electromagnets

Having both justified and demonstrated the practical advantage of using a gapped core to produce AMF amplitudes in a $1cm^3$ working volume with less dissipated power than coreless alternatives would have required, it may be tempting to imagine scaling up such designs to working volumes large enough to hold research rodents or human subjects. Doing so is inadvisable, and it is possible to show this analytically. Scalability of inductors and transformers with cores has been well-studied,[84-86] typically in the context of maximizing stored or transferred energy. A similar analysis can be conducted that considers the consequences of maintaining the same *AMF amplitude* in designs with and without cores as working volume increases. This constraint results in somewhat different design tradeoffs than the same analysis with more typical goals in power electronics would suggest.

Compare a hypothetical electromagnet with a core and a coreless solenoid as they are uniformly scaled up by a factor ϵ, and forced to maintain the same target AMF amplitude in the working volume. Power dissipation by the core and field amplitude depend on distributions of flux density and current density, and this thought experiment of simple scaling without altering the number of turns can be viewed as an analytical expedient to scaling these more fundamental quantities.

In the case of a coreless coil, due to the geometric dependence of the Biot-Savart law,[81] the new current I_ϵ would need to increase by the factor ϵ in order to maintain the same AMF amplitude.

$$\frac{I_\epsilon}{I} = \epsilon \tag{3.4}$$

Scaling up the windings also reduces their resistance R to a new value R_ϵ. In conditions when the full cross sectional area of the wire is expected to be utilized, such as when appropriate litz wire is selected,[87] scaling up the coil reduces its resistance, ${R_\epsilon}/{R} = \epsilon^{-1}$. With alternatives such as copper tubing, for a single-layer winding at high frequencies, the change in resistance may be estimated by assuming that the skin effect pushes current density fully to the outer surface of the wire. In this case, the resistance is unchanged, i.e. ${R_\epsilon}/{R} = 1$. These represent limiting cases, and the actual exponent of the scaling factor for resistance should fall between 0 and -1.

The power P_ϵ required to maintain the desired AMF amplitude follows directly from the scaling relationships of the resistance and current:

$$\left(\frac{P_\epsilon}{P}\right)_{coreless} = \left(\frac{I_\epsilon}{I}\right)^2 \frac{R_\epsilon}{R} \tag{3.5}$$

Such that

$$\left(\frac{P_\epsilon}{P}\right)_{coreless} \leq \epsilon^2 \tag{3.6}$$

The inductive energy stored in the coil, which scales with volume, therefore increases more rapidly with scale than the dissipated power. This agrees with the commonly held principle that the quality factor of coreless coils increases with size.[84, 86]

Turning to the case of a scaled up electromagnet with a core, Equation 3.1 implies that, similar to the coreless case, the current must increase by the factor ϵ to maintain the AMF amplitude. The power dissipated in the windings would scale according to the preceding

analysis, but it is small compared to the power dissipated in the core. Assuming that the same flux distribution in the core were uniformly scaled upward, dissipated power would scale proportionally with its volume and therefore ϵ^3.

$$\left(\frac{P_\epsilon}{P}\right)_{with\ core} \leq \frac{\epsilon^2 I^2 R + \epsilon^3 P_v V}{I^2 R + P_v V} \qquad 3.7$$

Here, P_v is power dissipated per unit volume in the core material and V is the volume of the core. In Figure 3.7, a plot of estimated power dissipation versus ϵ compares two cases based on values measured for two designs: a gapped 3F3 toroidal electromagnet and a finite solenoid with similar accessible working volume, producing an AMF with an amplitude of 50kA/m at a frequency of 100kHz. The upper bound for the power required by the solenoid accounts for the proximity effect and skin effect expected with a solid copper conductor. The lower bound is based on linear scaling of a measurement of litz wire resistance at 100kHz. For the gapped toroid, power dissipation was estimated by the voltage drop across the shunt resistor R_{shunt}, and the relative contributions of the core and wire were estimated using the current and known resistance of the litz wire alone at 100kHz. As expected, at the scale where the design was implemented, the gapped toroid is more efficient than the solenoid, and its power dissipation is dominated by its core. Figure 3.7(a) suggests that the justification for using a design with a core to reduce required power is rapidly undermined as scale increases. The specific crossover point depends on many factors, including AMF frequency and field amplitude, as well as core geometry and material.

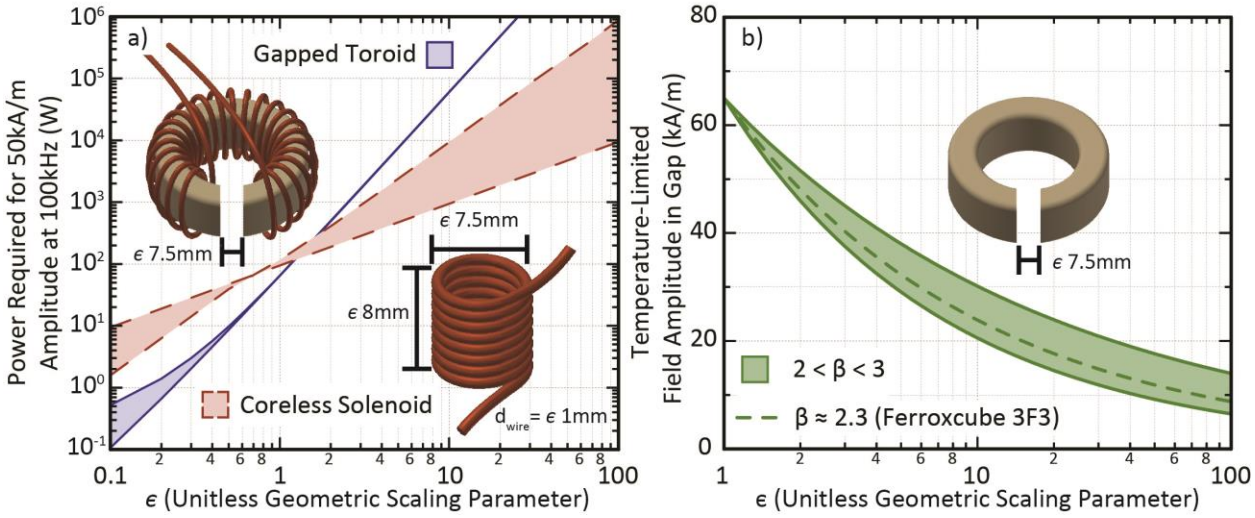

Figure 3.7 (a) Comparison of power requirements for a uniformly scaled gapped toroidal electromagnet and a solenoidal coil, generating the same AMF amplitude at a target point central to the working volume. The analysis is based on applying bounded scaling laws to extrapolate from measured power dissipation and resistances. (b) Estimate of allowable field amplitude in gap for constrained temperature change in the core. The estimate is based on applying a scaling law to a known set of aggressive operating conditions (65kA/m at 100kHz) for a Ferroxcube TX51/32/19-3F3 core with a 7.5mm gap.

Maintaining the same field amplitude in electromagnets utilizing cores is actually far less scalable at high frequencies than an analysis of required power alone suggests. Inductor design favors large sizes for high quality factor, but enlarged designs are limited to lower flux densities due to heating.[86] If the core is constrained to remain below a particular operating temperature, and the rate at which it can transfer heat to its surroundings is proportional to its surface area, then the allowable energy loss density $P_{v,allowed}$ is relatable to ϵ.

$$P_{v,allowed} \propto \frac{\epsilon^2}{\epsilon^3} = \epsilon^{-1} \tag{3.8}$$

Losses in core materials can be modeled as a function of the flux density at a given frequency, according to Seinmetz's equation:[88]

$$P_v \propto {B_{max}}^{\beta} \tag{3.9}$$

P_v is volumetric power dissipation, B_{max} is the peak flux density in the core, and β is a parameter that is approximately 2.3 for 3F3 and 2.2 for N87 according to fits of resistance versus AMF amplitude (Appendix J). This implies that, at sizes sufficient to be limited by temperature increase, the maximum allowable field in the gap scales as $\epsilon^{-1/\beta}$. In consequence of this scaling relationship, illustrated in Figure 3.7(b), larger designs would need to operate at a lower field amplitude, frequency, or duty cycle. Even for particularly well-designed flux paths such as the one presented in Gneveckow et al., the use of a core still limits usable amplitudes.[80] In contrast, cooling copper tubing or litz wire in a coreless coil by flowing deionized water is comparatively feasible, even in cases with many kilowatts of dissipated power. Magnetic materials could still play a role in scaled up designs, where they might be useful as shielding to reduce electromagnetic interference or perhaps even limited volumes could be used to influence the field distribution. However, it is clear that incorporating large volumes of into the main flux path of a large-scale AMF coil is counterproductive.

3.7 Parallel Resonant Tank Circuit Design Principles

For working volumes larger than few cubic centimeters, the previous section argued the advantage of designs that do not make use of soft ferromagnetic flux paths. In the case of coreless coils, it is again desirable to employ some form of resonance, but this time a parallel LC resonant "tank" is more appropriate (Figure 3.8(a)). Placing an inductor and capacitor in parallel amplifies the supplied current by the quality factor, Q, producing potentially large circulating currents. Q-factor is determined by the ratio of resistively dissipated power to stored power.

$$Q = \frac{X_L}{R_T} = \frac{2\pi f_r L_T}{R_T} \tag{3.10}$$

R_T is the resistance of the resonant tank, L_T is its inductance, and f_r is its resonant frequency. For an intuitive understanding of the frequency dependence of the load presented by a resonant tank with a large Q value, the circuit model in Figure 3.8(a) offers a close approximation.[89] R_p is the apparent resistance of the tank at resonance, which depends on Q and L_T.

$$R_p = 2\pi f_r L_T Q = \frac{(2\pi f_r L_T)^2}{R_T} \tag{3.11}$$

Impedance measurements on a resonant tank with various capacitance values are shown in Figure 3.8(b), illustrating how impedance is maximized at resonance and that R_p tends to increase with frequency.

The intent of an AMF coil in the context of biomedical applications of MNPs is to couple an external circuit to magnetic material introduced to the body. The actual power delivered to the MNPs can be a fraction of a milliwatt, far less than the kilowatts required to produce the circulating currents that create an AMF of sufficient amplitude. This implies that the tank can be designed to maximize field amplitude in essentially unloaded operation. Indeed, design characteristics such as the use of parallel conductors intended to maximize the field amplitude produced at resonance by an unloaded tank would not be worthwhile if the design were intended for induction heating.

General characteristics of the tank needed to maximize field amplitude at resonance can be suggested from a few basic circuit considerations that account for constraints on power and voltage. The field amplitude produced by a coil with N turns can be estimated by

$$H_0 \approx \alpha I_0 N \tag{3.12}$$

Here, α is a proportionality factor determined by the coil geometry. The approximation is warranted for a tightly confined current distribution, such as in a low aspect ratio solenoid. For a long solenoid, the dependence on N is weaker because adding turns to the ends has a diminishing

influence on the field at the center. Assuming that each turn contributes a resistance R_{turn} to the coil, the maximum power that can be delivered to the coil P_{max} limits the maximum value of the field,

$$H_{max} \leq \left(\alpha \sqrt{\frac{P_{max}}{R_{turn}}} \right) N^{0.5} \tag{3.13}$$

In the idealized resonant tank of Figure 3.8(a), the maximum circulating current is limited by the inductive reactance of the coil X_L in combination with the maximum voltage that can be applied to the tank V_{max}. This maximum voltage limit is a design parameter set by the capacitor array of the tank or perhaps ultimately by safety and dielectric breakdown considerations, especially given the possible path to ground via the circulating cooling fluid. Consistent with the approximation made in Equation 3.12, let $X_L \approx 2\pi f_r A_L N^2$, where A_L is a geometry dependent inductance factor and f_r is the resonant frequency.

$$I_0 \leq \frac{V_{max}}{X_L} = \frac{V_{max}}{2\pi f_r A_L N^2} \tag{3.14}$$

$$H_{max} \leq \left(\frac{\alpha V_{max}}{2\pi f_r A_L} \right) N^{-1} \tag{3.15}$$

Taken together, Equations 3.13 and 3.15 illustrate a fundamental tension in designing tank circuits that maximize field amplitude. Increasing N to reduce the required power eventually increases the inductance enough that the field amplitude may instead become limited by the voltage that can be applied to the tank. Regardless of the particular geometry or exact

dependence on N, a design maximizing the field amplitude in the working volume operates where the power and voltage limits coincide.

Figure 3.8(c) illustrates this principle with generality for three cases defined in terms of the ratio of the prefactors in Equations 3.13 and 3.15. By attempting to reach higher field amplitudes in scaled up high frequency coils (increased A_L), increasing P_{max}, and decreasing R_{turn}, the optimal number of turns is pushed progressively lower and the maximum grows progressively sharper, indicating the advantage of geometries with a few turns that carry high currents. High Q-factor is desirable so that power can be delivered efficiently and the majority of resistive losses occur in the tank. This, however, must be achieved by decreasing tank resistance rather than by increasing tank inductance. Decreasing R_{turn} can be accomplished by the use of parallel conductors and actively cooled litz wire. Figure 3.8(d) shows how these strategies increase the Q-factor for several coils with comparable inductance and similar resonance frequency, pictured in Figure 3.8(e).

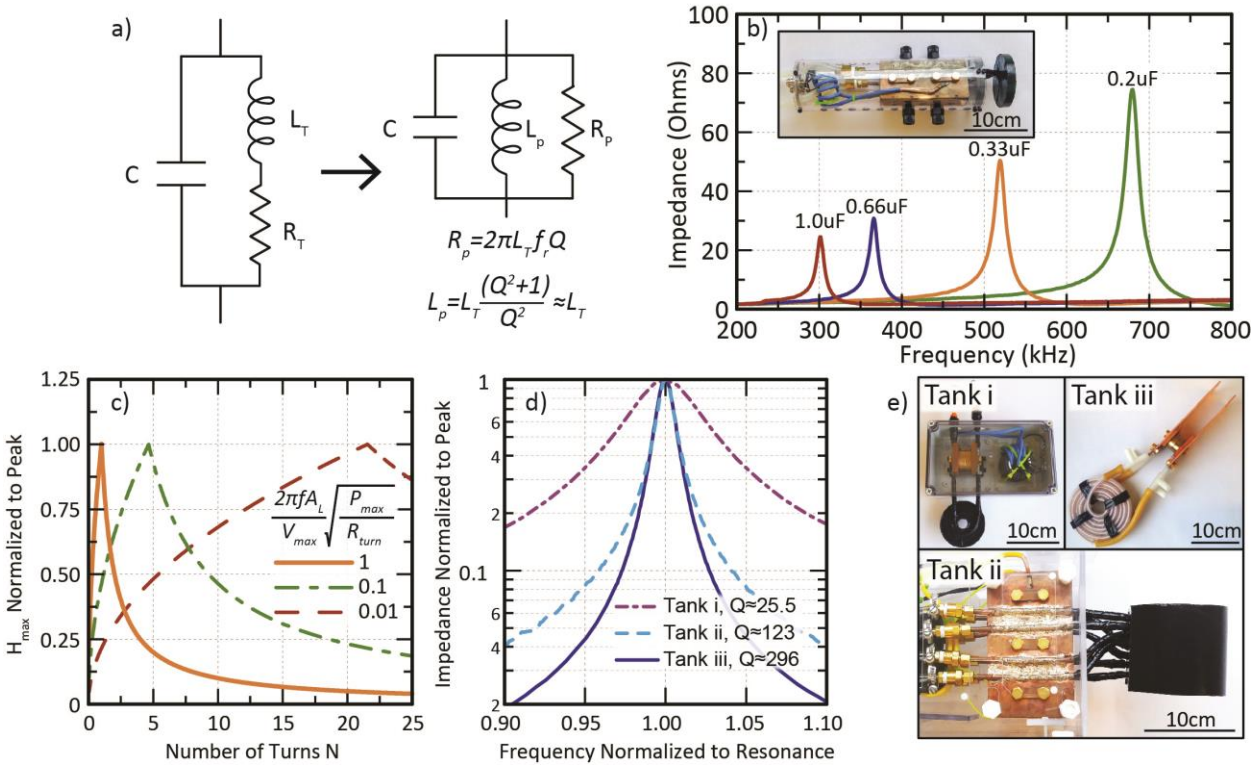

Figure 3.8 (a) Basic electrical schematic of resonant tank for establishing large circulating currents and an intuitive model with nearly identical impedance vs frequency characteristics. (b) Impedance vs frequency for a handheld coil with various resonances. (c) Analysis of the role of voltage and power constraints on optimizing the number of turns in an idealized tank circuit. (d) Measured Q-factor values of resonant tanks with comparable inductance and resonance frequencies but different inductor design. (e) Photographs of the coils measured in (d). Tank i is a simple 8 turn copper tubing coil. Tank ii incorporates 4 parallel copper tube conductors into an 8cm diameter two turn solenoid. Tank iii incorporates two parallel litz wires (42x10x10/44 AWG) surrounded by flexible Teflon tubing for flow.

The functionality of a resonant tank design employing a copper coil with two turns of four parallel conducing copper tubes was assessed by measuring the AMF amplitude with an inductive probe consisting of three orthogonal pickup loops. Figure 3.9(a) shows a finite element magnetostatic simulation for a current of 1.7kA in such a coil, assumed to be distributed evenly over the parallel conductors. A comparison with measurements along the center axis of a coil driven at approximately 164kHz suggests that the finite element model provides a reasonable

description of the expected profile and that very high circulating currents are being generated. (Figure 3.9(b)). Photographs of two resonant tanks, complete with transformers, high power capacitors, copper bus bars, and coils potted by epoxy for user protection are shown in Figure 3.9(c)-(d). The high circulating current in the tank necessitates active cooling by rapidly flowed deionized water passing through the custom made heat exchanger shown in Figure 3.9(e).

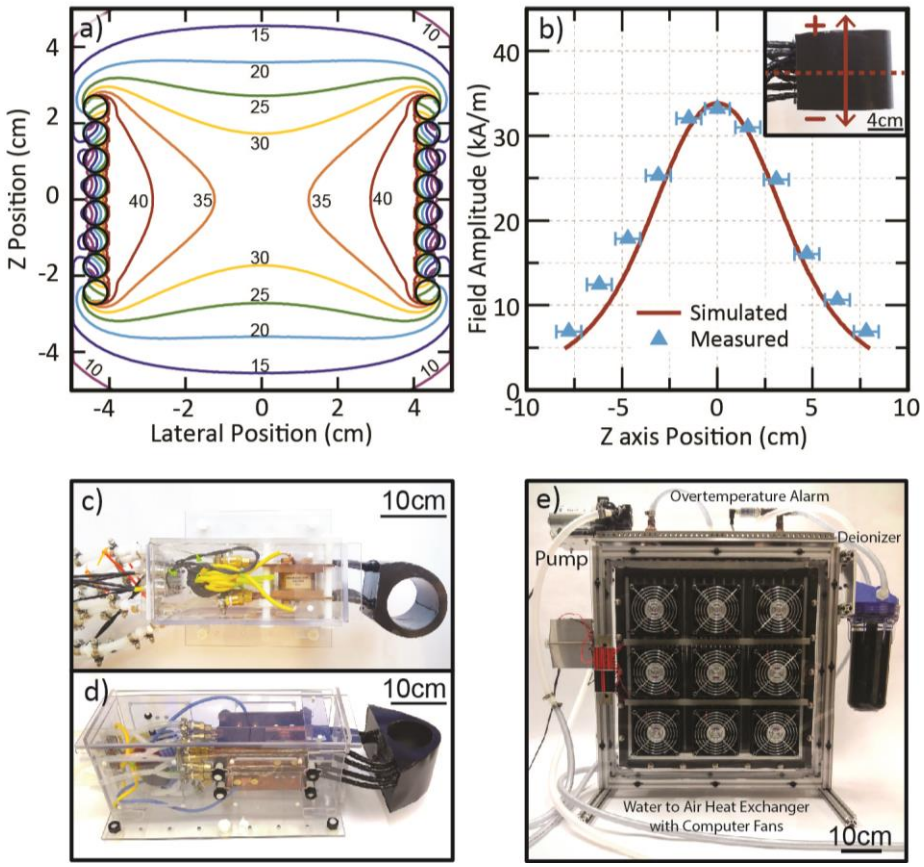

Figure 3.9 (a) Cross sectional view of finite element model plot for a two turn coil with four parallel conductors carrying a combined 1.7kA. (b) Field amplitude at 164kHz as measured by 3 interpenetrating orthogonal inductive pickup loops along the z axis of the coil, as compared to the values predicted in (a). (c) Resonant tank for ~160kHz operation. Insulating black potting epoxy covers the turns of copper tubing. (d) Resonant tank for ~720kHz operation. Note two series layers of capacitors in the array to increase voltage tolerance. (e) Heat exchanger for cooling resonant tanks with rapidly flowed deionized water.

3.8 Inverter Design

The use of an amplifier to drive the series resonant circuits described in Section 3.4 was a convenient and robust choice partly because the commercial linear amplifier used is extensively engineered to protect itself against failure from mismatched loads. Unfortunately, the cost of linear amplifiers climbs steeply with increasing power output capability, and power required for a resonant tank circuit like those shown in Figure 3.9 to reach a desired AMF amplitude is orders of magnitude higher than the power required by the electromagnets discussed in Section 3.3 to reach the same amplitude. This necessitated the design of a system capable of delivering at least several kilowatts of power to a resonant tank at a frequency that could be easily adjusted for use with different resonant tanks.

The first design iteration toward this goal in this thesis work was the development of a prototype half bridge inverter, shown schematically in Figure 3.10(a). Rather than making use of a commercial DC power supply, this design made direct use of AC line power from the wall, regulating it with a variable transformer, and stepping up the AC voltage before rectifying it with a full wave voltage doubler. A square wave at the desired frequency was delivered by a function generator to a circuit that incorporated a typical positive edge delay of about 50ns and a negative edge delay of about 5ns before feeding the signal to a digital isolator bridge driver chip (Analog Devices ADuM4223). These isolator chips then drove a pair of MOSFETs to switch between the high end of the DC power and ground, producing a square wave at the frequency set by the function generator. A DC blocking capacitor causes this square wave to be centered at 0V (Figure 3.10(b)), acting as a suitable power source for the resonant tank. The maximum recommended operating frequency is set by the isolated bridge driver chips at 1MHz, although the current handling capability of the MOSFETs decreases with frequency as switching losses

increase. The intent of the delay is to prevent common conduction of the MOSFETs, which would lead to failure in this configuration. Although it was able to deliver as much as a kilowatt of power at 130kHz, it became clear that the reliability and functionality of this prototype could be improved by adopting printed circuit board layout practices that reduced inductive noise on the gate drive and using a full bridge rather than half bridge topology. (The full bridge topology results in a higher square wave voltage, which is desirable considering the voltage limits on circulating current discussed in Section 3.7.)

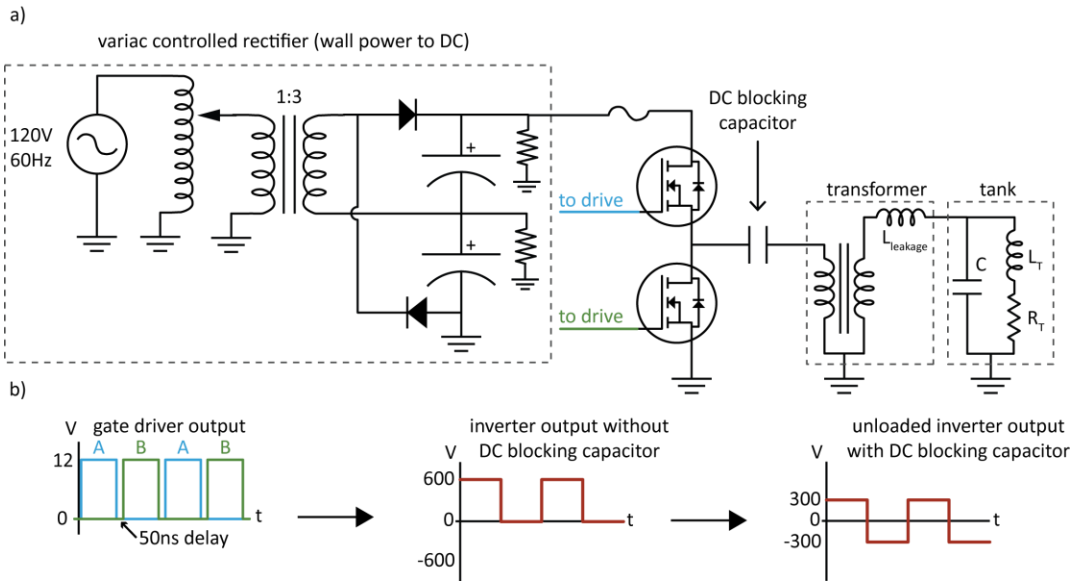

Figure 3.10 (a) Schematic of the half bridge inverter prototype. 120V 60Hz power from a wall outlet is stepped up adjustably by a variable transformer in series with a fixed transformer. The power is fed to a full wave voltage doubler that rectifies the power with a low ripple voltage. This DC voltage is converted to square wave by the half bridge and fed through a DC blocking capacitor and transformer to the resonant tank. (b) Various idealized voltage signals are shown, including the drive signal for the MOSFETs, inverter output without DC blocking, and inverter output with the DC blocking capacitor.

After several iterations of design and revision, an effective full bridge inverter system was developed. Its simplified conceptual schematic is depicted in Figure 3.11(a) and the custom inverter fed by parallel, computer controlled DC supplies is shown in Figure 3.11(b). The

internal layout of the inverter is shown in Figure 3.11(c). Notably, the design uses silicon carbide MOSFETs suitable for switching small currents at high voltages and frequencies, placing them close to one another and to bypass capacitors to avoid inductive coupling to the drive circuitry. Multiple full bridge boards triggered with the same input signal can be used in parallel to handle high currents.

The voltage and current combination demanded by R_P for maximal power delivery typically differs from what is supplied by the full bridge, suggesting the need for a transformer to maximize performance. For a transformer core, a stack of power ferrite toroids can be used to handle the increased power. In contrast to the transformer used in the series resonant circuits, leakage inductance in this context plays a crucial functional role by rejecting higher frequency components of the square wave (Figure 3.11(d)-(e)). Without the leakage inductance of the transformer, high frequency components of the square wave can shoot-through the tank, potentially causing the MOSFETs within the full bridge driver to fail. Partially coupled to the capacitance in the tank, the leakage inductance acts analogously to an L matching network, slightly shifting resonance and stepping up the voltage applied to the tank. Accounting for this is necessary to avoid exceeding the voltage tolerance of the resonant tank. The operating frequency of a resonant tank, identified by the phase of the impedance, must be measured with the transformer in place. More sophisticated driving circuits could potentially adjust frequency by sensing the load, but the methods described here have proven sufficient for functionality. Driving the resonant tank far from resonance, or otherwise driving a strongly inductive or capacitive load is not advisable and can result in catastrophic failure of the MOSFETs.

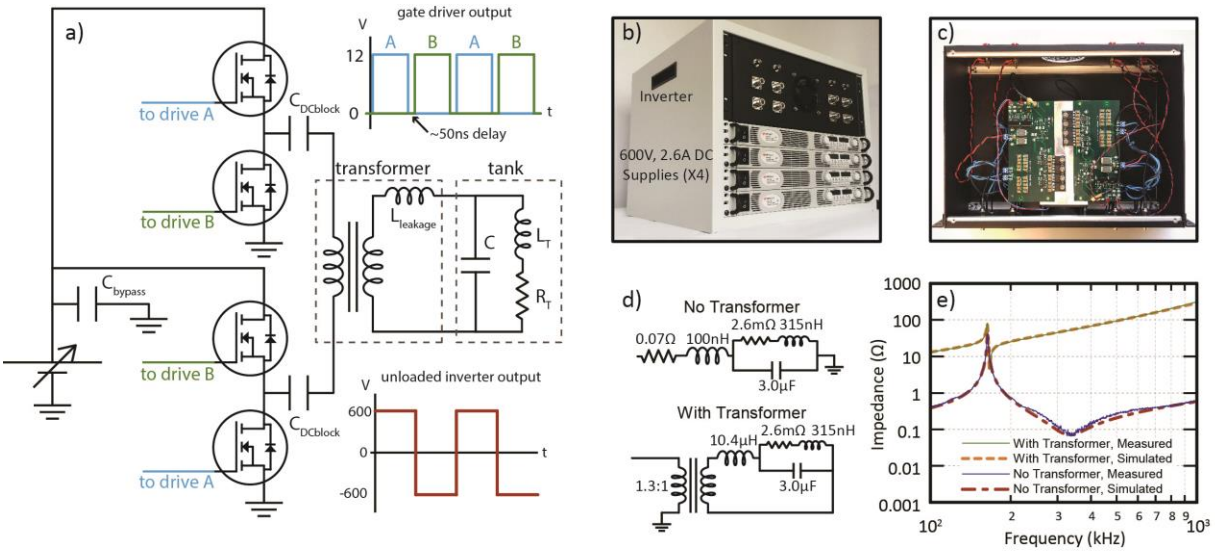

Figure 3.11 (a) Schematic overview of full bridge inverter design (b) Photograph of the inverter and high voltage DC power supplies. (c) Photograph of the internal components of the inverter. (d) Models of a resonant tank without a transformer and with a transformer incorporating leakage inductance. The former model includes resistance and inductance of test leads. (e) Measurements of low voltage impedance versus frequency for a resonant tank with and without a transformer, as compared to the predictions of the models in (d).

3.9 Outlook for Clinical Scalability

Research on biomedical applications of MNPs acted upon by AMFs implicitly assumes that particular AMF conditions employed experimentally can be feasibly scaled to the human body. Although an example of a clinical scale coil does exist,[80] studies are conducted over a wide range of AMF conditions, often with a markedly higher $H_0 f$ product than the AMF produced by this particular instrument. It is worthwhile to consider the problem in a more general way by extending the reasoning behind the resonant tanks demonstrated in the previous section to coils suitable for reaching a target deep inside a human brain.

Recalling the conclusion of the earlier thought experiment of coil scalability (Figure 3.7), a useful geometric starting point for designing a suitable tank is a (purely hypothetical) superconducting circular loop with a diameter of 35cm (Figure 3.12(a)) that can accommodate a

head with ample room left for insulation. Consistent with the analysis in Figure 3.8(c), the large voltages already necessitated by the inductance of this single loop recommend against a design with multiple turns (Figure 3.12(b)). Taking the target point to be the center of the loop, a bound on the minimum current needed to produce an amplitude meeting the $H_0 f$ product limit can be calculated, since distributing current density by adding additional parallel conductors will only increase the total required current. In envisioning how to replace this loop with real wire, e.g. water-cooled litz wire, it is neither practical to restrict the required current to a single conductor, nor to attempt to distribute it over thousands of parallel conductors cocooning the working volume. The latter strategy would, in principle, minimize the necessary power, but it does so at the expense of dramatically increasing the total required current, which causes the capacitor array to grow formidably in size and expense. A rational compromise is to set a target value for power to be dissipated per wire. The heat exchanger in Figure 3.9(e) was able to compensate for about 1kW of power dissipated per conductor, so this quantity can serve as a conservative limit for the purpose of discussion. Using measurements of the linear resistance of the litz wire incorporated into the coil in Figure 3.12(c) and the physical dimensions of the loop, the maximum current per wire can be estimated, which suggests the necessary number of conductors.

To determine an efficient geometric distribution of these parallel conductors one can assume that together they form a N by M rectangular cluster of wires, with spacing that accounts for the outer diameter of the surrounding cooling tube (Figure 3.12(a)). Then the total resistance of the coil and the total field produced at its center may be found by a sum or superposition of constituent rings, respectively. Figure 3.12(d)-(f) illustrate how total dissipated power varies with M and N for a fixed total number of conductors. At low frequencies (e.g. 50kHz) where large

currents are required, the necessary power is >150kW (Figure 3.12(f)), a level that far exceeds that of the higher frequency alternatives. In cases where total required power is comparable for two possibilities, higher N improves field uniformity (Figure 3.12(e),(h)). A finite element magnetoquasistatic model for this distribution of current predicts the variation of the field as shown in Figure 3.12(g)-(i), and additionally offers a means to calculate inductance using the magnetic field energy. The capacitor array must withstand both the total resonance current and the voltage applied to produce it. Such an array would consist of up to several hundred parallel and series elements that require cooling and account for a significant portion of the cost of such a system (Figure 3.12).

This analysis has several limitations. Notably, the current was assumed to be uniformly distributed over the parallel conductors. A more detailed design might balance the inductance and resistance of the conductors simply by constraining them to the same length and distributing their connections to the capacitor array in a way that mitigated differences in contributions to inductance. Also, the power dissipation of the capacitor array was neglected, such that required power would certainly exceed the values in Figure 3.12(d)-(f), though the array would operate at a lower current density than the coil. Crossover of the wires as they connect to the capacitor array (Figure 3.12(b)) would add some resistance, but the field would drop off more quickly far from the resonant tank, a feature that could help reduce its inductance.

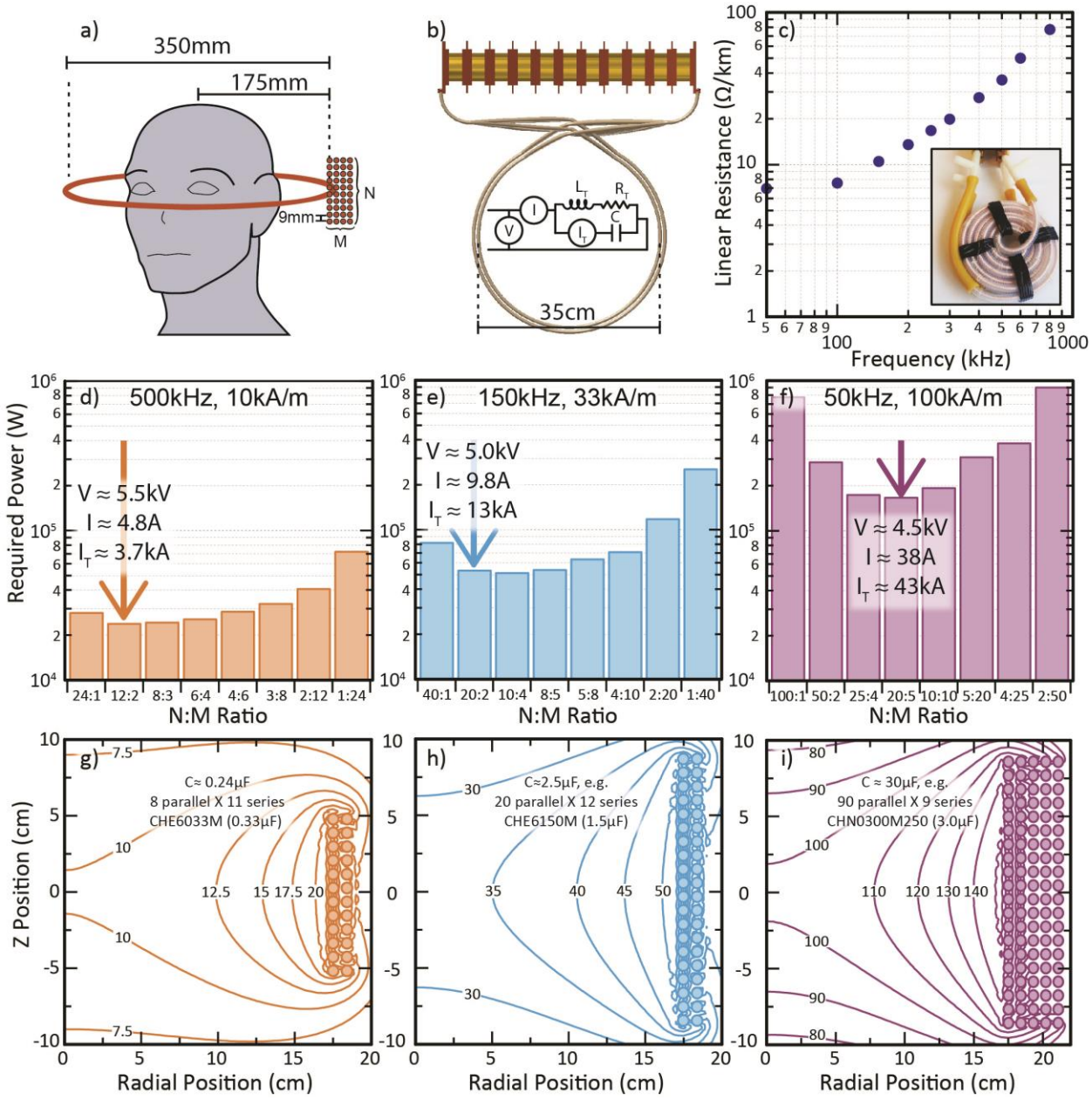

Figure 3.12 (a) Geometric starting point for a scaled up design for applying AMFs to a human head. (b) Sketch of top view of a scaled up resonant tank, along with definitions of quantities appearing elsewhere in the figure. (c) Measured linear resistance versus frequency for 42x10x10/44 AWG litz wire surrounded by Teflon tubing for flow. (d)-(f) Power dissipation required to achieve stated target field amplitude and frequency in the center a coil with a fixed number of parallel litz wire conductors arranged in various rectangular bundles. (g)-(i) Cylindrical magnetostatic finite element models of magnetic field magnitude for the recommended configurations. Possible capacitor array designs are indicated to corroborate feasibility.

4 Chapter 4. Empirical Identification of Materials Suited to Magnetothermal Multiplexing

4.1 Considerations Informing Material Selection

As was indicated in Section 2.8, multiplexing requires designing MNPs with differing coercivity, not tuning σ values for different frequencies.[‡‡] This chapter focuses on a route for identifying such materials via experimental characterization. The focus is on making a robust selection of two magnetic materials suitable for multiplexing, though such techniques can be readily extended to additional modes.

A reasonable starting point in a search for multiplexing materials is to assume that one of the modes will be based on iron oxide MNPs that have already been demonstrated to heat sufficiently for multiple applications.[90] This raises the question of whether MNPs with greater or lesser coercivity will prove to be more readily feasible for the second mode. MNPs with lower coercivity would favor use at higher frequencies and lower AMF amplitudes, which in principle reduces the required power and complexity of the setup producing the AMF at clinical scales, as suggested by Section 3.9. For the purpose of a demonstration that can be restricted to small working volumes in which high field amplitudes are more readily achievable, several other pragmatic considerations favor the design of a second type of MNPs with greater coercivity.

If it is supposed, as in Figure 4.1, that despite having different coercivity, two types of MNP are designed to have similar σ values for multiplexing, then lowering the coercivity has predictable effects on the energy scale of magnetic dipole interactions between MNPs, expressible as a ratio:

[‡‡] Recall from Section 2.4, Equation 2.13, that σ is a measure of the anisotropy energy barrier of a particle normalized to the ambient thermal energy. It was assumed to be proportional to the volume of an MNP.

$$\frac{U'}{U} = \left(\frac{H_k}{H'_k}\right)^2 \qquad 4.1$$

Here, U and U' are the initial and modified energy of the magnetic dipole-dipole interactions, respectively, and H_k and H'_k are the initial and modified anisotropy fields, respectively. The relationship implies that seeking a material with a lesser coercivity while maintaining a σ value in the ferromagnetic regime necessarily increases interparticle interactions. (See Appendix K for a more thorough explanation of the reasoning behind Equation 4.1.) These interactions can lead to clustering, aggregation, and settling. Increased energies of interaction are also likely to influence the dynamic magnetization response and hysteresis behavior of MNP suspensions at high concentration.[72] The design goals of colloidal stability and intrinsic multiplexing behavior clearly suggest the need for materials with higher H_k.

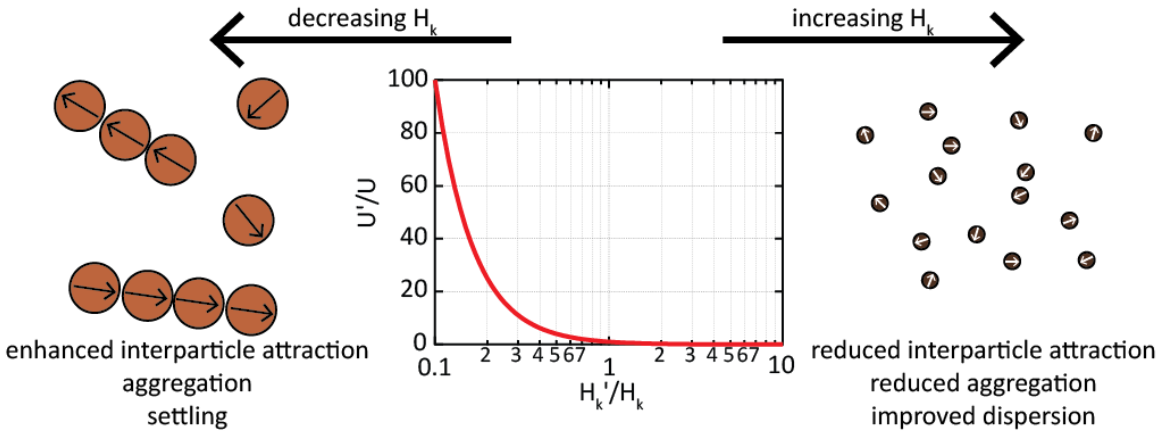

Figure 4.1 For multiplexing, dynamic hysteresis suggests the need for MNPs in the ferromagnetic regime with similar $\boldsymbol{\sigma}$ values, but differing coercivity. The expected interaction energy of MNPs with the same $\boldsymbol{\sigma}$, but different anisotropy fields $\boldsymbol{H_k}$, varies in a predictable way according to Equation 4.1. Reducing $\boldsymbol{H_k}$ leads to stronger interparticle interactions, whereas increasing $\boldsymbol{H_k}$ reduces interparticle interactions.

An additional argument can also be made for the pragmatism of seeking higher coercivity MNPs rather than lower coercivity MNPs for multiplexing. Although the definition of H_k may appear indifferent to whether M_s or K_{eff} are varied, the upper theoretical limit on SLPs is proportional to K_{eff} and does not depend on M_s (Appendix E). This suggests that for high SLPs, it is better to increase K_{eff} than to decrease M_s. For ferrites incorporating other transition metal ions (e.g. $M_xFe_{3-x}O_4$), magnetocrystalline anisotropy varies by at least an order of magnitude, whereas M_s stays within a factor of two.[54] Clearly, manipulating K_{eff} is the most relevant handle for designing multiplexing systems. As discussed in Appendix B, K_{eff} can arise from many separate influences, including spin orbital interaction within the crystal, shape anisotropy, and surface effects. In such a situation, it is generally more realistic to expect to feasibly increase one of these contributions appreciably, rather than to reduce all of them simultaneously. Again an approach with higher coercivity is indicated.

With both the theoretical motivation of Chapter 2 and the reasoning presented in this section, there is sufficient information to undertake an empirical search for multiplexing materials. This chapter will elaborate on the experimental methods necessary to do this. A reader familiar with the techniques described in subsequent sections may wish to skip to Section 4.7, which describes how such data can be analyzed to predict suitability for multiplexing.

4.2 Vibrating Sample Magnetometry

Vibrating sample magnetometry (VSM) is one of several techniques for measuring the magnetization of a sample in response to an applied static magnetic field. Typically, a large electromagnet with a soft ferromagnetic yoke applies a magnetic field in an adjustable gap about 1-2cm in width. The magnitude of the applied field can range from a fraction of a militesla up to 1T or higher. A quartz rod suspends the sample from an actuator that vibrates at some known

frequency, e.g. 20Hz. Contained within the faces of the gap of the electromagnet are a probe to sense the magnitude of the applied field, and also several thousand turns of fine magnet wire acting as inductive pickup coils. As the sample vibrates, its magnetic moment creates a time varying magnetic flux in the pickup loops, inducing a measureable voltage. By first measuring a nickel standard with a magnetic moment of known magnitude, the voltage signals measured from unknown samples can normalized to quantify their magnetic moments. Such a system, if optimized and operated appropriately can measure moments as low as $10^{-9}\mathrm{JT}^{-1}$ (10^{-6} emu).

Measurements of moment versus applied magnetic field can provide a variety of useful information about samples, best illustrated by several specific examples:

1. **Saturation Magnetization**

   If a sample exhibits simple saturation behavior, then the estimated value of the saturation moment can be measured as the asymptotic value approached by the moment at the highest field magnitudes. The MNPs in this thesis almost always exhibit simple saturation and apparent deviation from this behavior at high fields can usually be explained by improper background subtraction such as the use of a background reference sample with a different volume of water than the actual sample. The saturation moment can be used to deduce saturation magnetization if concentration of MNPs is known, or conversely can be used to estimate concentration if the saturation magnetization of that batch has previously been measured. If concentration is established by an analytical technique that destructively measures metal ion content, it is common practice to define magnetization using this quantity to avoid making assumptions about the phase or oxygen stoichiometry of the sample.

2. **Estimating Magnetic Moments of Individual MNPs**

When measuring dilute, monodisperse MNPs, it is sometimes possible to estimate the magnitude of individual particle moments from VSM measurements without needing to know concentration or saturation magnetization. If saturation is observed, the curve measuring the sample moment m can be renormalized to the saturation moment m_s. Since the moment of the sample is saturated when the magnetization is saturated,

$$\frac{m}{m_s} = \frac{M}{M_s} \tag{4.2}$$

Here, M is magnetization, and M_s is saturation magnetization. The Langevin function is a result of classical statistical mechanics that describes equilibrium magnetization of moments in an applied field that are able to assume arbitrary orientations and do not exhibit anisotropy.[54] In general, the Langevin function should not be expected to provide a good fit of the M/M_s versus H curves for real MNPs since the theory behind it does not account for magnetic anisotropy or interparticle interactions. However, in the limit $H \to 0$, the expected susceptibility converges to that of the Langevin function for randomly oriented MNPs, even if they exhibit significant anisotropy.[68] Consequently, the magnitude of their moments m_{MNP} can be estimated by the following equation

$$m_{MNP} = \frac{3k_B T}{\mu_0}\left(\frac{dM/M_s}{dH}\right)_{H\to 0} \tag{4.3}$$

A more detailed discussion of the reasoning behind this relationship and circumstances of its applicability can be found in Appendix L. Larger magnetic moments result in higher

susceptibility in the limit of low applied field magnitude, an inference anticipated by Equation 4.3 and demonstrated experimentally in Figure 4.2.

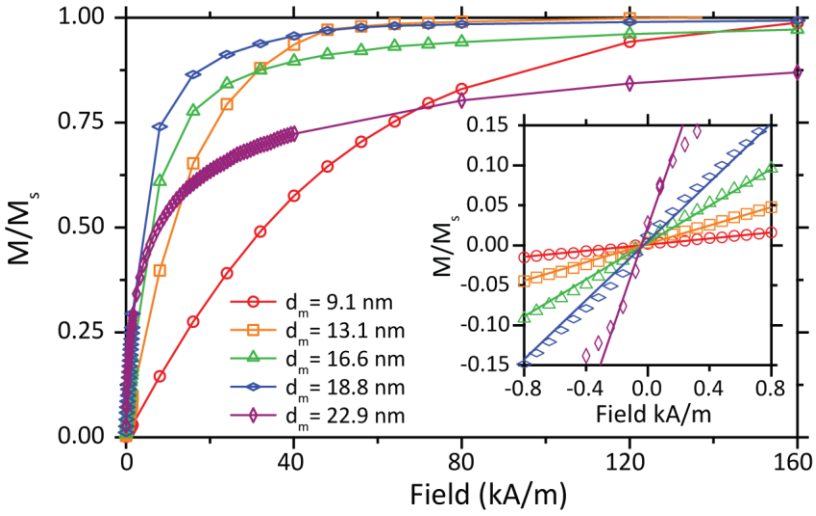

Figure 4.2 Vibrating sample magnetometry measurements were made on MNPs samples with differing physical diameters, as described in Chen et al.[91] A linear fit was performed in the limit of low field to determine "magnetic diameter," as described in detail in Appendix L, with larger moments resulting in steeper slopes. Taken from Christiansen et al.[51]

In cases where a comparison to bulk material is warranted, the concept of "magnetic diameter" d_m can provide a readily interpretable proxy for magnetic moment. This quantity can be defined as the diameter of a uniformly magnetized sphere with the same magnetic moment indicated in Equation 4.3, assuming the bulk magnetization value. This implicitly provides a form of comparison between bulk and sample magnetization values, such that the magnetic diameter is not expected to exceed the physical diameter of spherical MNPs. Expressing the concept mathematically,

$$d_m = \left(\frac{6\,m}{\pi M_{s,bulk}}\right)^{\frac{1}{3}} \qquad 4.4$$

Aside from useful comparison of nanoscale properties to bulk properties, estimating the magnitude of the magnetic moments of a sample of MNPs as suggested offers a

nondestructive method to measure ξ for real samples, which is useful if attempting to map the results of characterization onto a model as directly as possible.

3. Assessing Interparticle Interactions

The previous two uses of VSM data were routinely employed for material characterization during the course of work presented in this thesis. One less frequent use that nevertheless warrants consideration is the use of M/M_s vs H curves to assess interparticle interactions. When these curves do not exhibit hysteresis, they can be interpreted as reaching equilibrium at each point and sometimes they contain clues that hint at the influence of dipole-dipole interactions between MNPs.

Consider an illustrative example. Iron oxide MNPs nominally 25nm in diameter were purchased from Ocean Nanotech, LLC and encapsulated in liposomes as part of the controlled release mechanism employed by the experimental study described in Section 6.3. Compared to MNPs dispersed in solution, encapsulation in liposomes creates an environment of high local concentration where interaction effects are likely to be more pronounced. VSM measurements were performed on two highly dilute samples from the same batch of MNPs, only one of which was encapsulated in liposomes. The curves, normalized to their apparent saturation values, are shown in Figure 4.3. Note that the susceptibility in the limit of low applied field magnitude is not significantly different in the two cases, although the approach to saturation is more gradual for the MNPs encapsulated in liposomes. Similar behavior would be expected from two sets of randomly oriented MNPs with identical moments, but differing anisotropy.[68] Given that the MNPs are from the same batch and encapsulation would not be expected to modify the properties of individual MNPs, this effect is presumably attributable to dipole-dipole interactions. Related experiments can be imagined, for instance

comparing aggregated MNPs to well dispersed ones, in which *M* versus *H* curves offer evidence for interaction.

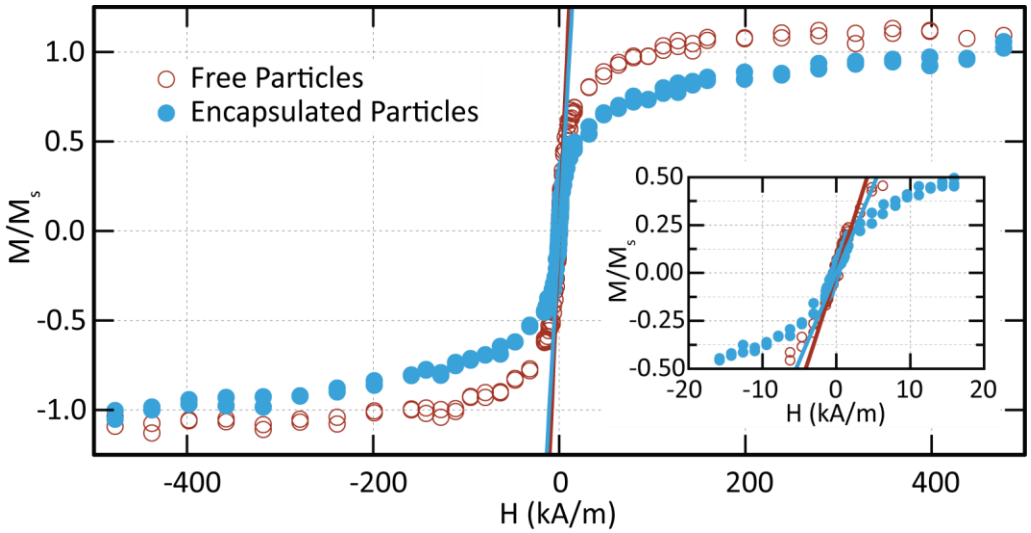

Figure 4.3 Iron oxide MNPs supplied by Ocean Nanotech LLC with a nominal 25nm diameter were suspended in 100μL of water measured by vibrating sample magnetometry. Using samples prepared from the same MNPs, one contained encapsulated the MNPs in liposomes, while the other contained freely dispersed MNPs. Linear fits of low field susceptibility (zoom shown inset) are indicated by solid lines and did not suggest a significant difference as would be expected for different moments. This, combined with the slower approach to saturation in the case of encapsulated MNPs, may suggest an effective anisotropy resulting from interparticle interactions. (Compare to Figure 2b of Carrey et al.[68]) Data taken from the supplementary materials of Schürle et al.[92]

4.3 Inductively Coupled Plasma Atomic Emission Spectroscopy

Inductively coupled plasma atomic emission spectroscopy (ICP-AES) is an analytical technique for determining the identity and concentration of ions dissolved in dilute nitric acid. The method is sufficiently sensitive to allow detection of trace amounts of heavy metals in food, drink, or environmental samples in parts per billion.[93] It is useful to employ such a technique because measurements of saturation magnetization (Section 4.2) and specific loss powers (Section 4.4) are, at best, only as accurate as the measured concentration of the samples.

Preparing MNPs such as the ones described in this thesis for ICP-AES involves dissolving them in a small volume of concentrated hydrochloric acid, resulting in a bright yellow (iron) or green (cobalt) solution. This solution is then diluted by nitric acid to its final volume. An automated peristaltic pump feeds this solution to a nebulizer, which creates a fine mist that is sprayed into an argon plasma flame. Here, transitions between excited electronic states of the atoms present in the solution result in spectra with emission peaks at known wavelengths. A high resolution diffraction grating enables spectral analysis of the light produced by the flame, nominally ranging from 167nm to 785nm, but attention typically focuses on ultraviolet peaks for greatest precision. (See the manual for the Agilent 5100.) In cases where elemental content is unknown, the evidence for the presence of elements can be deduced from set of spectral peaks that are observed.

In the context of the work performed here, the elements are typically known and measuring concentration is the primary concern. Concentration values are determined by comparing the relative intensity of peaks to a series of standard solutions of varying dilutions of known concentration. This series of samples together establish a calibration curve, and the accuracy of the results is limited by the quality of the calibration curve.

4.4 AMF Calorimetry in Samples Suspended in Water

As was discussed in Section 1.5, one key figure of merit for assessing and comparing the power dissipation capabilities of MNPs in an AMF is specific loss power (SLP). Observing trends in SLP as a function of H_0 has also played a central role throughout this work in testing hypotheses related to the models for hysteresis discussed in Chapter 2. Efforts to perform calorimetric measurements began with a focus on measuring the SLPs of MNPs suspended in water, which is the situation most frequently relevant to biomedical applications of these

materials. Ideal calorimetry in this case consists of placing a sample of a known concentration in adiabatic conditions and measuring its rate of change in temperature under continuous exposure to an AMF of known amplitude and frequency.

$$SLP = \frac{m_{sample}}{m_{Fe}} C_s \left(\frac{dT}{dt}\right) \approx \frac{C_w}{\varphi} \left(\frac{dT}{dt}\right) \quad 4.5$$

Here, m_{sample} is the sample mass, m_{Fe} is the mass of iron (or more generally total metal ions) in solution as determined by ICP-AES, C_s is the specific heat of the sample and $^{dT}/_{dt}$ is the rate of change in temperature. This expression can be approximated in terms of the specific heat of water C_w (≈4.184 J g^{-1} K^{-1}) and the concentration φ in g mL^{-1}, provided that the following approximations are valid:

1. The density of water at room temperature can be regarded as sufficiently close to exactly 1 g mL^{-1} that any variation from this figure can be neglected.
2. The concentration of magnetic nanoparticles is sufficiently low that $C_s \approx C_w$. In practice, most of the calorimetry performed in this work involved samples with a few parts per thousand iron by mass.
3. The specific heat of water is sufficiently independent of temperature to approximate it as a constant.

Equation 4.5 seems simple, but accurately measuring SLP in customized AMF setups requires careful mitigation of a variety of sources of error; the literature is replete with questionable measurements. Thermal management strategies should be adopted to best approach the adiabatic conditions that are assumed for Equation 4.5. This can include adequate insulation of the sample, reduction of waste heat from the setup providing the AMF, and measurement only over short

durations where the deviation of sample temperature from the holder temperature is small. Careful background subtraction, performed by measuring the apparent heating rate of water samples, should be done frequently and carefully. When a large set of samples is being measured, it is advisable to establish a timed cycle of operation for the AMF setup, with the intent that it will reach some steady state temperature versus time profile that allows for direct comparison against the control samples.

To measure and record temperature, an optical fiber probe was used rather than a thermocouple or thermistor. Any metal objects, including most wires, should be expected to heat due to eddy currents in the presence of a strong AMF, and in this case such heating would artificially inflate the apparent heating rates of the MNPs in the absence of proper controls. Unfortunately, the particular temperature probe used in the characterization efforts described here (Omega Engineering HHTFO-101) exhibits small jump discontinuities every few degrees Celsius, perhaps due to rounding in an internal lookup table (Figure 4.4(a)). Because temperature versus time was measured for long times and relatively small temperature deviations, it was necessary develop correction factors to account for the effect of these discontinuities, as described in Appendix M.

An extrinsic influence that is not widely appreciated is the role of anisotropy resulting from the shape of the sample itself. It has been experimentally demonstrated that changing the aspect ratio and concentration of samples comprised of the same MNPs can markedly influence heat dissipation.[94] In order to avoid this effect, the characterization efforts represented here made use of cylindrical vials in which the direction of the field was perpendicular to the axis of the cylinder. Even before this geometry was adopted, the vials were filled to a level that ensured an aspect ratio of approximately unity and relatively low concentrations were used. Shape

anisotropy resulting from the sample itself should be proportional to the magnetization squared, so reducing concentration in principle also significantly reduces the effect. It is notable that the favorability of low concentration is indicated both by the need for relatively small temperature changes to approach adiabatic conditions and also for mitigating the role of sample shape anisotropy. On the other hand, sufficient concentration is required to produce a heating rate observable compared to background noise. Most measurements described in this thesis were conducted on samples with concentrations of approximately 2mg mL^{-1}.

The development of setups to measure heat dissipated by MNPs was an iterative process, starting with a prototype limited to low AMF amplitudes ($\leq 5kA/m$) that emphasized thermal management strategies. It consisted of a litz wire solenoid placed in a thin plastic tube affixed to the bottom of a bucket, which could be filled with equilibrated ice water (Figure 4.4(b)). The space between the sample and the coil was carefully thermally insulated, but alumina based thermal grease was placed between the solenoid and the wall of the tube. Preceding operation, the coil was run continuously and the level of the ice water was adjusted until the temperature of a control sample matched room temperature. In this manner, minute differences in heating rates were reproducibly measurable. Aside from its limitation to field amplitudes at or below about 5kA/m, the direction of the field applied to the effectively cylindrical sample is parallel with the axis, which is not ideal for mitigating the influence of sample shape anisotropy.

The design of subsequent setups was motivated primarily by the need to reach higher AMF amplitudes for relevant comparison to existing literature. This was accomplished by shrinking the volume of the sample from 1mL to 100μL and adopting coils with gapped soft ferromagnetic flux paths, designs that produce high AMF amplitudes with relatively small input powers, as explained in Section 3.2. Sample holders were assembled from layers of plastic and

insulating polystyrene foam cut with a laser cutter and the electromagnet was cooled with water circulated from an ice bath (Figure 4.4(c)).

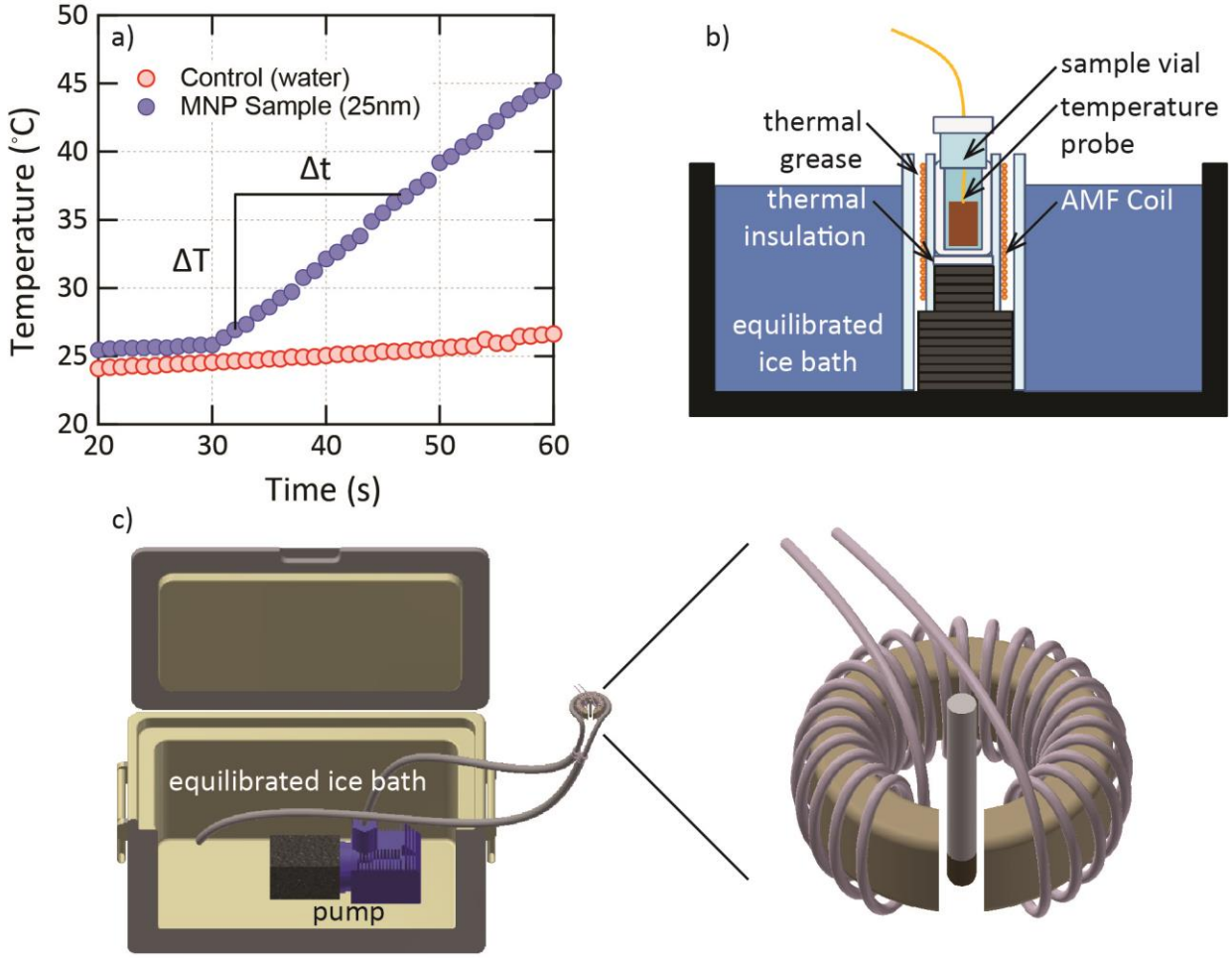

Figure 4.4 (a) A representative plot of temperature versus time for an Ocean Nanotech iron oxide MNP sample nominal average diameter of 25nm and a water sample serving as a background control are shown under exposure to an AMF with $\boldsymbol{H_0 = 25 kA/m}$ at $\boldsymbol{f = 500 kHz}$ starting at $\boldsymbol{t = 30 s}$. (Adapted from supplementary of Romero et al. [95]) (b) A sketch of a prototype AMF calorimetry system built early in this thesis work is shown. (c) In an updated calorimetry setup, an aquarium pump in a cooler is used to circulate water from an equilibrated ice bath to an electromagnet to offset waste heat from the core.

4.5 AMF Calorimetry in Solid Systems

Occasionally it is necessary to characterize the heating rates of MNPs embedded in solid matrices, whether for the purpose of developing an application such as the one discussed in Section 5.3 or for the sake of studying a physical system in which physical rotation should not

occur. The previous section explained that there are three necessary input quantities to determine SLP: 1) specific heat of the sample, 2) concentration of magnetic material, and 3) rate of temperature change under exposure to an AMF in approximately adiabatic conditions. AMF calorimetry in solid systems warrants a separate discussion because all three of these quantities are determined in a manner different from the liquid suspension.

The specific heat of water has been thoroughly characterized and studied and is relatively constant with respect to temperature, but the same is not necessarily true for polymer or resin matrices in which MNPs are embedded. Several straightforward techniques exist to measure specific heat. In this case, differential scanning calorimetry was used to compare polymer composite samples to a sapphire reference sample. (Details of this technique and the reasoning behind it can be found in Appendix M).

In liquid samples, concentration could be measured directly by dissolving the sample after measurement for analysis by ICP-AES. In the case of solid samples, this would require burning away the polymer that forms the majority of the sample mass, dissolving all the MNPs, and filtering out bits of ash that could clog the nebulizer. A more advisable approach consists in measuring the saturation magnetization of a batch of nanoparticles using VSM and ICP-AES, and then nondestructively measure the saturation moment of the polymer samples with VSM to deduce content of metal ions as suggested in Section 4.2. This, along with a measurement of the mass of the sample, provides concentration by weight.

The temperature probe used for liquid samples needs to be immersed in order to produce accurate measurements, and this kind of intimate interfacial contact is not possible for solid samples. Instead, an IR thermographic camera was used (FLIR ThermaCam S60) to record changes in temperature of the sample during exposure to an AMF. Figure 4.5 sketches the typical

setup for this purpose, which includes a custom polystyrene holder to insulate and contain samples cured in the shape of circular discs, with approximately 1.5mm thickness and 4mm diameter.

No matter how carefully the above steps are conducted, instrumental uncertainty of calorimetry measurements on solid samples is likely to be larger than for samples suspended in water. This is because the methods recommended for estimating concentration and measuring specific heat inevitably introduce uncertainty that was largely avoided in the techniques described in Section 4.4. One of the advantages of normalizing SLP curves to a projected maximum value for some particular sample, is that using a ratio that allows these constants to cancel reduces uncertainty.

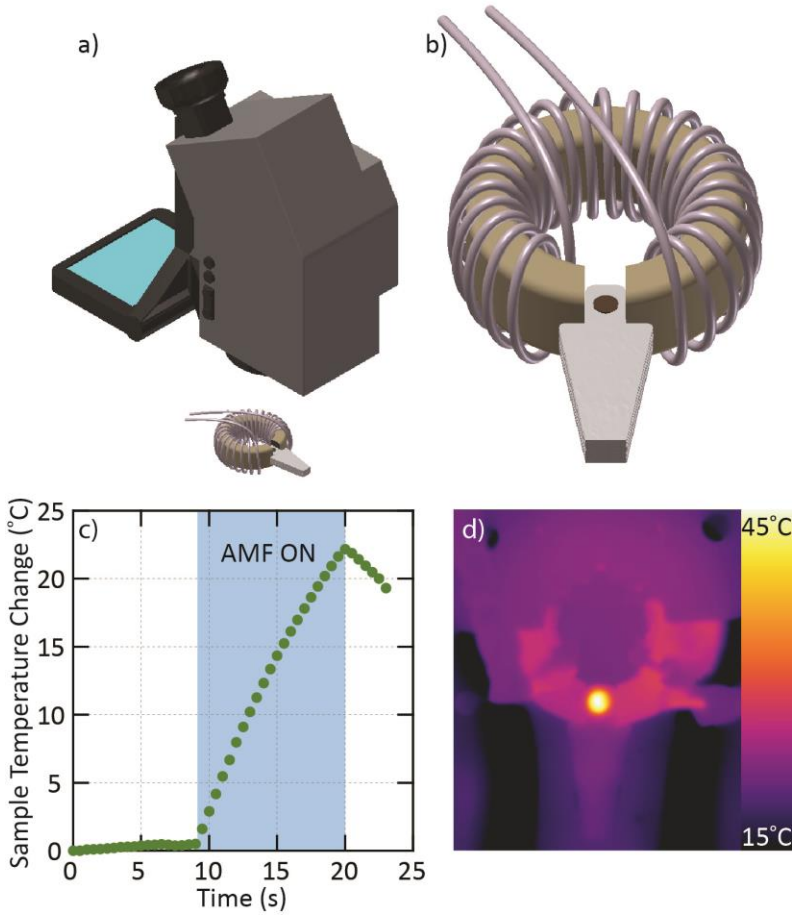

Figure 4.5 (a) A sketch shows the relative position of the IR camera, electromagnet, and sample holder. (b) A detail of the sample holder, containing a brown polymer composite disc, is shown with the sample placed in the gap of the electromagnet. (c) A representative plot of temperature versus time for a sample exposed to $H_0 = 60kA/m$ at $f = 100$kHz is shown. (d) An IR thermograph captures the time point with highest sample temperature difference from the trial shown in (c). The view is a top-down perspective of the same layout as in (b).

4.6 AC Magnetometry

Measuring the heating rates of MNPs exposed to AMFs is a conceptually straightforward method of characterization, often with direct relevance to their intended use. However, recalling the argument of Section 2.1 that heat dissipation can be understood in terms of hysteresis, even hypothetically perfect calorimetry can at best quantify the area of these loops. Alternative methods exist to measure loss characteristics in magnetic systems, and one such technique called AC magnetometry is capable of capturing M vs H curves at high frequencies and AMF

amplitudes. This is preferable not only for the additional information gained by observing the shape of hysteresis loops, but also in reducing the role of extrinsic thermal influences and potentially offering a route for high throughput loss power versus amplitude data collection.

AC magnetometry has a long history and has been employed by researchers to measure MNP systems intended for cancer hyperthermia.[75, 76, 94] The typical design, sketched in Figure 4.6(a), consists of a long solenoid that applies a uniform AMF to a pair of smaller, more densely wound solenoidal pickup coils. The latter are wound in opposite directions, placed in series, and positioned at either end inside the large solenoid. One of these pickup coils contains the sample, which contributes to the induced voltage with its time-changing magnetization. The second of these two series pickup coils is sufficiently far from the sample that the voltage induced in it can be reasonably regarded as entirely resulting from the AMF. Because they are wound in opposite directions, the second coil compensates for the voltage induced in the sample coil by the driving AMF. If the field profile and the windings are perfectly geometrically symmetric, in principle only the signal from the sample should remain. In practice, this cancellation is almost always incomplete, but the background is reduced to a level where simple subtraction readily reveals the signal from the sample. In setups where high driving AMFs are achievable, it has been shown repeatedly that square-like hysteresis loops are observed,[75, 76] evidence that contradicts the predictions of linear response theory as applied in these conditions in a way that is more consistent with the general character of the models explored in Sections 2.4 through 2.6.

An AC magnetometer setup was constructed during the course of this thesis work in an effort to provide an additional line of evidence for evaluating a preliminary multiplexing demonstration. It was designed to measure over a wide frequency range at AMF amplitudes limited to a few kA/m. 3D-printed polymer coil forms were created to maximize geometric

symmetry in both the driving coil and the pickup coils, which were wound with fine litz wire. Self-resonance of the pickup coils limited their maximum usable frequency. The parasitic capacitance responsible for this effect likely resulted from a combination of electric fields between fine multilayer windings and the capacitance of the coaxial cables connecting them to the oscilloscope measuring induced voltage signals. Fewer turns are needed to produce a robust signal from the pickup coils at high frequencies, so this issue was overcome by creating a series of three magnetometers spanning the desired frequency range with sufficient overlap to ensure continuity. Data from this effort is shown in Figure 4.6. Notably, it shows a crossover point in imaginary susceptibility for the two samples at low field amplitudes that is consistent with the calorimetry data (Figure 2.9) and with the assertion in that paper that the 25nm MNPs were in the ferromagnetic regime.

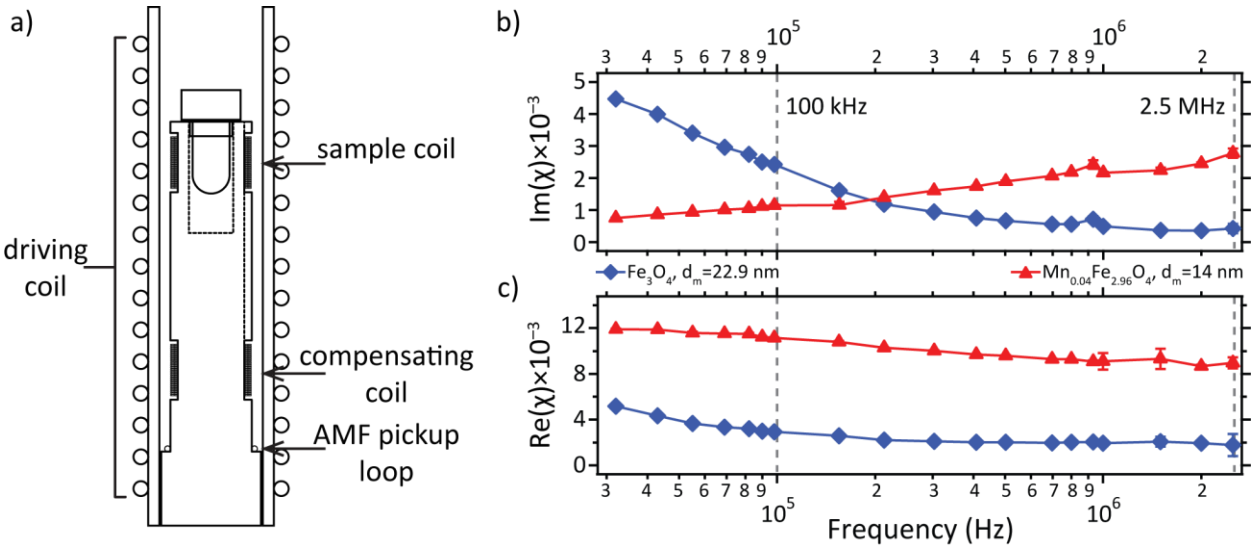

Figure 4.6 (a) A sketch of the AC magnetometer constructed for measuring susceptibility at low field amplitudes ($\leq$ **3kA/m**), following the typical design. The sample coil and compensating coil, which are as geometrically symmetric as possible, are placed in series but wound in opposite directions. This causes the voltage signal induced in each by the AMF generated by the driving coil to cancel, leaving only the induced voltage signal from the changing magnetization of the sample. A pickup loop is used to measure the AMF amplitude. All coil forms were 3D printed in ABS plastic. Data from the setup, measuring the real (b) and imaginary (c) parts of the susceptibility χ of the multiplexing samples depicted in Figure 2.9. The observed crossover in $\mathbf{Im}(\chi)$ is consistent with the calorimetry findings. Adapted from Christiansen et al.[51]

4.7 Heuristic Route to Multiplexing Based on Characterization Data

Perhaps the most pragmatic approach for identifying materials suitable for multiplexing is to heuristically extrapolate heating rates from characterization data, making projected comparisons at numerous conditions. Studying the models of hysteresis in Chapter 2 was valuable primarily because it motivated the feasibility of multiplexing and suggested how suitable MNPs might be designed (Section 4.1). However, all models make simplifying assumptions, and even the most general models explored in Chapter 2 are no exception. Moreover, input quantities for these systems such as K_{eff} are difficult to predict or measure and could plausibly vary significantly throughout a population of MNPs (Appendix B). Attempting to incorporate these kinds of considerations into a model results in rapidly diminishing marginal utility; a small gain in understanding is made at the expense of considerable additional

complexity. By comparison, extrapolation of experimental data is a simple approach adequate for making suitable selections for magnetothermal multiplexing from a set of MNPs and AMF conditions presently available.

Experimental data suggests that reasonably accurate extrapolation is possible within the frequency range of interest. For a given sample of MNPs, the specific loss energy (SLE) per cycle of the AMF, defined by dividing the SLP by the frequency, appears to remain relatively consistent in both solid and liquid matrices (Figure 4.7(a)-(b)). Both dynamic hysteresis and linear response theory anticipate only small changes in SLE per cycle for MNPs in the ferromagnetic regime over the frequency range of interest, so this behavior is not unexpected. In order to test the hypothesis that this method can be used to extrapolate heating rates, Figure 4.7(c)-(d) show an extrapolation of the data in Figure 4.7(b) at amplitudes meeting the $H_0 f$ product limit at various frequencies, and Figure 4.7(d) compares these predictions against calorimetry measurements. This method of extrapolation appears to be adequate for the purpose of heuristically identifying of materials and AMF conditions suitable for magnetothermal multiplexing, demonstrated in Section 5.4 for bulk heating.

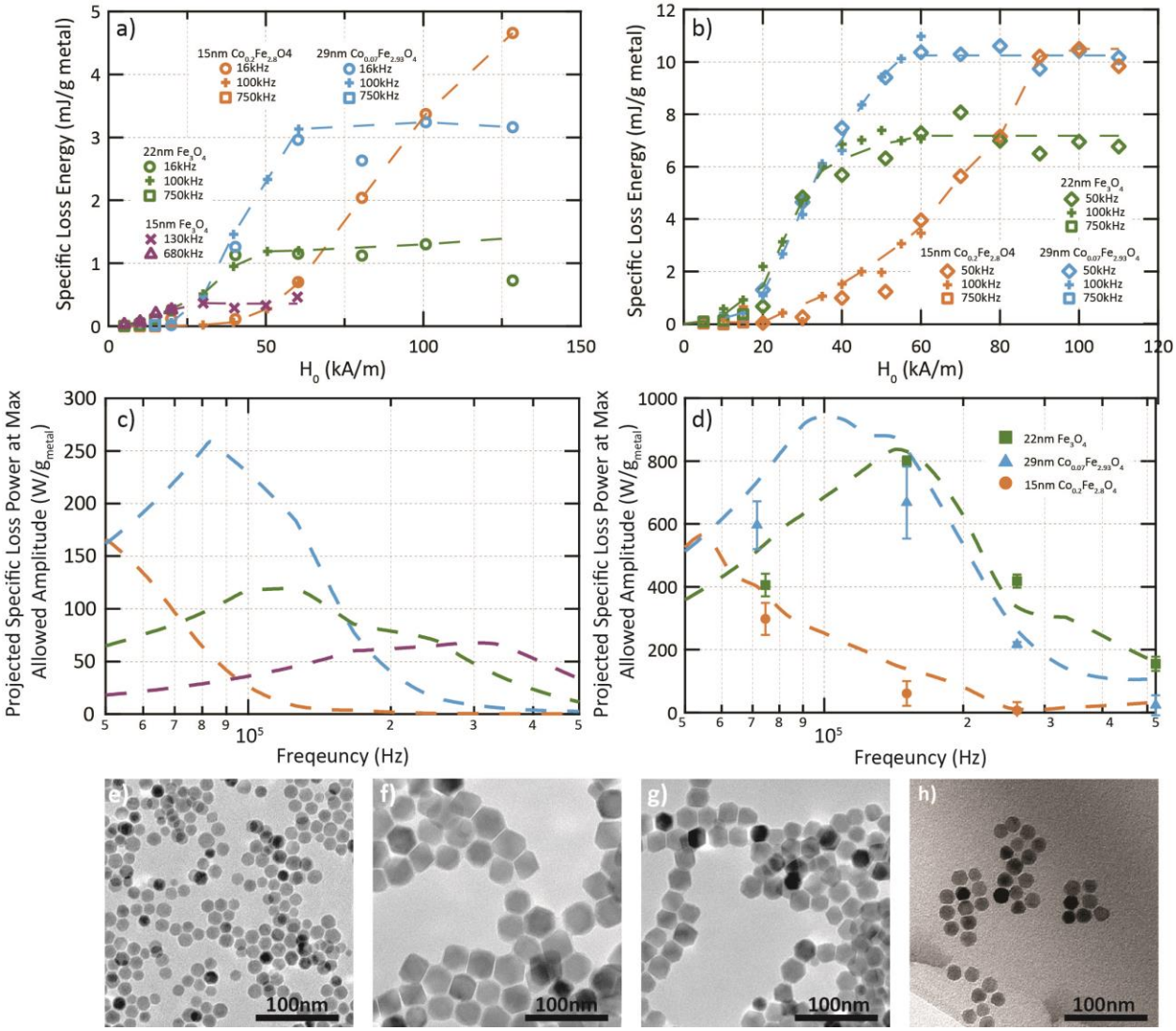

Figure 4.7 Specific loss energy per cycle of the AMF (calculated by dividing SLP by frequency) versus field amplitude $\boldsymbol{H_0}$ is shown for samples prepared in polymer composite discs in (a) and suspended in water in (b). (c) and (d) show projections for specific loss power at the maximum allowed AMF amplitude as a function of frequency, based on the heuristic method described in the text for samples in solid matrices and suspended in water, respectively. (d) Includes points measured to test validity of the heuristic projections. (e)-(h) Transmission electron micrographs of the samples measured in (a) and (b). (e) shows 15.1±2.0nm MNPs with 6.5±1.1% Co ($Co_{0.2}Fe_{2.8}O_4$). (f) shows 29.1±2.7nm MNPs with 2.4±0.2% Co ($Co_{0.07}Fe_{2.93}O_4$). (g) shows 21.9±1.9nm Fe_3O_4 MNPs and (h) shows ~15nm Fe_3O_4 MNPs.

5 Applications Based on Bulk Heating of MNPs

5.1 The Case for Methods Based on Bulk Heating

The term "bulk heating" here refers to the heating that results from the exposure of a region with a significant volume fraction of MNPs to an AMF. Viewing MNPs as infinitesimal point sources of heat distributed homogeneously throughout a volume, it is reasonable to adopt a continuum approximation for heat dissipation. This is in contrast to nanoscale heating effects, which are applicable to the case of isolated MNPs, a topic discussed in greater depth in Chapter 6. One straightforward consequence of the continuum approximation is that heating rates can increase with concentration, though the relationship is not necessarily linear and there are practical limits on how concentrated suspensions can be. Namely, at high concentrations, the formation of large aggregates limits injectability and interparticle interactions are expected to influence the heating properties of the MNPs.[72]

Cancer hyperthermia, probably the longest researched application of MNPs for biomedical applications, relies inherently upon bulk heating to elevate the temperature within tumors and cause cancer cell death.[21] In the work presented in this thesis, bulk heating is employed in the context of two possible applications: magnetothermal stimulation of neurons with ferrofluid droplets[20] and the actuation of shape memory polymer composites via dissipated heat.[47]

5.2 Neuronal Stimulation with Ferrofluid Droplets

The basic scheme for neuronal stimulation via bulk heating that was experimentally investigated during this thesis work is represented in Figure 5.1(a). The concept involves injecting a highly concentrated droplet of MNPs into the brain in order to produce a rapid rise in local temperature upon exposure to an AMF. Prior transfection of the surrounding cells causes them to overexpress TRPV1, a heat sensitive channel protein that undergoes a conformational

change at temperatures above 43˚C, permitting diffusion of divalent ions such as Ca^{2+}.[35] Neurons actively maintain electrochemical gradients and contain voltage gated ion channels in order to propagate actions potentials, and these endogenous features help to amplify the effect produced by opening TRPV1.

Experiments to examine this approach were first conducted *in vitro*, where a series of stimulation trials with primary hippocampal cultures transfected to express the calcium indicator GCaMP6s that were placed in ferrofluid. Changes in GCaMP6s fluorescence, as measured by an inverted fluorescence microscope, were taken to be indicative of intracellular calcium concentrations correlated with activity.[96] By comparing the responsiveness to AMF stimulus of neurons both expressing TRPV1 and bathed in ferrofluid to suitable controls that excluded these factors, it was strongly indicated that both were necessary for stimulation, a finding consistent with the hypothesized mechanism described above (Figure 5.1(b)-(c)).

A similar experiment was performed *in vivo* to assess stimulation provided by a droplet of ferrofluid to the ventral tegmental area of sedated and restrained mice. In this case, a different indicator of neural activity was chosen: postmortem histological staining for c-fos, an immediate-early gene expressed in correlation with recent neuronal activity.[97, 98] A set of trials with these animals analogous to the *in vitro* experiment described above similarly suggested a significant increase in neuronal activity for animals exposed to AMF stimulation if they were both transfected to overexpress TRPV1 and injected with a droplet of ferrofluid (Figure 5.2(a)).

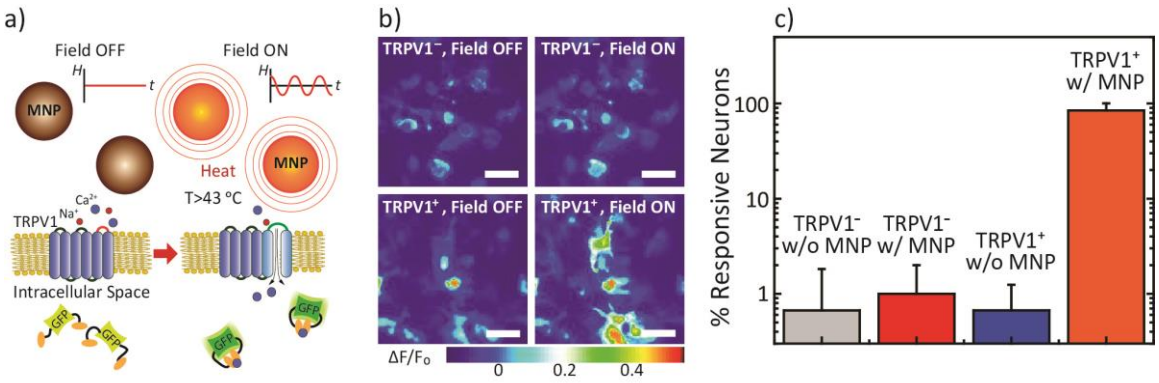

Figure 5.1 (a) A conceptual depiction of neural stimulation via the heating of concentrated ferrofluid droplets. MNPs dissipate heat in the presence of an AMF, triggering the opening of TRPV1. Ca^{2+} influx is observed via a fluorescence increase in GCaMP6s. (b) False color images of GCaMP6s fluorescence intensity in primary rat hippocampal cultures bathed in ferrofluid. An increase in fluorescence indicates an increase in intracellular Ca^{2+} under exposure to an AMF as compared to a control lacking TRPV1 overexpression. (c) A population study of 100 neurons shows the percentage of responsive neurons under AMF stimulation, comparing the responsiveness of cultures with TRPV1 expression and MNPs against control trials that remove one or both of these factors.

The promise of this approach for deep brain stimulation is best understood within the context of other methods that use AMFs for noninvasive stimulation. Perhaps the best established of these is "transcranial magnetic stimulation," which uses a rapidly pulsed current to generate a magnetic field that elicits action potentials through faradic induction.[§§] This technique has been approved by the federal Food and Drug Administration for clinical use on patients with depression and other ailments, and research into other applications is ongoing.[13] Some of the relevant field coil designs use superposition to produce focal points for stimulation, but spatial specificity is limited.[99]

[§§] The circuits that generate these fields typically discharge a capacitor into an inductive field coil, which can produce an alternating magnetic field that decays rapidly. The highest dB/dt, and therefore the peak in induced voltages at the targeted site, comes from the rapid initial rise.

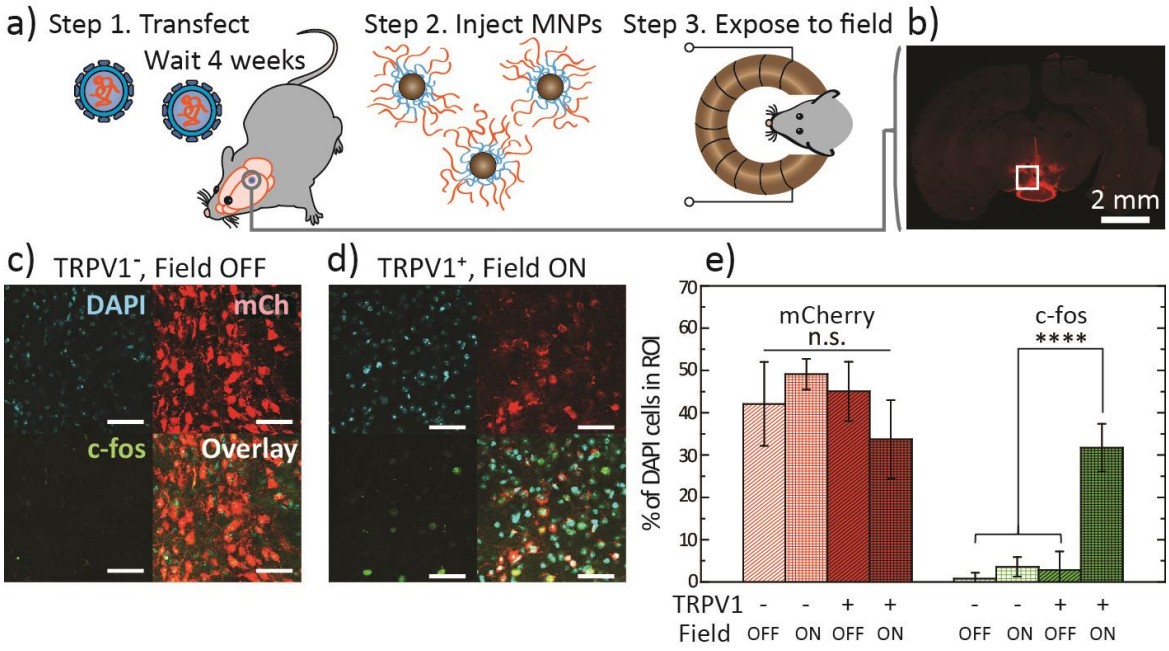

Figure 5.2 (a) An outline is shown for an *in vivo* ferrofluid stimulation experiment. Mice are transfected by direction injection, 4 weeks are allowed for expression, the mice are injected with a concentrated droplet of MNPs in the same region, and they are exposed to an AMF. (b) mCherry, a red fluorescent protein (co-expressed with TRPV1 in trials overexpressing TRPV1), is used to verify transfection of the targeted brain structure, the ventral tegmental area. (c) Confocal microscopy shows DAPI (blue), mCherry (red) and c-fos (green) staining for the ventral tegmental area of a mouse expressing TRPV1, but not exposed to AMF. DAPI stains all cells, mCherry indicates extent of viral transfection, and c-fos is correlated with activity before the animal is killed. (d) The same is shown for a mouse expressing TRPV1 and exposed to an AMF. (e) c-fos and mCherry expression are shown as the proportion of cells revealed by DAPI staining for micrographs such those in (c) and (d), as well as the two other control groups indicated. n = 4 for each group of mice.

A magnetothermal method demonstrated by Huang et al. made prior use of transgenic overexpression of TRPV1 combined with nanoscale heating effects in low concentrations of MNPs.[12] Like the bulk heating approach, this method should provide greater selectivity than transcranial magnetic stimulation, both spatially and possibly by cell type through chemical targeting or selective transfection. The drawback of using low concentrations of MNPs that bind to the membranes of cells for local nanoscale heating is that they are unlikely to persist there for long durations. A process such as cellular uptake of MNPs bound to the membrane would limit their usable lifetime after injection to perhaps a matter of days, depending on the aspects of their

surface chemistry.[100] Some researchers claim to have avoided the use of magnetic nanomaterials and instead purport to use a fully transgenic biomagnetic mechanism.[11, 15] For instance, Stanley et al. describe the expression of ferritin attached to channel proteins that enables response to magnetic fields, including alternating magnetic fields.[19] These fully transgenic approaches have come under scrutiny because the mechanisms they claim are unclear or implausible.[39, 40]

While perhaps less elegant, using the bulk heating of a droplet of ferrofluid offers a mechanism that is comparatively simple, robust, and plausible. Additionally, histological staining of the tissue surrounding droplets of ferrofluid with PEGylated surface chemistry implanted in mice suggests that a reduced immune response is elicited compared to implants.[20] This is consistent with prior literature suggesting that better matching mechanical properties of brain tissue such as modulus and mass density can contribute to improved biocompatibility.[101, 102] Ferrofluid droplets are known to remain for months in the brains of glioblastoma patients participating in clinical trials for cancer hyperthermia,[103] and such persistence ostensibly could enable stimulation over long timeframes if a similar injection were used for neuronal stimulation.

While bulk heating clearly presents advantages over closely related technologies, it should be noted that any approach that requires transfection faces significant hurdles to clinical relevance. An additional objection could be raised regarding the long term impact of repeatedly heating the healthy tissue surround the injection site of the ferrofluid and the limitations on duration or repetition that could result. Chen et al. address the survivability of surrounding tissue in their supplementary material,[20] but even a high expected survival fraction can eventually result in significant damage with excessive repetition.[104] Other unintended consequences might result from repetitive heating such as reorganization of local neural networks or changes in the behavior of glia.

5.3 3D Printed Shape Memory Polymer Composites

Some polymers are known to undergo a shape memory response that can be activated by heat.[105] The basis of this effect is a second order phase transition between glassy and rubbery states, which allows a sample to be heated until it transitions to its rubbery state, mechanically manipulated into some desired shape, and quenched back into its glassy state to freeze it in place.[106] Upon heating to restore it to the rubbery state, the sample elastically returns its original shape. A composite consisting of such a polymer system embedded with MNPs can be heated with an AMF in order to actuate the shape memory response, an idea previously studied in several different polymer systems.[47, 107] In principle, medical devices such as stents or drug release devices incorporating such a composite material with a transition temperature slightly above body temperature could undergo a predetermined mechanical response upon actuation by an AMF.

Previous work on shape memory composites incorporating MNPs is has typically been limited to curing samples in planar geometries. An active collaboration between the MIT Bioelectronics Group and the lab of Prof. Qi Ge of Singapore Institute of Technology and Design is exploring the possibility of incorporating MNPs into intricate structures produced through an additive manufacturing technique in which the monomer precursor is selectively photo polymerized one layer at a time to form three dimensional shapes such as the one shown in Figure 5.3. The monomer solution consists of benzyl methacrylate (BMA) as a linear chain builder, and the crosslinkers poly (ethylene glycol) dimethacrylate (PEGDMA), bisphenol A ethoxylate dimethacrylate (BPA), and di(ethylene glycol) dimethacrylate (DEGDMA).[108] This effort combines the additive manufacturing expertise of the Singapore lab with magnetic

materials and AMF setups produced at MIT. The collaboration could offer progress toward the manufacture of objects with shapes relevant to functionality in medical devices.

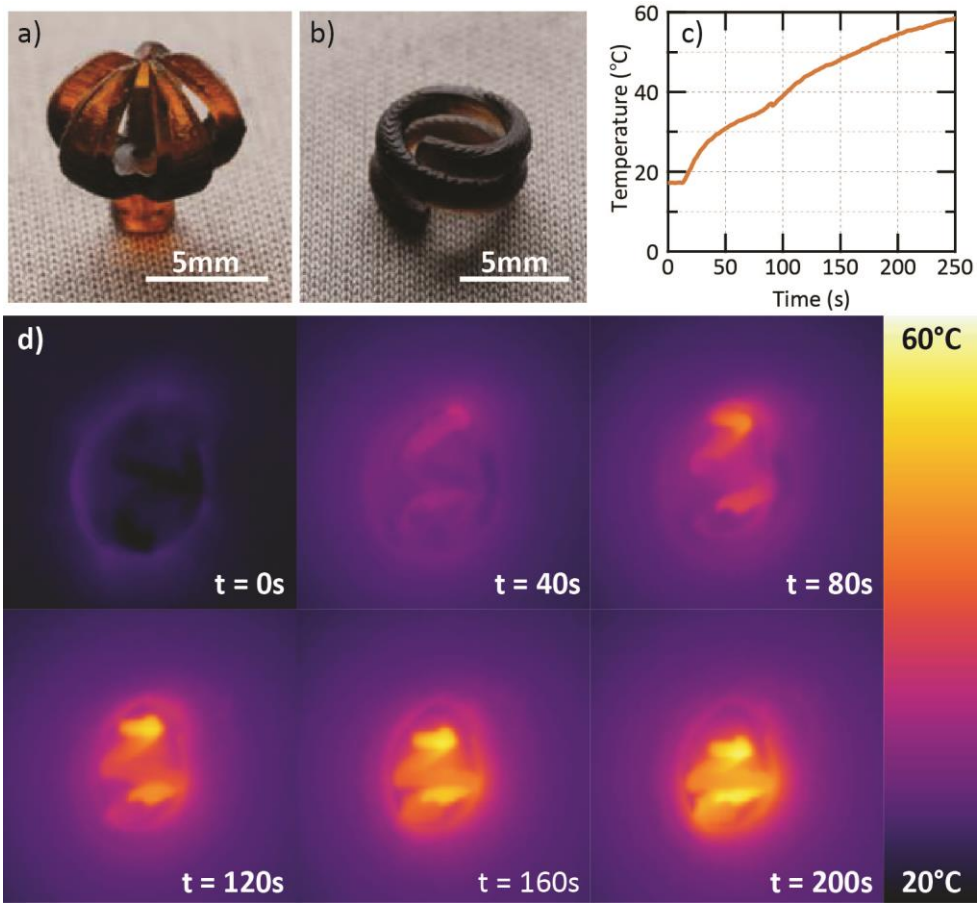

Figure 5.3 (a) 3D printed shape memory polymer composite claw, incorporating MNPs into the part of the shape that is strained when the claws are opened. (b) 3D printed shape memory composite spring. Both structures are courtesy of the lab of Prof. Qi "Kevin" Ge at SUTD. (c) Temperature change over time is shown for a composite spring like the one shown in (b) under exposure to an AMF with $\boldsymbol{H_0 = 20 kA/m}$ and $\boldsymbol{f = 680 kHz}$. (d) An IR thermography video taken over several minutes shows the heating and shape memory response of 3D printed composite spring. It starts frozen in its glassy state in a stretched configuration and collapses back to its printed shape upon being heated by an AMF.

Several of the characterization methods described in Chapter 4 for MNPs in solid samples were developed initially in order meet the needs of this project. The availability of a UV curable monomer with a measured specific heat made this composite system a convenient one in which

the study the heat dissipation of MNPs in environments that preclude rotation. A preliminary demonstration of an AMF actuated shape memory response is shown in Figure 5.3.

Although these initial results are promising, the most persistent challenge is stable suspension of the MNPs in the monomer solution. MNPs are currently transferred from chloroform into the monomer solution as synthesized,[90] presumably with a surface on which oleate is adsorbed as a remnant of the synthesis reaction. MNPs suspended in this way readily disperse under the influence of ultrasonication and vortex mixing, but settle over a timescale of hours. While this is sufficient to prepare planar samples for characterization, the issue is compounded by the need for stability within the topmost fraction of a millimeter of the solution for additive manufacturing. The structures produced for the initial demonstration therefore required frequent pausing and mixing of the suspension, a situation that limits the robustness of such techniques. Efforts to reduce magnetic dipole interactions, which are known to contribute to settling, have improved but not eliminated the issue. Ongoing efforts may include the synthesis of a polymer surface coating for the MNPs that favorably influences their stability in the monomer solution.

5.4 Multiplexing Applied to Bulk Heated Systems

Ideal magnetothermal multiplexing in bulk systems can be envisioned as the selective heating of two or more separate regions occupied by high concentrations of different types of MNPs. An intriguing and similar idea explored in literature is that of frequency-selectable macroscopic inductive heating targets.[109] By incorporating them into temperature sensitive viscous gel dampers of a dynamic vibration absorber (DVA), a noncontact method for adjusting the natural frequency of the DVA has previously been demonstrated. A similar effect could

perhaps be achieved with MNPs incorporated into gels, but they dissipate far less heat than macroscopic eddy currents and their properties make them more readily suited to biomedical applications.

Section 1.5 discussed scoring functions for quantitative comparison of efficiency, selectivity, and parity in potential multiplexing MNP sets. For bulk heating applications, it is most appropriate for these quantities to be defined in terms of SLP. Moreover, achieving parity in a bulk heating system is less important than efficiency and selectivity, since concentration in the regions can in principle be adjusted to produce parity in the expected temperature change.

In the case of neuronal stimulation with ferrofluid droplets, magnetothermal multiplexing could offer the option of stimulating two or more separate droplets. These could be implanted in different brain structures, perhaps to elicit different therapeutic responses. By contrast, attempting to independently heat these droplets by selective exposure to a focused AMF is especially implausible for targeted regions close to each other and deep in the brain. A preliminary experiment could take place in rodent models, where c-fos staining or behavioral observation could be used to assess the effectiveness of multiplexing. (Figure 5.4(a))

3D printing of shape memory structures consisting of multiple materials with different transition temperatures has recently been demonstrated.[108] If the same can be done with shape memory composites incorporating different types of MNPs suitable for multiplexing, then it should be possible to actuate multistage shape memory response by heating. This capability, combined with the versatility of 3D printing could offer numerous intriguing possibilities. A graphical representation of the concept is shown in Figure 5.4(b).

As a practical example of a heuristic search, the SLE data from Figure 4.7(a) were extrapolated to identify MNPs well-suited for magnetothermal multiplexing in 3D printed shape

memory composites. Using an algorithm that sampled many possible combinations, comparing them with an overall score based on efficiency and selectivity, the selection shown in Figure 5.4(c) was determined to be suitable.

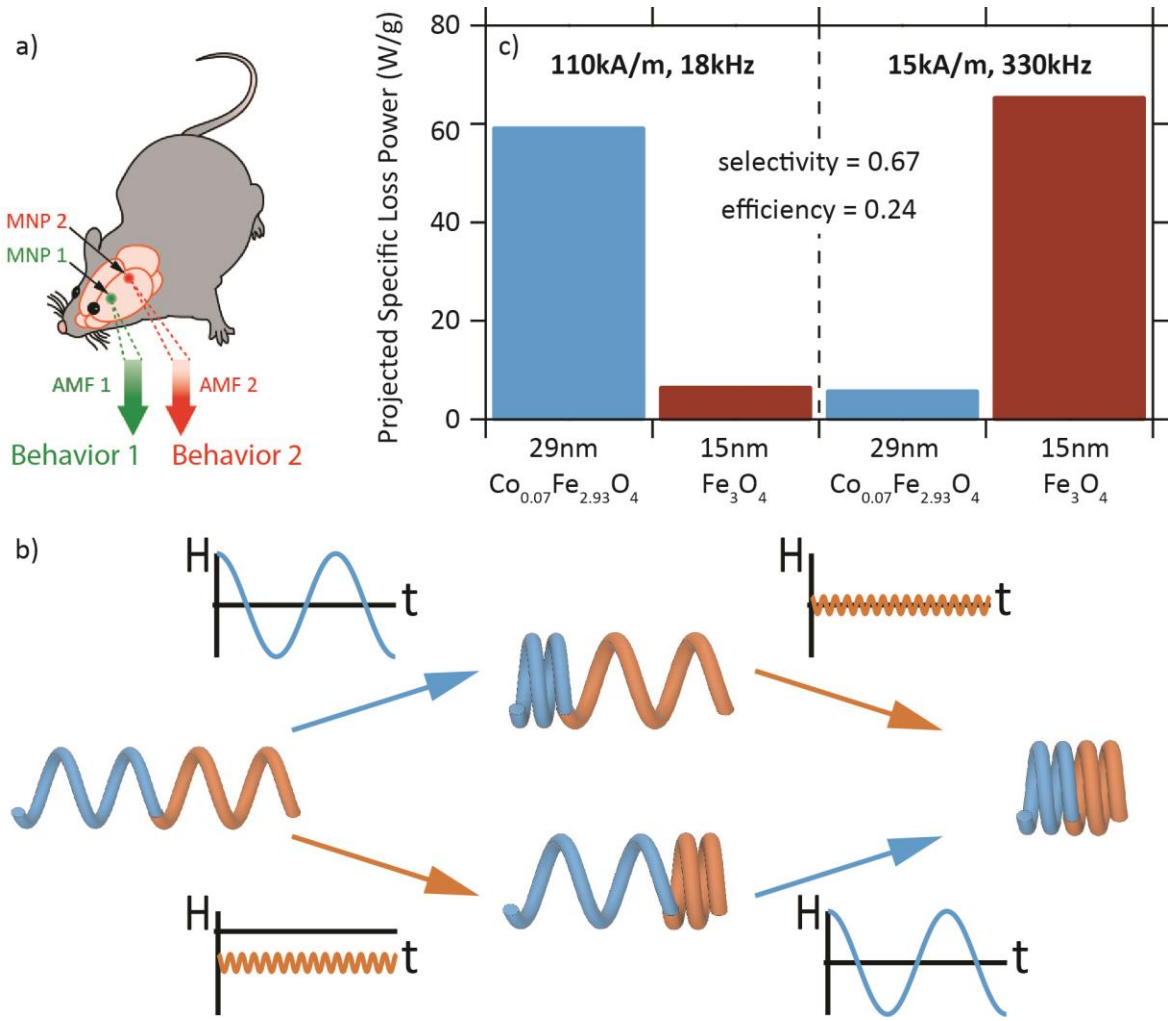

Figure 5.4 (a) Magnetothermal multiplexing could be applied to the selective heating of different ferrofluid droplets in the brain of an animal model in order to stimulate different structures associated with distinct behaviors. (b) A multimaterial 3D printed shape memory composite could exhibit a multistage shape memory response through selective heating of different regions. (c) Materials and AMF conditions from among the choices available in Figure 4.7 are suggested for the application depicted in (b) based on algorithmic sampling of heuristically extrapolated heating rates as described in Section 4.7.

6 Applications Based on Nanoscale Heating of MNPs

6.1 The Peculiarity of Nanoscale Heating

As the scale of a hypothetical heat dissipating object is reduced, bulk heat transport equations predict that its tendency to raise the temperature of its surroundings should be dramatically lessened. This may seem obvious in the sense that shrinking size combined with the assumption of constant heat dissipated per unit volume or mass results in less total dissipated power, but the trend is actually even more dramatic than this observation alone would suggest. Even if the temperature change is considered along a spatial coordinate that is scaled with the object, the expected change in temperature is reduced. An intuitive explanation is that, all else being equal, the surface area to volume ratio increases with decreasing size, allowing smaller bodies to exchange heat more efficiently with their surroundings. Recognizing this trend is a matter of direct relevance to applications of MNPs for bulk heating, which for instance limits the feasibility of cancer hyperthermia to tumors larger than a few cubic millimeters[44] or, in principle, limits the size of shape memory devices such as those explained in Section 5.3. A well-reasoned argument based on this logic has also been used to assert the implausibility of nanoscale heating at the surface of MNPs,[110] and it is worth considering in greater depth.

To estimate the order of magnitude of temperature increase predicted by bulk heat transport equations, it is useful to consider steady state heat dissipation by an isolated sphere, a geometric approximation of an MNP. For simplicity, the analysis is confined to the temperature of the medium surrounding the particle and not the temperature inside the MNP itself. Bulk heat transport can be described mathematically by diffusive flow of heat, and the details of this treatment are offered in Appendix N. The result is that at the surface of the sphere, the expected change in temperature ΔT can be expressed as follows:

$$\Delta T(R) = \frac{R^2(\mathrm{SLP})\rho_m}{3K} = \frac{\mathrm{IPLP}}{4\pi KR} \qquad 6.1$$

Here, R is the radius of the particle, ρ_m is mass density and IPLP is individual particle loss power. If values are substituted for a series of MNPs with different sizes with characterized SLPs at 15kA/m and 500kHz, and assuming approximate thermal conductivity $K \approx 0.5\frac{W}{mK}$ for water,[111] predicted temperature changes are on the order of 10^{-7} K (Figure 6.1). This indicates that the temperature at the surface of the nanoparticle is not predicted to differ significantly from that of its bulk surroundings, even for SLPs substantially higher than the range of values currently observed.

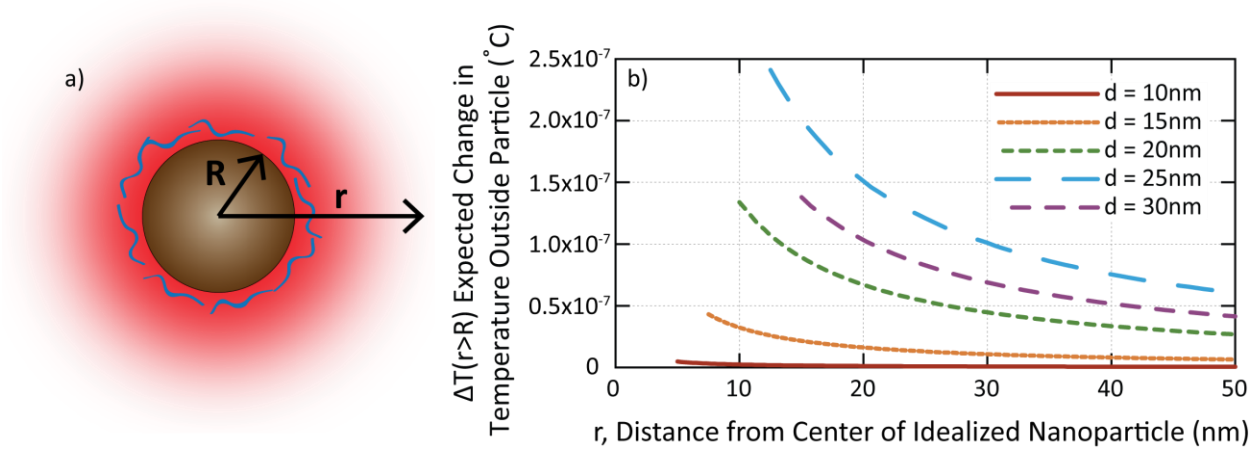

Figure 6.1 (a) A sketch of an idealized MNP as a heat dissipating sphere of radius $\boldsymbol{R}$, with temperature measured at radial distance $\boldsymbol{r}$. (b) The change in temperature at the surface and in the immediate vicinity of the MNP is plotted as predicted by bulk heat transport equations. An assumption for the heat dissipated by the MNP is estimated from measured SLP at an AMF with $\boldsymbol{H_0 = 15kA/m}$ and $\boldsymbol{f = 500kHz}$. Nominal physical dimensions are assumed. Note that the prediction is for no significant nanoscale heating. Adapted from supplementary materials of Romero et al. [95]

Surprisingly, these predictions depart dramatically from experimental observations that have attempted to probe temperature in the nanoscale vicinity of the surface of the MNPs; these suggest a temperature change many orders of magnitude larger (reaching even 10s of degrees

Celsius)[112] that may evolve over a long timescale of seconds or tens of seconds before reaching steady state.[113]

The body of empirical evidence for nanoscale heating effects is derived from a variety of different techniques, several of which address systems with nanoparticles and surface chemistries directly comparable to the ones employed in this thesis. For instance, one study by Huang et al focused on the use of nanoscale heating from MNPs for neural stimulation produced a set of observations based on thermal quenching of fluorescent dye conjugated to the surface of MNPs, indicating temperature changes on the order of degrees Celsius.[12] Another study by Riedinger et al. made use of a thermally labile azide bond which released a dye molecule at a temperature dependent rate.[112] Combined with PEG spacers of varying length, these researchers used this system to probe temperature as a function of distance, with their results suggesting that the temperature at the surface of the MNPs changed by tens of degrees Celsius in some cases, and seemed to drop off more rapidly than the $1/r$ dependence suggested in Appendix N.

Similar observations have been made in related, though distinct material systems. For example, observing temperature dependent refractive index of polymers surrounding gold nanoparticles indicated changes in surface temperature comparable to observations with MNPs.[114] More recently, another study probed nanoscale thermal phenomena through the observation temperature dependent upconversion luminescence spectra of nanocrystals embedded in mesoporous silica alongside MNPs.[113] Their results again suggested a temperature increase of similar magnitude to the others, and moreover indicated that this temperature change can take tens of seconds to reach steady state. In one particularly striking experiment, localized heating was observable via luminescence in a system suspended in equilibrated ice water.

Forceful rebukes against the notion of nanoscale heating in these kinds of systems have been voiced for decades, but the quality and variety of experimental evidence now available suggests that the problem deserves reexamination. The reasoning behind the bulk heat transport arguments is sound, suggesting that its application to this situation may be in some way unwarranted. Indeed, macroscopic heat transport is known to fail at the nanoscale in some types of solid-solid systems.[115] Heat transport at the interfaces between nanostructures and the media surrounding them often requires ballistic models, particularly when the structures exhibit length scales less than the mean free path of phonons.[115] Several of the authors employing bulk heat transport are aware of this limitation and argue that diffusive heat flow is adequate for water even at the scale of nanometers because the disorder of a liquid results in effective mean free paths so short they are comparable to intermolecular spacing.[110] The problem of solid crystalline nanoparticles dissipating heat in a solid crystalline matrix has been studied in some theoretical depth, and can result in effective interfacial thermal conductivities far reduced from the bulk interfacial thermal conductivity. It is unclear whether this model can fully explain the discrepancy, even in its limiting cases, and it is possible that some other factors may be playing an unexpectedly significant role.

While nanoscale heating is clearly a topic worthy of further study, the work presented in this chapter instead focuses on making use of the effect to accomplish engineering outcomes. From this perspective, nanoscale heating is appealing because it enables response to AMF at low concentrations of MNPs. In cases where direct injection into the targeted structure would ostensibly take place, this allows for a much smaller dose of MNPs and by extension a smaller dose of heat dissipated in healthy tissue. For other applications, such as the protease sensors explored in Section 6.3, it allows for systemic delivery of theranostic agents. Methods that avoid

repeatedly heating healthy cells beyond normal physiological conditions, even for short durations, may produce fewer unintended consequences. In short, making use of material responses based on nanoscale heating ultimately may prove to be more desirable for many applications.

6.2 Neuronal Stimulation via Rapid Release of Pharmacological Compounds

An alternative to using the direct action of heat upon a channel protein to elicit neural activity is to instead use heat to trigger the release of a chemical compound that can act upon the channel protein. TRPV1, the channel protein which was employed in the ferrofluid stimulation scheme described in Section 5.2 as well as previous literature making use of nanoscale heating, responds to a variety of chemical agonists in addition to heat. Among these is allyl isothiocyanate (AITC), which gives horseradish and wasabi their pungency.[116] By linking an AITC payload to the polymer coating of an MNP via a thermally labile azide bonds, its release can be triggered through the action of an AMF by a temperature increase within the first several nanometers from the surface of the MNP. After release, AITC can bind to TRPV1, allowing the influx of divalent ions. (A schematic representing the concept for this mechanism of stimulation is shown in Figure 6.2.)

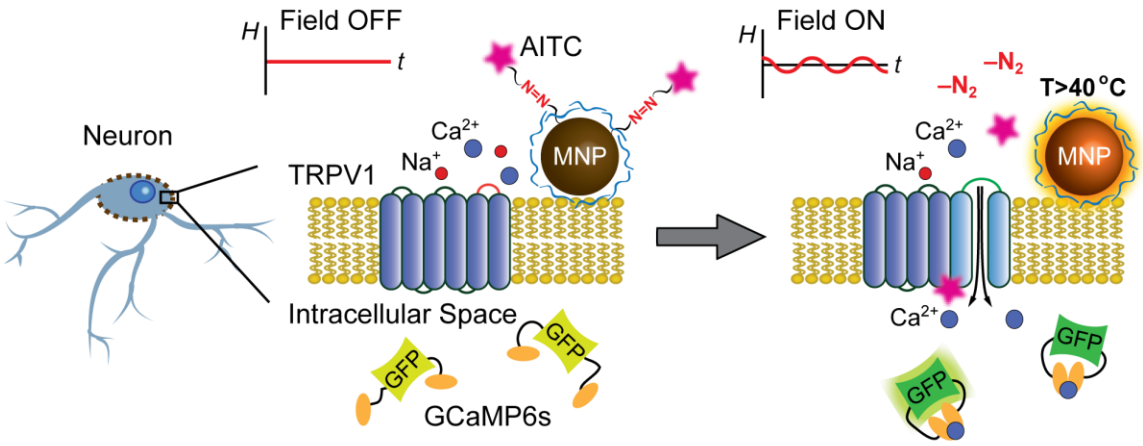

Figure 6.2 An overview of the experimental scheme. Functionalized MNPs target the surface of neurons made to express TRPV1 and GCaMP6s. Upon exposure to an alternating magnetic field, the heat dissipated by magnetic hysteresis results in the release of AITC from their surfaces. This liberated AITC binds to TRPV1, triggering Ca^{2+} influx detectable through the fluorescence increase of GCaMP6s. From Romero et al. [95]

An earlier study by Riedinger et al. making use of a similar azide linker focused on probing temperature as a function of distance from the surface of MNPs, but exposure to AMFs in that work lasted for durations of 45 minutes and produced incomplete release.[112] In that work, release was compared against a calibration curve from control trials performed in water baths at set temperatures and partial release in the main experiment was necessary to unambiguously deduce a nanoscale temperature measurement. In contrast, the goal of producing a robustly measureable experimental signal assessing neuronal stimulation *in vitro* makes it desirable instead to release an entire payload as rapidly as possible. Accordingly, an effort was made to alter the system to encourage rapid release.

As a preliminary experiment, a series of different iron oxide MNPs with nominal diameters of 10nm, 15nm, 20nm, 25nm, and 30nm were purchased from Ocean Nanotech, LLC and conjugated with dye as chemical payload rather than AITC. Dilute aliquots of dye-functionalized MNPs were then exposed to an AMF for varying durations while their temperature was monitored and a custom sample holder continuously perfused the surrounding

space with room temperature water to ensure that the influence of waste heat from the coil could be mitigated. The extent of release after exposure to an AMF with amplitude 15kA/m and frequency 500kHz is shown in Figure 6.3(b). Several results are notable:

1. Rapid release was observed for many of the MNPs, which were larger and driven at more aggressive AMF conditions than the ones in used by Riedinger et al.[112]
2. Even though the 20nm and 25nm MNPs have similar SLPs (Figure 6.3(c)), the 25nm MNPs released their payload more rapidly and completely, suggesting a higher effective temperature at the surface. This is consistent with the notion that IPLP may be a more relevant metric for the heating of individual particles, since the IPLP of the 25nm MNPs exceeds that of the 20nm MNPs by approximately a factor of two due to their volume difference (Figure 6.3(d)).
3. For the 25nm MNPs, a rapid and complete release occurred after 10 seconds of latency, which is consistent with the idea that the large temperature increases at the surfaces of these MNPs develop over timescales of seconds,[113] not reaching steady state in hundreds of nanoseconds as bulk heat transport would suggest.[110]

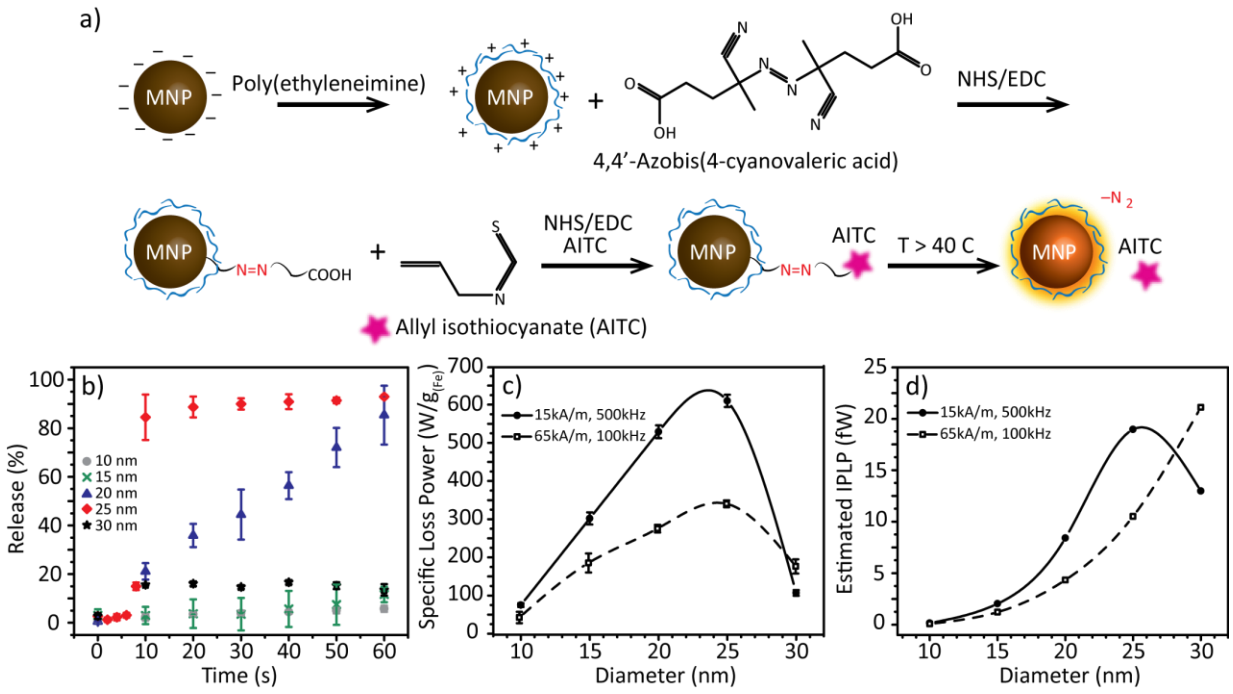

Figure 6.3 (a) The chemistry for loading the MNPs is shown. MNP surfaces are supplied with carboxyl termination. The surface is electrostatically coated with poly(ethyleneimine), followed by the covalent attachment of ACVA through NHS/EDC chemistry. An additional step of NHS/EDC chemistry binds AITC to ACVA. Exposure to an AMF results in decomposition of the linker, releasing AITC. (b) Release under exposure to an AMF with $H_0 = 15\text{kA/m}$ and $f = 500\text{kHz}$ is shown for MNPs of various sizes functionalized with the dye CF633. Release is compared to controls incubated at 60˚C for 24 hrs. (c) Specific loss powers are shown for the MNPs in (b) as measured by AMF calorimetry. (d) IPLP is estimated from SLP and nominal physical dimensions. From Romero et al.[95]

Having identified a suitable material system and surface chemistry to produce rapid release, an *in vitro* experiment was designed to test the hypothesized mechanism of stimulation. Primary hippocampal cultures were prepared from neonatal rats, transfected with TRPV1 and GCaMP6s, and incubated overnight with a low concentration (25μg/mL) of the 25nm Ocean Nanotech MNPs functionalized with AITC. By exposing samples to AMF and measuring changes in the fluorescence of GCaMP6s attributable to calcium influx, it was possible to compare relative levels of elicited neural activity (Figure 6.4). In addition to trials that included all components, a series of control trials was performed in which various components were subtracted, including

the AMF stimulus, TRPV1, the AITC payload. All of these control trials exhibited significantly less induced activity. As an additional control, in one set of trials, loaded MNPs were added to the media just before AMF exposure rather than allowing overnight incubation, during which the MNPs are targeted to the membrane through a weak electrostatic interaction. These exhibited less responsiveness than the trials that allowed time for incubation, but significantly more responsiveness than the other control trials.

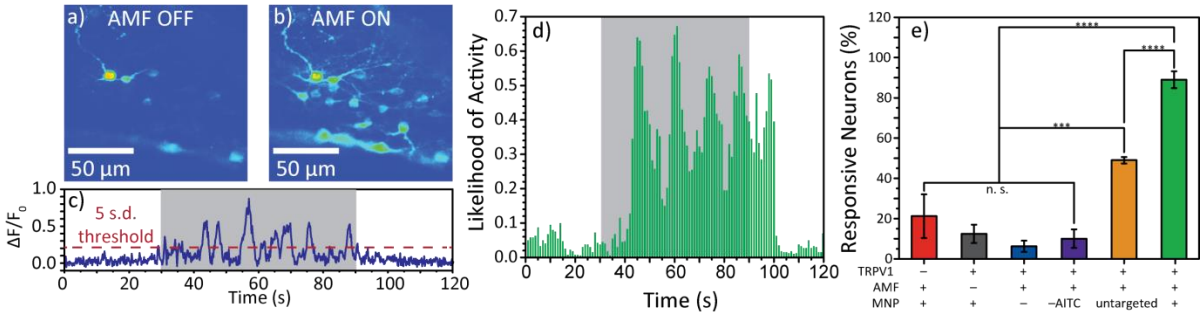

Figure 6.4 False color images indicate GCaMP6s florescence signal from a representative trial of primary hippocampal neurons transfected with AITC, incubated with 25µg$_{(Fe)}$/mL AITC-functionalized MNPs overnight, (a) before and (b) after exposure to an AMF with $\boldsymbol{H_0 = 15 kA/m}$ and $\boldsymbol{f = 500 kHz}$. (c) Fluorescence signal from a single neuron is plotted over time, with a level of five standard deviations from background noise serving as a threshold for "activity." (d) 100 neurons were randomly selected for analysis and the proportion exceeding the threshold in a given second ("likelihood of activity") is shown as a function of time. The grey bar represents AMF exposure. (e) The percentage of responsive neurons is compared between the response represented in (d) and control trials that remove various components thought to be necessary for the mechanism of stimulation. Adapted from Romero et al.[95]

The intent of this study was primarily a preliminary exploration of using rapid, magnetothermally mediated release to stimulate cellular responses. Because the method was based on nanoscale heating effects, the concentration could be reduced by at least three orders of magnitude compared to the ferrofluid stimulation method detailed in Section 5.2. Some modifications would be required for greater clinical viability, perhaps including the release of compounds such as neurotransmitters which would be able to influence neurons without requiring transfection. While the approach taken in the study was to select for materials and

conditions that would lead to rapid and complete release, an actual therapy would likely require incremental release, though the data shown in **Figure 6.3**(b) suggest that this is possible.

6.3 Magnetically Actuated Liposomal Release for Protease Sensors

Proteases, enzymes that act upon proteins and peptides, take an active role in tumors, occurring both intracellularly and extracellularly, and contributing to nearly every hallmark of cancer.[117] Matrix metalloprotinases in particular have been implicated in tumorigenesis, progression, invasion, and metastasis.[118] Some emerging cancer therapeutics interact with these proteases,[119] and in order to be effective, these and other personalized treatments must be appropriately tailored to individual tumor environments. Robust diagnostic methods to profile protease activity in tumors can help inform clinical care. One approach is to introduce substrates known to be selectively cleaved by particular proteases, liberating a reporter molecule detectable in the urine.[120] However, because many of the same proteases perform natural and healthy functions throughout the body, systemic introduction can lead to a poor signal to noise ratio, resulting in diagnostic uncertainty.[121]

Several strategies are possible to obtain a spatially specific biomarker readout despite systemic introduction, including site specific imaging methods.[122] However, compared to these methods, the approach investigated in this section offers the advantage of simultaneous measurement with multiple protease substrates. It entails protecting these substrates from cleavage by encapsulation in liposomes that undergo triggered release through the application of an AMF to the tumor (Figure 6.5(a)-(b)). This is enabled by co-encapsulation of MNPs expected to exhibit nanoscale heating effects in liposomes that exhibit a phase change making them permeable when heated above a critical temperature.[123] An initial experiment was conducted to

assess the effectiveness of release triggered by AMFs using florescence measurements on liposomes loaded with MNPs and homeoquenching calcein dye (Figure 6.5(c)-(d)).

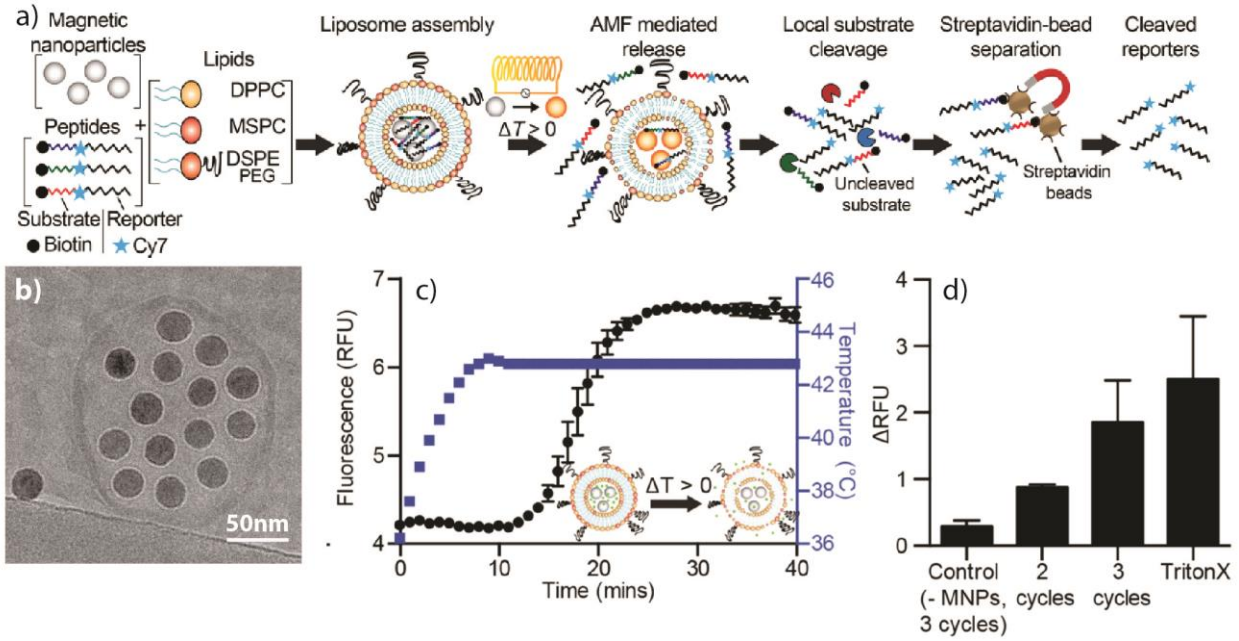

Figure 6.5 (a) A conceptual sketch for magnetically actuated protease sensors is shown. (b) A cryo-transmission electron micrograph shows MNPs encapsulated in a liposome. (c) Release was quantified by an increase in calcein fluorescence signal for liposomes exposed to temperatures above 37˚C (N = 5). (d) Similarly quantified release is shown for liposomes loaded with MNPs exposed to 40 second "cycles" of an AMF with $\boldsymbol{H_0 = 15 kA\,m^{-1}}$ and $\boldsymbol{f = 515 kHz}$,. Signal is compared to a control trial without MNPs and a trial in which the liposomes were disrupted with the surfactant TritonX. Adapted from Schürle et al.[92]

After establishing the capability of this system for triggered release, a set of *in vivo* experiments was performed on immunocompromised mice with xenografted flank tumors exhibiting known protease phenotypes. It was hypothesized that after a systemic tail vein injection, the liposomes would circulate throughout the animal accumulating preferentially in the tumor due to the enhanced permeation and retention effect caused by the leaky and defective vasculature of tumors.[124] During circulation, the protease specific substrates would be protected by the liposomes from premature cleavage. Upon exposure to an AMF at the site of the tumor, the substrates should be released and if their corresponding proteases are present in the tumor

microenvironment, they will be cleaved, liberating a fluorescent reporter for detection in the urine.

A control group ("Group A") was not exposed to an AMF, whereas another group ("Group B") was exposed to an AMF by an electromagnet of the design explained in Section 3.5 at the site of the tumor. Urine was collected for assay at time points before and after the AMF was applied. (**Figure 6.6**(a) shows the timeline of the experiment.) The signal measured in the urine before AMF exposure did not show a significant difference between the two groups, validating the consistency of the baseline signal in the two groups prior to AMF exposure. As anticipated by the hypothesis that release of the substrates would be triggered by the AMF, Group B showed a significant increase in the reporter signal detected in the urine (Figure 6.6(b)-(c)). To test the diagnostic capability of this system, liposomal release of a mixture of three substrates was triggered by AMF exposure in groups of mice with two different types of tumors known to have distinct protease phenotypes: LS174T and HCT8.[125] The relative signal in the urine for the reporter molecules associated with these substrates was consistent with known protease profiles of the two tumor types (**Figure 6.6**(d)-(e)).

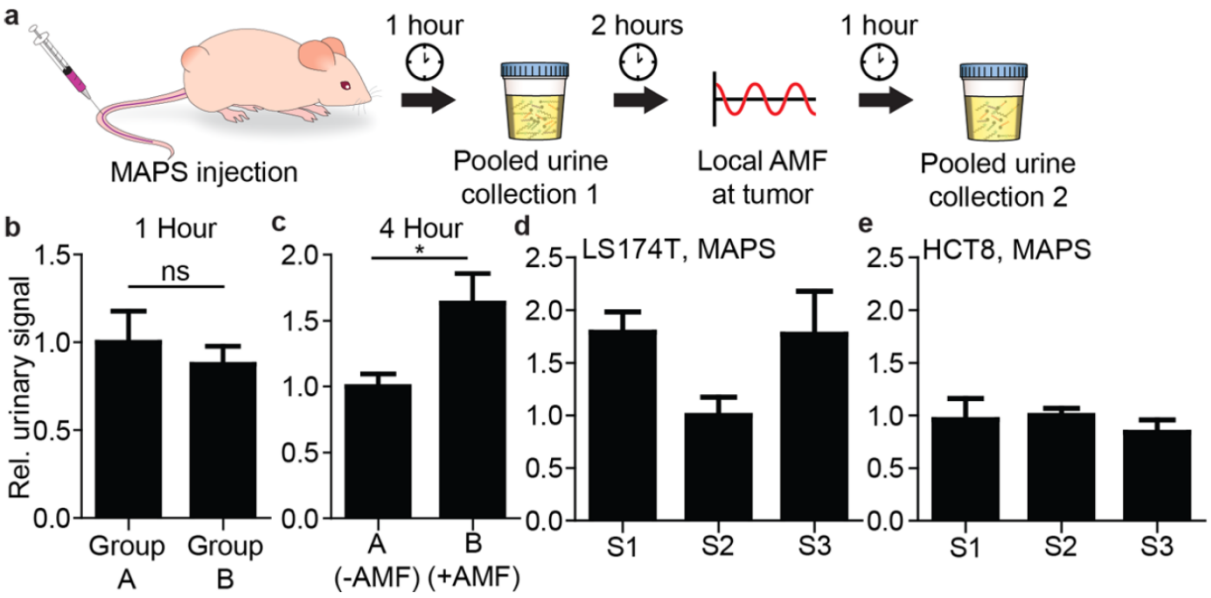

Figure 6.6 (a) Schematic timeline for the *in vivo* tumor profiling assay. Magnetically activated protease sensors (MAPS) were administered by a tail vein injection, and urine was collected to measure background signal after 1 hour. 2 hours later, AMF was applied to the tumor in group B. Urine was collected from both groups A and B one hour later. (b) Prior to activation, groups A and B exhibit similar background levels. (c) After exposure to AMF, detected reporter concentrations significantly increased for the group exposed to AMF ($n = 5$; *, $P < 0.05$ Student's t test; data normalized to Group A). MAPS urinary signatures after activation across the three substrates (S1, S2, S3) for (d) LS174T and (e) HCT-8 indicate that S1 and S3 are cleaved more rapidly than S2 in LS174T tumors ($n \geq 5$ per group; data normalized to S2 signal for both LS174T and HCT8). From Schürle et al.[92]

Provided that AMFs scaled to the human body can be sufficiently focused to trigger release primarily within a tumor, this method represents a promising diagnostic approach. It should be noted that other magnetothermally actuated liposomal release schemes have been studied, and these have the advantage of compatibility with release of contents including drugs, signaling molecules, viruses, etc.[126, 127] These payloads are not subject to the same chemical restrictions as the method in the previous section, which relied upon covalent attachment to a thermally labile bond.

6.4 Disruption of Amyloid β Aggregates

Plaques containing a misfolded and aggregated version of the protein amyloid beta (Aβ) have long been associated with Alzheimer's disease, though their role remains unclear.[128] One route to investigate the role of these plaques in Alzheimer's pathology has been to attempt to clear them away. This includes methods that use local heating of gold or graphene oxide nanoparticles to disaggregate Aβ deposits under exposure to microwave or near infrared radiation.[129, 130] While these forms of electromagnetic radiation clearly can penetrate tissue more effectively than visible light, scattering and absorption are still a concern. In the case of NIR, experiments with cadaver heads have indicated that the delivered NIR intensity drops by about an order of magnitude per centimeter of penetration.[131] The absorption of tissue in the microwave range makes this a less than ideal band for delivering energy to nanoparticles without also indiscriminately heating the surrounding tissue.[132]

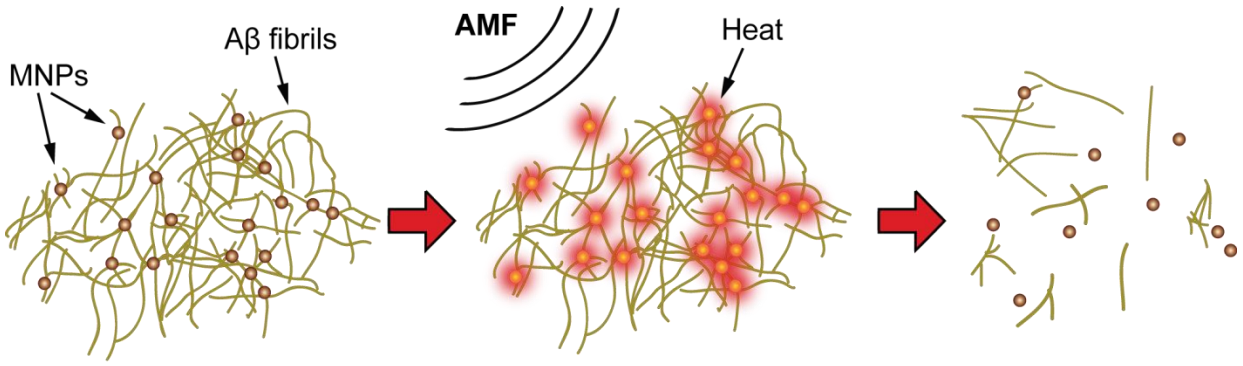

Figure 6.7 Conceptual sketch for protein disaggregation using alternating magnetic field and MNPs. Under exposure to an AMF, targeted MNPs dissipate heat, leading to fragmentation of amyloid aggregates. From Loynachan et al.[133]

Since MNPs exhibit local heating effects and AMFs should penetrate tissue substantially undiminished provided that they can be successfully scaled to clinically relevant dimensions, it is similarly worthwhile to consider whether this nanomaterial system can be used to disrupt Aβ aggregates. To do this, a surface chemistry designed to produce stable suspension of MNPs in

solution and targeted binding to Aβ was developed. Starting with MNPs coated with poly acrylic acid, 10kDa poly ethylene glycol (PEG) was grafted to the surface with carbodiimide chemistry. Then the carboxymethyl end group of the PEG was functionalized with a peptide sequence (leucine-proline-phenylalanine- phenylalanine -aspartic acid, LPFFD) known to bind to a hydrophobic domain on the Aβ structure.[134] Both PEG and LPFFD have been shown to influence the aggregation behavior of Aβ, but the MNPs were used in such limited concentration in this study (28μg/mL Fe) that the corresponding quantity of PEG and LPFFD was low enough to rule out these mechanisms.[134, 135]

Aβ was procured through collaboration with the Walsh laboratory of Harvard University and aggregates self-assembled as verified through thioflavin T fluorescence[136] and dynamic light scattering.[137] Analysis of transmission electron micrographs comparing the coverage of MNP-PEG to MNP-PEG-LPFFD suggested that LPFFD is correlated with preferential binding to Aβ aggregates. The MNPs tend to bind in clusters, and a simple model based on pseudorandom seeding of MNPs onto a grid of sites suggested that even MNPs well suspended in solution would tend to cluster in their binding behavior (Appendix O).

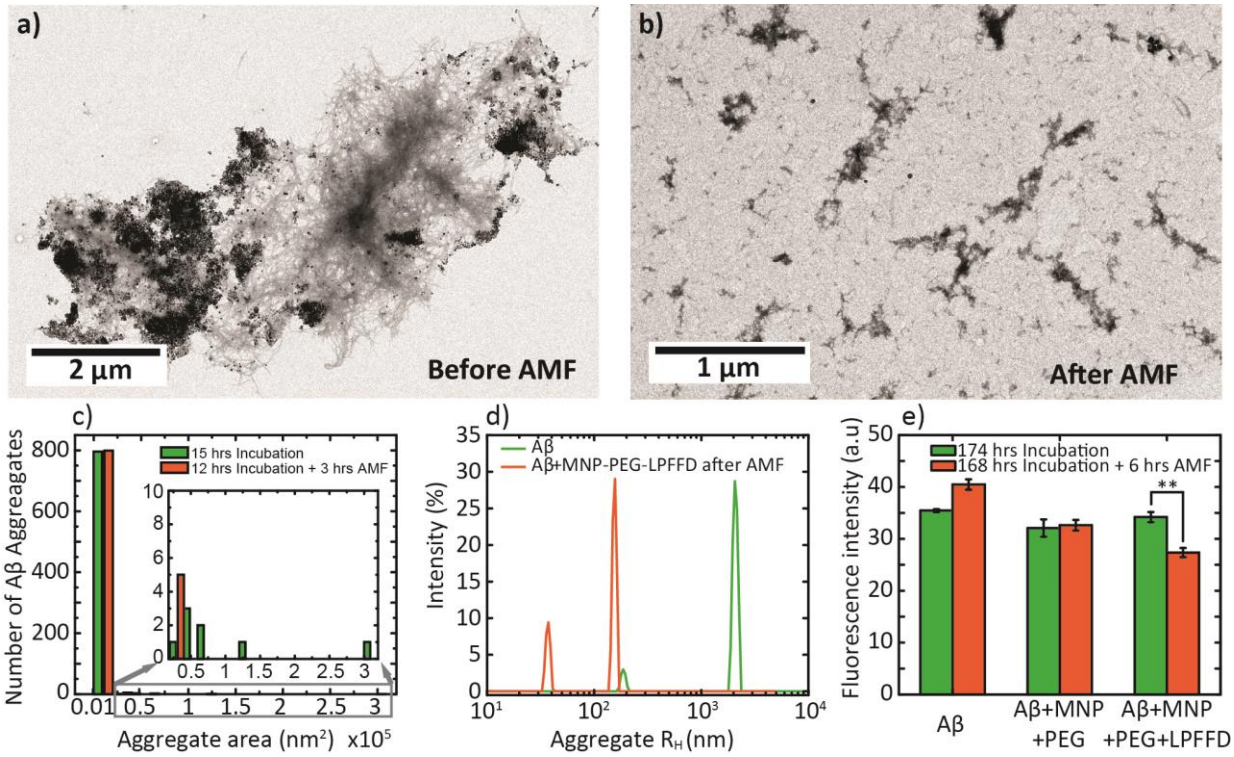

Figure 6.8 (a), (b) Representative TEM images of Aβ (168 hours) decorated with MNP-PEG-LPFFD, (a) untreated and (b) exposed to an AMF with $H_0 \approx 28\text{kA m}^{-1}$ and $f \approx 100\text{kHz}$ for 6 hrs. (c) Histogram of the areas of aggregates analyzed from 8 randomly selected TEM images from each sample set. AMF-exposed samples (orange) and no AMF exposure (green). (d) Dynamic light scattering is used to measure the average aggregate size for Aβ alone with no AMF exposure (green), mean value: 1191 ± 198 nm and Aβ + MNP-PEG-LPFFD after exposure (orange) to 3 hour AMF, mean value: 387 ± 12.5 nm. (E) Fluorescence intensity of AMF-treated (orange) and untreated (green) samples (Gain = 177). A decrease in intensity is observed for Aβ targeted with MNP-PEG-LPFFD following AMF, correlated with the disruption of the β-sheet structure. Number of trials n = 3, Student's t-test p = 0.003. Adapted from Loynachan et al.[133]

A series of experiments was conducted to assess the extent of AMF induced disaggregation of the Aβ structures as indicated by several distinct lines of evidence including TEM on dried samples, dynamic light scattering, and Thioflavin T fluorescence. These experiments made use of AMF electromagnet setup capable of applying an AMF with an amplitude of 28kA/m at a frequency of 100kHz continuously for up to 6 hours, while producing consistent background heating that maintained the samples at 34±1˚C. Together, all three lines of evidence strongly suggest that the exposure of samples with MNPs targeted to Aβ aggregates

tend to break those aggregates into smaller fragments without entirely eliminating them (Figure 6.8(c)-(e)). Elevated temperature has been suggested by atomistic modeling to introduce defects into aggregates, causing them to bend or break,[138] so some form of nanoscale heating from the MNPs could have played a significant role, though this assertion was not tested directly in the study.

Because previous studies have suggested that short soluble Aβ oligomers can exhibit cytotoxic effects,[139] a subsequent *in vitro* experiment was conducted combining Aβ aggregates with primary hippocampal cultures extracted from neonatal rats (Figure 6.9(a)). A colorimetric assay was used to assess the viability of these cultures to assess whether disaggregation of Aβ influenced the health of the cells. All trials received a 3 hour exposure to AMF (Figure 6.9(b)), with a control group left unexposed to Aβ, a group exposed to Aβ and no MNPs, a group exposed to Aβ and untargeted MNPs, and finally a group exposed to Aβ and targeted MNPs. The group exposed to Aβ and left untreated showed significantly reduced viability as compared to the other groups, though no significant difference was distinguished between the targeted and untargeted MNPs. (Figure 6.9(c))

To put this study into context, it should be acknowledged that pharmacological approaches have been demonstrated to reduce or eliminate the plaques associated with Alzheimer's disease, and yet have failed to show significant improvement in clinical trials.[140] The inherent invasiveness of introducing MNPs throughout the brain makes the likelihood of a widespread adoption quite low for a treatment based on this, especially considering the existence of compelling alternatives. One recently reported method even purports to entirely circumvent the introduction of any foreign substance into the body, instead using a light pulsed at 40Hz to stimulate an immune response that clears the plaques.[141] The disruption of protein aggregates

observed in this study may have relevance to other diseases that involve misfolded proteins, or more broadly represents a mechanism of noninvasive protein manipulation that could be useful in other therapeutic contexts.

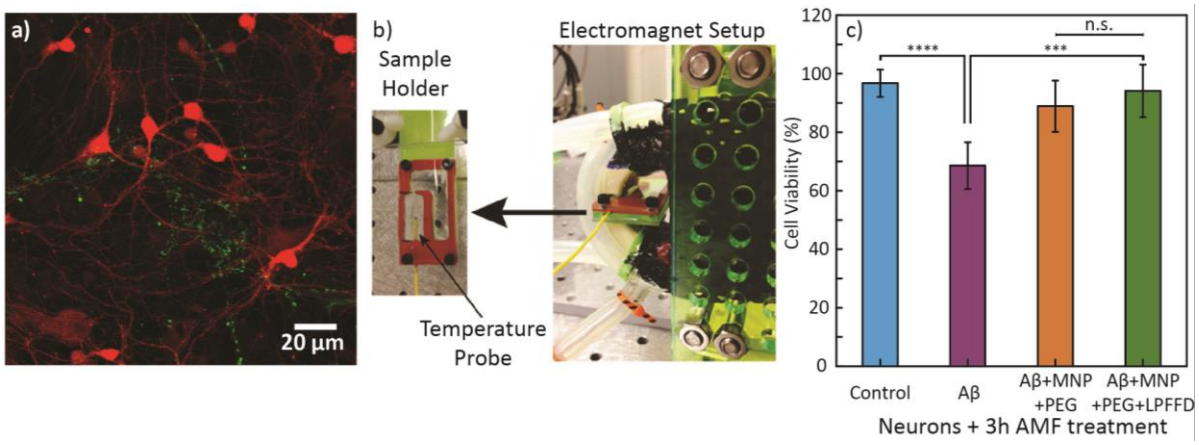

Figure 6.9 (a) Confocal microscopy image of hippocampal neurons incubated with Aβ aggregates. Neurons were transfected with mCherry (red) and Aβ was stained with thioflavin T (green). (b) The experimental setup used for the in vitro viability study is shown. (c) Cell viability assessed by colorimetric assay of hippocampal neurons after 3h AMF treatment (control), and after 3h AMF treatment in presence of Aβ, Aβ+MNPs-PEG, or Aβ+MNPs-PEG-LPFFD. Adapted from Loynachan et al. [133]

6.5 Magnetothermal Multiplexing Applied to Nanoscale Heating Systems

For systems based on nanoscale heating, the possibility of multiplexing is particularly exciting because responses can be actuated in overlapping spatial regions with low concentrations of MNPs. Emerging applications that utilize selective independent heating of plasmonic gold nanostructures offer appealing analogues for what may eventually be possible with MNPs. For instance, Lee et al. demonstrated independent control of two genetic circuits using the thermally driven release of siRNA from gold nanorods engineered to respond selectively to 785nm and 660nm irradiation.[142] Puig et al. used a similar selective plasmonic heating scheme with two types of gold nanorods for bidirectional control of blood clotting.[143] In this study, triggered release of a thrombin binding aptamer inhibited clotting and then release of

the complementary single stranded DNA counteracted its effects. Though such strategies would certainly need to be modified for compatibility with magnetothermal multiplexing, these examples serve to illustrate the kinds of actuation that may eventually be possible.

Some of the nanoscale heating applications explored in this thesis could serve as a starting point for demonstrating magnetothermal multiplexing. For instance, a mixture of liposomes containing different types of MNPs and different payloads could undergo selective release triggered by AMFs. In the case of neuronal stimulation, AMF conditions could be chosen to selectively release excitatory or inhibitory compounds (Figure 6.10). Alternatively, selective heating could provide the basis for multistage release of the same compound, prolonging the duration of release. In systems that depend directly upon nanoscale heating to actuate channel proteins, multiplexing could again provide a means for independent stimulation of different regions, and in this case would even allow the stimulation of different cell types in the same region or bidirectional stimulation of a single population if different kinds of temperature activated ion channels could be employed. Moreover, in the event that multiple therapies based on the heating of MNPs were employed in a single patient, magnetothermal multiplexing would provide a way to reduce or eliminate crosstalk.

For the purpose of assessing magnetothermal multiplexing for nanoscale heating applications using the scoring functions defined in Section 1.5, IPLP appears to be a more relevant metric than SLP, for reasons discussed in Section 1.5. Rather than IPLP, it would be ideal to compare expected temperature change at some well-defined point near the surface of an MNP. Perhaps further study of nanoscale heating will enable such comparisons to be made readily, though this could depend sufficiently on extrinsic conditions that IPLP may remain a reasonable proxy for surface heating. For nanoscale heating, efficiency, selectivity, and parity are

all important metrics to consider. Unlike the bulk heating case, parity cannot be achieved simply by adjusting concentration. Figure 2.10 showed that dynamic hysteresis models predict this should be possible.

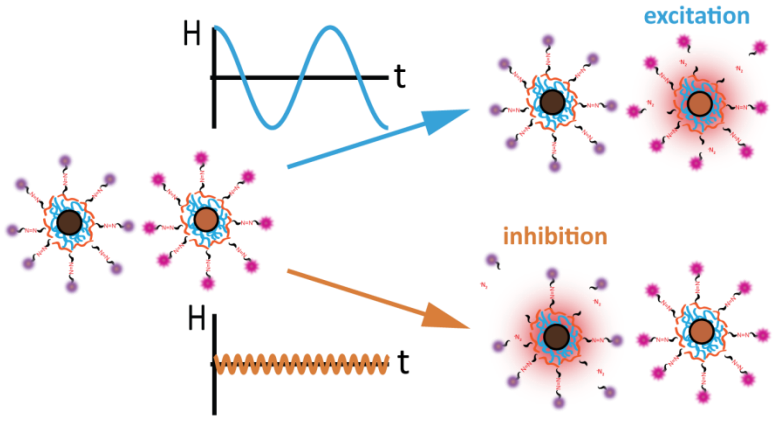

Figure 6.10 An idealized representation of magnetothermal multiplexing being used to selectively stimulate the release of compounds from two separate types of MNPs, e.g. for selective control of neural excitation or inhibition.

7 Conclusion and Key Lessons

This thesis has focused on the development of the concept of magnetothermal multiplexing, which was first anticipated theoretically and then investigated experimentally. It is has endeavored throughout to both elucidate the underlying physical principles that permit selective heating of MNPs, and to provide practical and straightforward guidance for empirically identifying suitable materials. The experimental challenge of constructing setups capable of supplying AMFs at various length scales was sufficiently central for these efforts to warrant analysis and discussion of their design principles. Several projects were summarized that investigated biomedical applications using heat dissipated by MNPs in AMFs to actuate biological and material responses. When considered individually, each of these topics explores appealing technological possibilities, and together they help provide a context and impetus for the development of magnetothermal multiplexing.

Key Lessons:

Optimization of loss power is subject to AMF constraints.

Studies on the heating of MNPs in AMFs have a predilection for claiming loss powers that are either high or the highest ever recorded. Unfortunately, the implied comparison with related literature is often specious because AMF conditions differ dramatically from study to study. This work adopted a field frequency product ($H_0 f$) as a rudimentary constraint, which played a central role in anticipating the possibility of magnetothermal multiplexing. Moving beyond the rudimentary $H_0 f$ product assumed in this thesis, more nuanced constraints might consider off-target heating in tissue or factors such as the relative expense of different AMF setups.

Quantitative attempts toward optimization could help advance materials design for these applications in a more systematic and effective way.

Linear response theory as a model for the heating of MNPs has a limited domain of validity.

As discussed in Chapter 2, linear response theory's domain of validity is limited to AMF amplitudes much lower than the anisotropy field H_k. The fact that linear response theory is mathematically identical to the Debye theory for dielectric losses in polar solvents draws attention to a crucial difference inherent to these systems: the moments of MNPs are large and their interaction with the applied field often cannot be neglected. All three of the improved models for hysteretic heat dissipation discussed in this thesis account for the barrier to magnetization reversal being lowered by the AMF and overcome through thermal fluctuation. As a result, they all predict square like hysteresis loops in some circumstances, a prediction that appears to be borne out experimentally.

Scaling up setups that produce AMFs is an underappreciated challenge that must be addressed if clinical therapies based on heating MNPs are to offer practical utility.

Despite the proliferation of studies on possible therapies that use MNPs in AMFs, the best example of an AMF setup scaled to human dimensions produces AMF conditions (100kHz and 18kA/m) that are far less aggressive than what is used in research.[80] Although design principles for scaling resonant tanks were presented here, the topic is deserving of further study and experimentation.

AC magnetometry is a superior experimental method for characterizing hysteresis and loss power as compared to AMF calorimetry.

In the experimental work described in this thesis, the task of calorimetry data collection frequently limited the rate of progress. Automated AC magnetometry could offer a compelling alternative method that is not only more rapid by orders of magnitude, but also provides higher quality data. For example, it could allow observations of hysteresis loop shapes and highly resolved SLE vs H_0 curves of the kind used in Section 4.7 for extrapolation of heating rates. In contrast to the setups shown in literature, an ideal AC magnetometry setup would leverage low power electromagnets to access high AMF amplitudes at readily adjustable resonant frequencies. These electromagnets by necessity have narrow gaps, suggesting the use of side by side spiral pickup coils, rather than end to end solenoidal pickup coils. If a multilayered printed circuit board with very fine traces could be used for such a magnetometer, with minimal physical construction steps, the setup could easily be made widely available and perhaps improve data collection practices in the field for measuring hysteretic heat dissipation by MNPs.

Methods to stimulate neurons with AMFs and MNPs, even if effective, will face significant barriers to widespread adoption.

As it currently stands, these methods tend to require transfection, which presents significant challenges for approval as a therapy for humans. Perhaps an approach based on release of neurotransmitters triggered by MNPs could circumvent this difficulty, but this would likely offer a limited number of stimulations before carriers become depleted. As an experimental tool for neuroscientists wishing to simply and precisely excite neurons in freely behaving animal models, the inherent difficulties of AMF generation in large volumes are likely to discourage adoption by

researchers other than those investigating the stimulation method itself. Compelling alternatives based on AMFs are rapidly emerging. For example, Draper Laboratories is currently developing highly miniaturized (<1mm^3), inductively powered neural stimulators. These can be easily selectively addressed because of their adjustable resonant response and the inductive coils that power them require watts rather than tens of kilowatts to generate a suitable AMF for the volume of an animal cage. Researching stimulation methods with MNPs is nevertheless worthwhile because the techniques and technologies investigated may translate into other therapies. For instance, the concept of magnetothermal multiplexing as presented in this thesis was initially investigated with the intent of providing multiple channels for neural stimulation, but as a broader materials concept could eventually be used in other technologies.

The phenomenon of nanoscale heating is both fundamentally interesting and technologically useful.

The peculiarity of nanoscale heating at the surface of MNPs, a topic motivated at length in Section 6.1, is not yet generally appreciated. This is perhaps best demonstrated by the fact that some of the studies that have yielded fascinating and compelling experimental evidence for the existence of nanoscale heating model their systems with bulk heat transport equations and constant temperature boundary conditions—a choice tantamount to assuming loss powers eight to ten log units larger than any ever observed.[12, 112] The existence of nanoscale heating in MNPs represents such a dramatic departure from seemingly well-motivated predictions that the topic begs for further fundamental study, either to explain the phenomenon or correct the experimental record.

Appendix A Details and Extensions of Magnetothermal Multiplexing Figures of Merit

In Section 1.5 of the main text, scoring functions were defined in order to quantify comparisons in a search for a set of two multiplexing MNPs. The concept of magnetothermal multiplexing encompasses two *or more* types of MNPs, so some explanation is needed on how these scoring functions might be extended to compare more than two types of MNPs. In practice, a function calculating efficiency might appear as follows:

$$efficiency = \frac{\mathrm{Max}\left(LP_{x,1}, LP_{x,2}\right) + \mathrm{Max}\left(LP_{y,1}, LP_{y,2}\right)}{2LP_{max}} \tag{A.1}$$

If the different MNP sets, x and y, heat most effectively in the same AMF, the condition in Equation 1.4 ensures that the selectivity will go to zero. Extending this form of comparison to a situation in which N types of multiplexing MNPs are desired is straightforward.

$$efficiency = \frac{\mathrm{Max}\left(LP_{x,1}, LP_{x,2}, \ldots LP_{x,N}\right) + \cdots \mathrm{Max}\left(LP_{z,1}, LP_{z,2}, \ldots LP_{z,N}\right)}{N\ LP_{max}} \tag{A.2}$$

A function for selectivity might be written as follows when two types of MNPs are desired:

$$selectivity = \begin{cases} 0 & \text{if } \dfrac{LP_{x,1} - LP_{x,2}}{LP_{y,1} - LP_{y,2}} > 0 \\ \mathrm{Min}\left[1 - \dfrac{4LP_{x,1}LP_{x,2}}{\left(LP_{x,1} + LP_{x,2}\right)^2}, 1 - \dfrac{4LP_{y,1}LP_{y,2}}{\left(LP_{y,1} + LP_{y,2}\right)^2}\right] & \text{if } \dfrac{LP_{x,1} - LP_{x,2}}{LP_{y,1} - LP_{y,2}} < 0 \end{cases} \tag{A.3}$$

This assumes that it is prudent to take the less selective of the two selectivity values as representative of the overall selectivity of the system. Perhaps in applications such as sequential release, the case could be made for a less stringent approach. Rather than a minimum, in such cases it may be more appropriate to take a maximum and assume that the most selective MNP would be responsible for initial release.

When seeking simultaneous selectivity in N MNP types in N AMF conditions, the most direct approach might be to first establish preferred AMF conditions for each MNP type. If any of the MNP types heats best at more than one of the AMF conditions under consideration, selectivity could be conditionally evaluated to zero. Selectivity could then be evaluated for each of the MNP types, comparing the favored AMF conditions against all other AMF conditions. For example if $N = 3$ and MNP type x is favored at AMF condition 1, then the selectivity score for x could be assessed as follows:

$$\mathrm{Min}\left[1 - \frac{4LP_{x,1}LP_{x,2}}{\left(LP_{x,1} + LP_{x,2}\right)^2}, 1 - \frac{4LP_{x,1}LP_{x,3}}{\left(LP_{x,1} + LP_{x,3}\right)^2}\right] \tag{A.4}$$

The overall score for selectivity of these choices in MNPs and AMF conditions could then simply be taken as the minimum of the selectivity for x, y, etc., depending on the particular application.

For applications based on nanoscale heating where parity is a significant consideration, a similar approach could be taken. The goal in that case is for comparable heating rates at the favored AMF conditions, and since favored conditions were already determined to evaluate selectivity, these can be used directly in evaluating parity. Once again, retaining the lowest parity value permits the most realistic assessment of the system. For example, consider a case when N=3, MNP x is favored at AMF 1, MNP y is favored at AMF 2, and MNP z is favored at AMF 3. The parity might be evaluated as follows:

$$\text{partiy} = \text{Min}\left\{\left[\frac{IPLP_{x,1}IPLP_{y,2}}{\left(\frac{IPLP_{x,1}+IPLP_{y,2}}{2}\right)^2}\right]^8, \left[\frac{IPLP_{y,2}IPLP_{z,3}}{\left(\frac{IPLP_{y,2}+IPLP_{z,3}}{2}\right)^2}\right]^8, \left[\frac{IPLP_{x,1}IPLP_{z,3}}{\left(\frac{IPLP_{x,1}+IPLP_{z,3}}{2}\right)^2}\right]^8\right\} \quad \text{A.5}$$

The discussion thus far has outlined an approach intended to ascertain suitable AMF conditions for magnetothermal multiplexing with a given set of MNPs. A more likely scenario is that, in addition to unknown optimal AMF conditions, a palate of materials would need to be evaluated as possible candidates. The general procedure for comparing M candidate MNP sets to find N that multiplex effectively is simply to separately consider the $\binom{M}{N}$ possibilities for different combinations of MNPs. For instance, Figure 5.4(c) was developed based on considering $\binom{4}{2} = 6$ separate combinations of MNP types, where each combination involved an algorithmic search of accessible conditions to attempt to maximize the most relevant figures of merit: selectivity and efficiency.

Appendix B Subtleties of Anisotropy

In MNPs, anisotropy can be understood in its most general sense as the existence of certain preferred orientations of the magnetic moment, separated from one another by energy barriers. This concept, accompanied by thermal fluctuations that can eventually surmount such barriers to reorient the magnetization, is a central feature of all of the models explored in Chapter 2. Attempting to correlate these models with experimental observations relies upon estimating or inferring reasonable values for anisotropy. Because anisotropy is influenced by numerous characteristics of MNPs, and inherent variability is present not only between different synthesized batches of MNPs but also within a single population, a distribution of anisotropies should be anticipated.

To some extent, the models in Chapter 2 gloss over the full complexity of anisotropy by assuming a uniaxial form. This assumption is convenient because of the resulting azimuthal symmetry, especially in the case of easy aligned MNPs, where the interaction of the moment with the field has the same symmetry. In real MNPs, anisotropy can take nonuniaxial forms, and some distribution of physical orientations should be expected with neither fully aligned easy axes, nor completely random alignment. Attempting to capture all of these complexities could perhaps improve the predictive accuracy of the models, but this would carry a substantial cost. No model is perfect; ultimately their purpose is to offer intuition and understanding. This is the view motivating the representation of the σ-ξ space in Figure 2.5, which depicts the results of dynamic hysteresis with a broad view of normalized energy scales. The remainder of this appendix will address several important nuances concerning the anisotropy of MNPs.

1. Leading order coefficients for uniaxial and cubic anisotropy are not interchangeable for estimating the value of the barriers separating easy axes.

There is a tendency in literature to conflate the first order coefficient of cubic magnetocrystalline anisotropy with the first order coefficient of uniaxial anisotropy. Doing so ignores the basic functional forms of these different anisotropies. For the uniaxial case, the first order dependence is as follows:

$$U(\theta,\phi) \approx K_{u,1} \sin^2\theta \qquad \text{B.1}$$

$K_{u,1}$ denotes the first order uniaxial anisotropy coefficient. A polar plot of this function is shown in Figure B.1(a). The first order cubic case can be similarly expressed in terms of θ and ϕ

$$U(\theta,\phi) \approx K_{c,1} \sin^2\theta \,(\cos^2\phi \sin^2\phi \sin^2\theta + \cos^2\theta) \qquad \text{B.2}$$

Here, $K_{c,1}$ is the first order cubic anisotropy coefficient. If $K_{c,1} > 0$, there are six easy axes, as shown in Figure B.1(b). If $K_{c,1} < 0$, there are eight easy axes, as shown in Figure B.1(c). Clearly, the sign of $K_{c,1}$ is a significant consideration. A comparison of Equations B.1 and B.2 indicates that $|U(\theta,\phi)|$ in the cubic case will be less than or equal to $|U(\theta,\phi)|$ in the uniaxial case for all θ and ϕ if $K_{u,1}$=$K_{c,1}$. This is significant because it also impacts the magnitude of the barriers separating easy axes, as shown in Figure B.1(d).

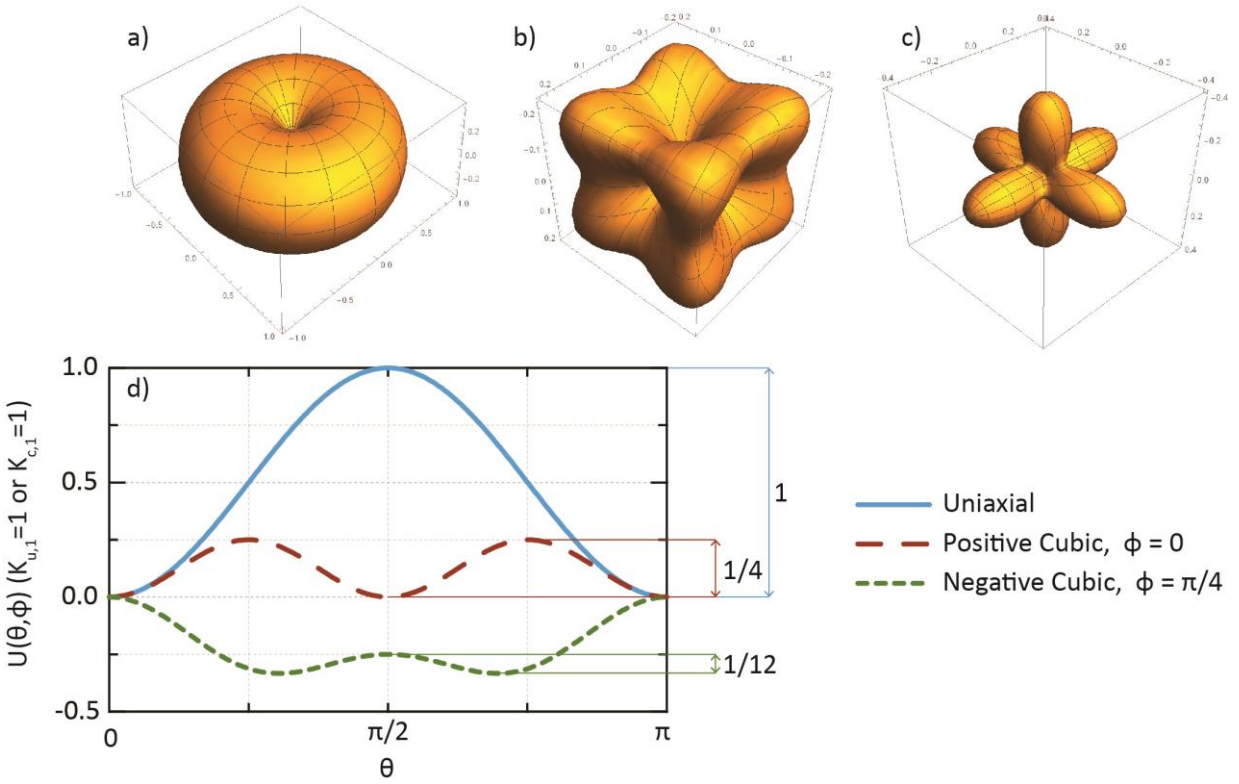

Figure B.1 Polar plots are shown for the first order terms of (a) positive uniaxial anisotropy, (b) positive cubic anisotropy, and (c) negative cubic anisotropy. A constant has been added to the expression for negative cubic anisotropy to allow for a polar plot, which cannot depict negative values. (d) The minimal energy paths connecting easy axes are shown for each case, assuming a coefficient of 1.

2. The overall anisotropy of an MNP often results from contributions other than the magnetocrystalline component.

In literature that models the heating of MNPs, it is frequently assumed that the anisotropy of MNPs originates primarily from magnetocrystalline anisotropy. This is an approximation that may be warranted in some cases, but not nearly as often as it is made. For instance, Usov et al. have shown theoretically that for ellipsoidal MNPs comprised of materials such as metallic iron, metallic cobalt, and magnetite, only slight deviations from spherical shape lead to shape anisotropy dominating relaxation times.[60] Experimental comparisons between faceted and round MNPs of comparable volume have suggested the role of surface anisotropy, which can become especially pronounced in cases of very small MNPs[55] or where other contributions are weak.[144] Many synthesis methods produce MNPs that are strained,[90] and for magnetostrictive materials, this may also contribute to anisotropy, as has been shown repeatedly in thin films.[145]

If the energy scale of interaction between MNPs is comparable to or larger than the intrinsic anisotropy of isolated MNPs, then it may instead dominate the response of magnetization to the field.

3. Deviations from a spherical shape do not necessarily contribute to shape anisotropy.

Some additional explanation of shape anisotropy is required to illustrate this point. One formulation of magnetostatics envisions fictitious magnetic monopoles bound to the surfaces of magnetized objects. In free space outside the magnetized body, these monopoles produce a field with the same direction as M, but there is also a resulting H field inside the object with the opposite sign. This internal field is sometimes called the demagnetizing field $\overrightarrow{H_d}$, a name that anticipates the nature of the interaction between this field and the magnetized volume.

$$U \propto -\int \vec{M} \cdot \overrightarrow{H_d} dV \geq 0 \qquad \text{B.3}$$

The sign indicates an energy penalty associated with magnetizing an object. The direction and magnitude of $\overrightarrow{H_d}$ depends on the direction of $\vec{M}$. This can be understood intuitively by envisioning the distance between the fictitious monopoles at the surface of a magnetized object changing for different orientations of $\vec{M}$, particularly in a disc or a needle. A potential energy difference that depends on angular coordinates leads to a torque.

One convenient property of ellipsoids is that $\overrightarrow{H_d}$ is uniform. The demagnetizing tensor $\overleftrightarrow{N}$ describes the directional dependence of the energy penalty. With appropriate selection of coordinate axes (principal axes), its form is diagonalized, and its action reduces to

$$U = \frac{{M_0}^2 \mu_0}{2} V\left(N_x {m_x}^2 + N_y {m_y}^2 + N_z {m_z}^2\right) \qquad \text{B.4}$$

Where $\vec{M} = M_0 \vec{m}$ and the demagnetizing tensor is

$$\overleftrightarrow{N} = \begin{pmatrix} N_x & 0 & 0 \\ 0 & N_y & 0 \\ 0 & 0 & N_z \end{pmatrix} \qquad \text{B.5}$$

Note that $N_x + N_y + N_z = 1$ and these values have to appropriately correspond to the geometric symmetry of the shape. The Brown-Morrish theorem asserts the existence of an "equivalent ellipsoid" for every magnetized shape.[146] This does not imply that $\overrightarrow{H_d}$ is uniform inside every shape, but rather that when energy is integrated over the entire volume, an appropriate coordinate system can be selected to diagonalize the demagnetization tensor. A corresponding ellipsoid would have produced the same result, though actually finding this ellipsoid can be nontrivial.

For instance, the equivalent ellipsoid of a circular disc would unsurprisingly be a highly oblate spheroid. The situation can be somewhat less obvious in cases of cubes or faceted shapes, which are commonly encountered in MNPs and exhibit discreet rotational symmetry. Surprisingly, these shapes are not expected to exhibit shape anisotropy and thus their corresponding equivalent ellipsoids are spheres.[147] Though the form of $\overrightarrow{H_d}$ would change significantly with orientation in many of these shapes, changing the energy density in the magnetized object, the total integrated energy is constant.

4. Interactions between particles can plausibly have an effect similar to adding a term to the anisotropy.

Suppose that there are two MNPs separated by a distance d from one another, and that the reorientation of their moments and the period of the applied AMF are sufficiently fast compared to translation of the MNPs through solution that taking a "snapshot" view is appropriate. Their energy of interaction could play a role in influencing the orientation of the moments. Here, a simple case can be considered where the moments of the two particles are equal and aligned. (Figure B.2).

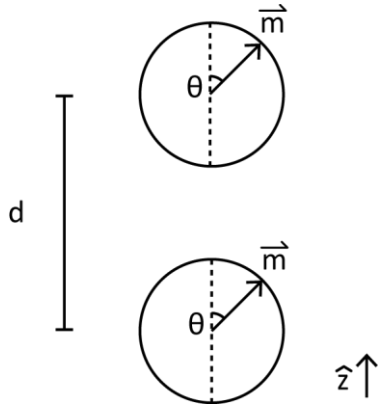

Figure B.2 A sketch of the geometry for interacting identical MNPs separated by a distance d and constrained to orient together is shown.

The resulting energy of interaction U that results is as follows

$$U = \frac{-\mu_0 m^2}{4\pi d^3}(3\cos^2\theta - 1) \qquad \text{B.6}$$

A constant can be added to an expression for energy without influencing the forces or torques that that it implies. It is revealing to add the following constant to Equation B.6:

$$U + \frac{2\mu_0 m^2}{4\pi d^3} = \frac{3\mu_0 m^2}{4\pi d^3}\sin^2\theta \qquad \text{B.7}$$

This shows that these simple assumptions have produced an interaction with a functional form identical to positive uniaxial anisotropy. One intuitive way to view this is as a form of shape anisotropy of a cluster, such that clusters of many MNPs could exhibit different dependences. Sweeping conclusions should not be drawn from this highly simplified picture of MNP interaction. For instance, it is easy to imagine a long chain of interacting MNPs exhibiting long range order and undergoing reversal processes analogous to nucleation and growth of opposing domains under the influence of an applied field. This simple model merely serves to illustrate dependencies on m^2 and d^{-3}, which helps to motivate the basis of more involved modeling of interparticle interactions such as Usov et al,[72] and to demonstrate that in some cases these interactions can plausibly contribute to anisotropy.

Appendix C Thermodynamic Reasoning for Hysteresis

Starting with the first law of thermodynamics, where U is energy, Q is heat and W is work, heat exchange will be neglected in order to consider just the magnetic work being done on the system, W_m.

$$dU = \delta Q + \delta W \quad \text{C.1}$$

$$dU = dW_m = HdB \quad \text{C.2}$$

Substituting $\mu_0(dH - dM)$ for dB, and integrating over a full cycle of the alternating field,

$$\Delta U = \mu_0 \oint HdH - \mu_0 \oint HdM \quad \text{C.3}$$

The first term, which describes energy reversibly stored in the magnetic field itself, goes to zero because H varies cyclically. The second term can be rewritten using integration by parts,

$$\oint HdM = MH - \oint MdH \quad \text{C.4}$$

The first term on the right-hand side will go to zero for steady state hysteresis, which by definition produces closed loops. This can be interpreted as the energy stored reversibly by magnetizing an object. Substituting the nonvanishing part into Equation C.3,

$$\Delta U = -\mu_0 \oint HdM = \mu_0 \oint MdH \quad \text{C.5}$$

Both of these integrals are representations of the area of a hysteresis loop. The area of such loops may be interpreted as a graphical representation of loss energy per cycle of the field.

Appendix D Details of Linear Response Theory

Linear response theory finds loss powers by integrating over elliptical hysteresis loops described by complex valued susceptibility. As explained in the main text, complex values can be interpreted as a mathematical tool for describing a phase shift.

$$M = \tilde{\chi} H_0 e^{i\omega t} = |\tilde{\chi}| H_0 e^{i(\omega t + \delta)} \qquad \text{D.1 (2.5)}$$

The relationships between complex values and their real and imaginary components can be understood straightforwardly with the Argand plane, shown in Figure D.1.

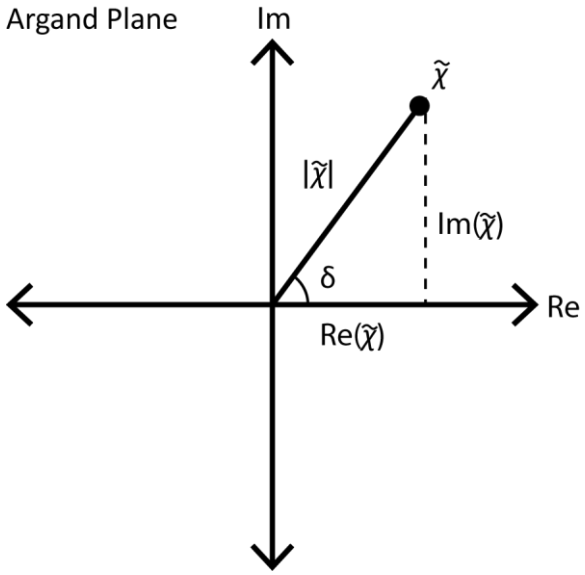

Figure D.1 The Argand plane is used to represent all possible complex values analogously to the way a real number line represents all possible real values. The abscissa of the Argand plane is the real number line and the ordinate is the imaginary number line. Any complex value, such as $\tilde{\chi}$, can be represented by a point in the plane. To describe this point, one can equivalently specify either an angle δ and distance $|\tilde{\chi}|$ together, or the projections along the real and imaginary axes, $\mathrm{Re}(\tilde{\chi})$ and $\mathrm{Im}(\tilde{\chi})$.

Complex periodic functions in time are convenient because they allow for simultaneous consideration of sine and cosine functions. This is because both the real and imaginary parts implied in Equation D.1 must be separately equal. Introducing a phase shift to linear susceptibility describes elliptical hysteresis loops, and to show this mathematically, it is useful to specifically consider either the real or imaginary part of Equation D.1. Take for instance the parametric equations represented by the real component.

$$H(t) = |\tilde{\chi}| H_0 \cos(\omega t) \qquad \text{D.2}$$

$$M(t) = |\tilde{\chi}| H_0 \cos(\omega t + \delta) \qquad \text{D.3}$$

Describing the response of a material within the framework of complex susceptibility allows $|\tilde{\chi}|$ and δ to be altered in the above parametric equations, but the family of loops represented are ellipses, as illustrated in Figure 2.2(b).

Loss energy per cycle of the field can be found by integrating over a generalized loop, as shown in Equation C.5, and in this case analytical integration is possible.

$$dH = -H_0\omega \sin(\omega t)dt \tag{D.4}$$

$$M = |\tilde{\chi}|H_0 \cos(\omega t + \delta) \tag{D.5}$$

$$\Delta U = \mu_0 \oint M dH = -|\tilde{\chi}|{H_0}^2 \int_0^{\frac{2\pi}{\omega}} \cos(\omega t + \delta)\omega \sin(\omega t)dt \tag{D.6}$$

A trigonometric identity readily provable using Euler's rule allows the phase shifted cosine term to be split into an in phase and out of phase component.

$$\Delta U = -|\tilde{\chi}|{H_0}^2 \int_0^{\frac{2\pi}{\omega}} [\cos(\omega t)\cos(\delta) - \sin(\omega t)\sin(\delta)]\omega \sin(\omega t)dt \tag{D.7}$$

Referring to the Argand plane diagram in Figure D.1, one can see geometrically how the above expression can be recast in terms of the real and imaginary components of the susceptibility. These terms represent the in phase (storage, $\mathrm{Re}(\tilde{\chi})$) and out of phase (loss, $\mathrm{Im}(\tilde{\chi})$) component, respectively.

$$\Delta U = -{H_0}^2 \int_0^{\frac{2\pi}{\omega}} [\mathrm{Re}(\tilde{\chi})\cos(\omega t) - \mathrm{Im}(\tilde{\chi})\sin(\omega t)]\omega \sin(\omega t)dt \tag{D.8}$$

As expected, the storage term vanishes from the integration.

$$\Delta U = {H_0}^2 \int_0^{\frac{2\pi}{\omega}} \mathrm{Im}(\tilde{\chi})\omega \sin^2(\omega t)dt = \pi {H_0}^2 \mathrm{Im}(\tilde{\chi}) \tag{D.9}$$

To find the specific loss power, the susceptibility is put in terms of mass of metal ions per unit volume and ΔU is multiplied by the frequency, $\frac{\omega}{2\pi}$.

$$\mathrm{SLP} = \tfrac{1}{2}\mu_0\chi_0{H_0}^2\omega\left(\frac{\omega\tau}{1+(\omega\tau)^2}\right) \tag{D.10}$$

In practice, the Langevin function is often incorporated into the expression for χ_0.

$$\chi_0 \approx \frac{M_s\phi\, L(\xi)}{H_0} \tag{D.11}$$

Where

$$L(\xi) = \coth \xi - \frac{1}{\xi} \quad \text{D.12}$$

Substituting into Equation D.10,

$$\text{SLP} = \tfrac{1}{2}\mu_0 \phi M_s H_0 L(\xi) \omega \frac{\omega\tau}{1 + (\omega\tau)^2} \quad \text{D.13}$$

The intent of this "chord" approximation is to bound the magnetization so that loops are not predicted in which $M > M_s$. It should be emphasized that the assumed equilibrium behavior is still linear; now the susceptibility is simply assumed by drawing a line from the origin to a point on the Langevin curve. In limit of low ξ (low H_0), the SLP will be proportional to ${H_0}^2$. As $L(\xi)$ saturates, SLP will be proportional to H_0, and this is the case most relevant to the AMF conditions and MNP sizes discussed in this work. The prediction of linear response theory that SLP should grow linearly without bound in H_0 can be seen as resulting from its inability to restrict the coercive field H_c in the same way it bounds M.

Appendix E Details of Dynamic Hysteresis for Easy Aligned Uniaxial MNPs

Section 2.4 of the main text offers context and interpretation for the results of dynamic hysteresis models, and this appendix is intended to provide a more detailed account of the reasoning behind it. Carrey et al.[68] offer additional details on topics such as equilibrium magnetization curves including anisotropy and random orientation and much of what follows is based on the model they describe.

For easy aligned MNPs with uniaxial anisotropy, the energy landscape experienced by individual MNP moments is azimuthally symmetric and can be expressed as follows.

$$\frac{U(\theta,\phi)}{k_B T} = \sigma \sin^2\theta - \xi\cos\theta \qquad \text{E.1 (2.5)}$$

Note that $\sigma \equiv \frac{K_{eff}V_m}{k_B T}$ and $\xi \equiv \frac{\mu_0 H M_s V_m}{k_B T}$, unitless quantities describing the magnitude of the anisotropy energy barrier and Zeeman energy normalized to the energy scale of ambient thermal fluctuations. The moments can be considered to exist in populations that statistically inhabit the energy minima (a so called "macrospin approximation"), where P_A and P_B are the proportion of the total population inhabiting minimum A and minimum B respectively. (See Figure 2.3 or Figure E.1). Let ν_A be the probability of escape from minimum A per unit time, and ν_B be the probability of escape from minimum B per unit time. The system of coupled differential equations that describes how P_A and P_B evolve in time can be written as follows

$$\frac{dP_A}{dt} = -\nu_A P_A + \nu_B P_B \qquad \text{E.2}$$

$$\frac{dP_B}{dt} = \nu_A P_A - \nu_B P_B \qquad \text{E.3}$$

Note that the sum of these two equations vanishes on the right-hand side. This indicates that the sum $P_A + P_B$ is conserved, as it must be.

$$\frac{d}{dt}(P_A + P_B) = \frac{dP_A}{dt} + \frac{dP_B}{dt} = -\nu_A P_A + \nu_B P_B + \nu_A P_A - \nu_B P_B = 0 \qquad \text{E.4}$$

The main text provided a justification for expressing the instantaneous escape rates as follows

$$\nu_A = \nu_0 e^{\frac{-U_A(\sigma,\xi)}{k_B T}} \qquad \text{E.5}$$

U_A is the effective energy barrier for moments escaping from minimum A into minimum B, and conversely U_B is the effective energy barrier for moments escaping from minimum B to minimum A. θ_{max} is the orientation of the moment at which energy is maximized. (Figure E.1).

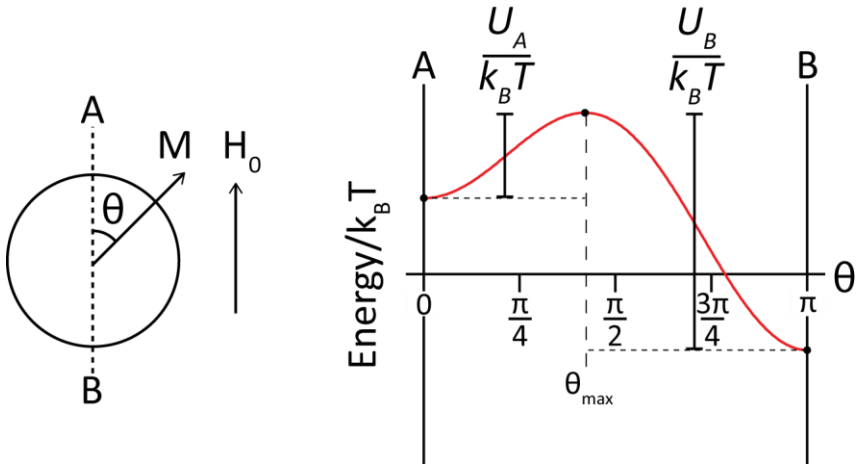

Figure E.1 The energy of an easy aligned MNP with uniaxial anisotropy is shown, along with the definitions of U_A, U_B, and θ_{max}.

With the application of an AMF, U_A and U_B will vary periodically in time. To describe this mathematically, the barriers can be considered functions of σ and ξ. At some value of ξ, the barrier to reversal will vanish, and this can be investigated by taking a derivative of U with respect to θ and considering the conditions under which the maximum $U(\theta_{max})$ corresponding to the barrier will exist.

$$\frac{1}{k_B T}\frac{dU}{d\theta} = \sin\theta\,(2\sigma\cos\theta + \xi) = 0 \qquad \text{E.6}$$

The $\sin\theta$ prefactor ensures that this equation is always satisfied for $\theta = 0$ and $\theta = \pi$, where stationary extrema occur. The expression in parenthesis is associated with maximum that occurs at the angle θ_{max}. Setting this expression to zero and solving,

$$\theta_{max} = \arccos\frac{\xi}{2\sigma} \qquad \text{E.7}$$

Note that the domain of the arccosine function is bounded between -1 and 1. This implies that when $\left|\frac{\xi}{2\sigma}\right|$ exceeds 1, the barrier to reversal vanishes. This is a familiar result from Stoner Wholfarth theory, in which very low temperature reversal takes place at the applied field where the barrier to reversal vanishes, the "anisotropy field," H_k. The quantity can serve to normalize applied fields in generalized hysteresis loops in a physically meaningful way, as depicted in Figure 2.5. In magnetic nanoparticle systems at the physiological temperatures relevant to biomedical applications, the coercive field H_c of hysteresis loops should be expected to always be less than H_k.

$$\frac{\xi}{2\sigma} = \frac{\mu_0 H M_s}{2K_{eff}} \equiv \frac{H}{H_k} \qquad \text{E.8}$$

For the purpose of finding accurate expressions for the energy barriers determining escape rates, it should merely be noted that the effective barrier should be 0 after H_k is exceeded in the

direction favoring escape and 2ξ in the other direction. Equation E.7 can be substituted into Equation E.1 to find intermediate values.

$$\frac{U_A}{k_B T} = U(\theta_{max}) - U(0) = \sigma(1 - \cos^2 \theta_{max}) - \xi \cos \theta_{max} - \xi$$
$$\frac{U_A}{k_B T} = \sigma + \frac{\xi^2}{4\sigma} - \xi \qquad \text{E.9}$$

The overall function for U_A can either be defined piecewise or by using Heaviside step functions, $H_\theta(x)$.

$$\frac{U_A(\sigma, \xi)}{k_B T} = \begin{cases} 2\xi, & \xi \leq -2\sigma \\ \sigma + \dfrac{\xi^2}{4\sigma} - \xi, & |\xi| \leq 2\sigma \\ 0, & \xi \geq 2\sigma \end{cases} \qquad \text{E.10}$$

Equivalently,

$$\frac{U_A(\sigma, \xi)}{k_B T} = \left(\sigma + \frac{\xi^2}{4\sigma} - \xi\right)[1 - H_\theta(\xi - 2\sigma)] - \left(\sigma + \frac{\xi^2}{4\sigma} + \xi\right) H_\theta(-\xi - 2\sigma) \qquad \text{E.11}$$

The energy barrier to escape in the opposite direction $\frac{U_B(\sigma,\xi)}{k_B T}$ can be found either by applying the same logic to the other easy axis or by realizing that the barrier to reversal ought to vary antisymmetrically with respect to the sign of the applied field. I.e.,

$$U_B(\sigma, \xi) = U_A(\sigma, -\xi) \qquad \text{E.12}$$

Figure E.2 shows a these barriers and the resulting instantaneous escape rates vary with ξ for the case of $\sigma = 10$. Notably, the escape rate can potentially vary by many orders of magnitude during a single cycle of the AMF.

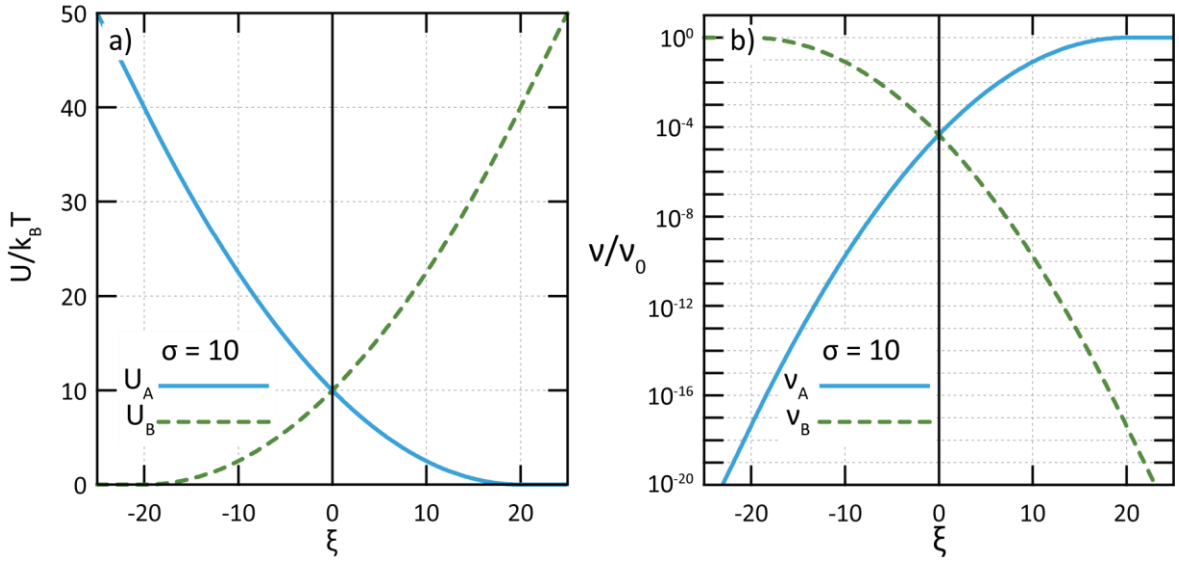

Figure E.2 (a) As an illustrative example, the magnitude of the energy barriers U_A and U_B are plotted as a function of ξ (which is proportional to H) according to Equation E.11 for the case of $\sigma = 10$. (b) The corresponding escape rates over the barrier, normalized to the attempt rate are shown for the same case of $\sigma = 10$.

With expressions for $U_A(\sigma, \xi)$ and $U_B(\sigma, \xi)$, there is now sufficient information to numerically solve the system of differential equations E.2 and E.3. ξ assumes a form that oscillates in time,

$$\xi = \xi_0 \cos \omega t \qquad \text{E.13}$$

The time dependent form of Equation E.11 can be substituted into E.5, which can be substituted into E.2 and E.3, and the system can be solved numerically to find $P_A(t)$and $P_B(t)$. In the main text, the macrospin approximation was used to relate these populations back to the magnetization, however a Boltzmann distribution of moment orientations should be expected in the minima to be consistent with model's assumptions about the escape rate. A small refinement can help account for this thermal spreading.

$$\frac{M}{M_s} = C_A P_A + C_B P_B \qquad \text{E.14}$$

Here, C_A and C_B are functions that account for thermal spreading by approximating the total energy function with a second order Taylor series expansion about the extrema at $\theta = 0, \pi$ (Figure E.3)

$$C_A = \frac{\int_0^{\frac{\pi}{2}} \sin\theta \cos\theta \exp\left[\frac{-(\xi + 2\sigma)}{2}\theta^2 + \xi\right] d\theta}{\int_0^{\frac{\pi}{2}} \sin\theta \exp\left[\frac{-(\xi + 2\sigma)}{2}\theta^2 + \xi\right] d\theta} \qquad \text{E.15}$$

$$C_B = \frac{\int_{\frac{\pi}{2}}^{\pi} \sin\theta \cos\theta \exp\left[\frac{(\xi - 2\sigma)}{2}(\theta - \pi)^2 - \xi\right] d\theta}{\int_{\frac{\pi}{2}}^{\pi} \sin\theta \exp\left[\frac{(\xi - 2\sigma)}{2}(\theta - \pi)^2 - \xi\right] d\theta} \qquad \text{E.16}$$

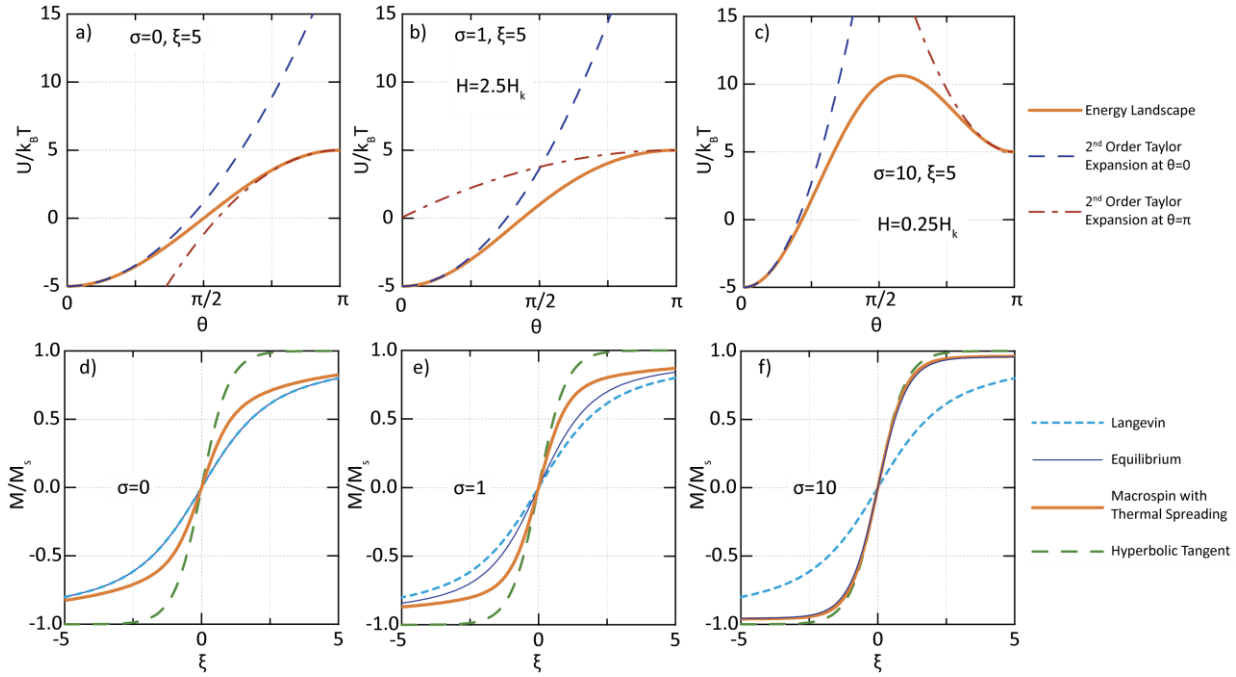

Figure E.3 (a), (b), and (c) show the uniaxial easy aligned energy landscape described by Equation E.1 for the values of σ and ξ shown, along with second order Taylor series centered at the stationary extrema at $\theta = 0, \pi$. These expansions are used to determine coefficients for thermal spreading in Equations E.16 and E.17. (d), (e), and (f) show equilibrium magnetization functions for the σ values in the panels above. The equilibrium magnetization as determined by Equation E.17 is shown along with the result of applying thermal spreading to an equilibrium distribution of macrospins. Bounds are provided in the form of the Langevin function for classical moments without anisotropy, and the hyperbolic tangent function for "macrospins" which can only assume the values $\theta = 0$ or $\theta = \pi$.

Note that a macrospin approximation combined with thermal spreading does not exactly reproduce a treatment of the full energy landscape at equilibrium, which would be given by a numerical evaluation of the following expression.

$$M(\sigma, \xi) = \frac{\int_0^{\pi} \sin\theta \cos\theta \exp[-\sigma \sin^2\theta + \xi \cos\theta]\, d\theta}{\int_0^{\pi} \sin\theta \exp[-\sigma \sin^2\theta + \xi \cos\theta]\, d\theta} \qquad \text{E.17}$$

The macrospin approximation without spreading results in the hyperbolic tangent function just as it would for a quantum mechanical treatment for which the available states are quantized. The hyperbolic tangent predicts a more rapid approach to saturation than the Langevin function or an equilibrium function based on the entire energy landscape (Figure E.3). Incorporating thermal

spreading in E.14 partially accounts for the difference at low σ values and agrees well with the more rigorous equilibrium landscape as σ becomes large (Figure E.3). In some sense, thermal spreading is probably more appropriate as a form of local equilibrium justifiable when populations of moments within the wells equilibrate more rapidly than they transition between them. In practice, the effect on the shape and area of hysteresis loops is small.

With a framework in place to determine M/M_s as a function of time, and a form assumed for ξ as a function of time, it is now possible to parametrically define hysteresis loops. These graphical representations are intuitive and instructional, and are worth examining to make sure that they have symmetries that make them physically plausible. In streamlined code, it is often the goal to simply quantify expected heat dissipation and to do that it is necessary to determine the area of a hysteresis loop, A.

$$A = \oint \frac{M(t)}{M_s} \frac{d\xi(t)}{dt} dt \tag{E.18}$$

This area can be interpreted as the individual particle loss energy per cycle of the field, normalized to the ambient thermal energy. To see this, consider the units of area of a M/M_s vs ξ loop:

$$A \Longrightarrow \frac{M}{M_s}\xi = \frac{\mu_0 H M V_m}{k_B T} \tag{E.19}$$

$\mu_0 HM$ is a volumetric energy density recognizable from macroscopic hysteresis loops, V_m is the magnetized volume of an MNP, and $k_B T$ is the energy scale of ambient thermal fluctuations. Clearly, the loop area A corresponds to the unitless loss energy of a single MNP normalized to thermal fluctuations, analogous to the definitions in Equations 2.13 or 2.14. Thus,

$$IPLP = Ak_B Tf \tag{E.20}$$

And

$$SLP = \frac{Ak_B Tf}{V\rho_m} \tag{E.21}$$

The analysis can be extended a bit further by considering the limiting case of maximal area. Note that this limit corresponds to the Stoner Wohlfarth curve at zero temperature, which has an area that can be expressed compactly in terms of σ. (Figure E.4)

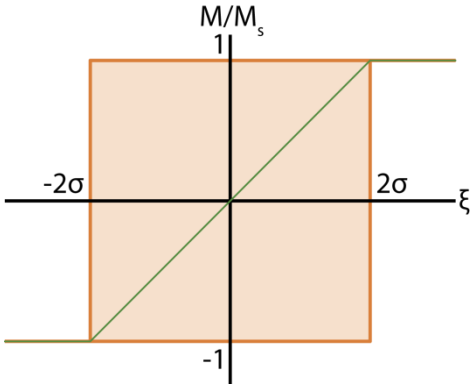

Figure E.4 A Stoner Wohlfarth zero temperature hysteresis loop is shown for the easy aligned and hard aligned uniaxial cases in terms of M/M_s versus ξ. Equation E.8 indicates that $\xi = 2\sigma$ when $H = H_k$. This produces a square loop with area 8σ.

Taking 8σ as an upper bound for A, and applying it to Equations E.20 and E.21, it can be asserted that

$$IPLP \leq 8\sigma k_B T f \qquad \text{E.22}$$

And,

$$SLP \leq \frac{8\sigma k_B T f}{V \rho_m} \qquad \text{E.23}$$

Substituting the definition of σ into Equation E.23 results in cancellation that shows SLP is bounded by K_{eff}

$$SLP \leq \frac{8K_{eff} f}{\rho_m} \qquad \text{E.24}$$

This result helps to justify why it is better to increase K_{eff} in cases when higher H_k is desired, rather than decreasing M_s, as suggested in Section 4.1.

Appendix F Details of Landau-Lifshitz-Gilbert Equation with Thermal Noise

This appendix explains details about modeling hysteresis with the LLG equation by incorporating stochastic fluctuations. The simulation shown in Figure 2.6 is based on a project completed for a course, 18.086, for which a simple 4th order Runge-Kutta solver was written to propagate the system forward in time. The information provided here emphasizes physical background rather than the details of the numerical treatment.

Equation 2.20 can be rewritten by dividing throughout by M_s in order to re-express it in terms of the unit magnetization vector $\vec{\alpha}$

$$\frac{d\vec{\alpha}}{dt} = -\gamma_1 \vec{\alpha} \times \left(\vec{H}_{eff} + \vec{H}_{th}\right) - \kappa\gamma_1 \vec{\alpha} \times \left[\vec{\alpha} \times \left(\vec{H}_{eff} + \vec{H}_{th}\right)\right] \quad \text{F.1}$$

Where, as before $\gamma_1 \equiv \frac{\gamma}{1+\kappa}$ and

$$\gamma = \frac{\mu_0 g|e|}{2m_e} \quad \text{F.2}$$

Here, e is the elementary charge, g is the Landé g factor, m_e is the electron mass, and μ_0 is the permeability of free space. The effective field is defined to supply a torque consistent with the overall energy landscape that the MNP experiences.

$$\vec{H}_{eff} = -\frac{1}{\mu_0 M_s V_m}\frac{\partial U}{\partial \vec{\alpha}} \quad \text{F.3}$$

This energy U, for a uniaxial MNP, can be written as in Equation 2.15, but in this case, it is helpful to notate the angular dependence in a form that aids in differentiating with respect to $\vec{\alpha}$.

$$U = -\mu_0 M_s V_m\left[\vec{\alpha} \cdot \vec{H}_{ap}(t)\right] + K_{eff} V_m (\vec{\alpha} \times \hat{z})^2 \quad \text{F.4}$$

Using this expression for U to calculate $\vec{H}_{eff}$, the Zeeman energy term reduces to a simple added contribution $\vec{H}_{ap}(t)$, as anticipated by the form given to Equation F.3. The assumption of uniaxial anisotropy results in a simple form for the second term incorporated into $\vec{H}_{eff}$. Its prefactor reduces to H_k as defined in Section 2.4 and Appendix E:

$$\vec{H}_{eff} = \vec{H}_{ap}(t) - \frac{2K_{eff}}{\mu_0 M_s}\begin{pmatrix}\alpha_x\\ \alpha_y\\ 0\end{pmatrix} = \vec{H}_{ap}(t) - H_k\begin{pmatrix}\alpha_x\\ \alpha_y\\ 0\end{pmatrix} \quad \text{F.5}$$

Had a nonuniaxial anisotropy instead been considered, $\vec{H}_{eff}$ would have been more difficult to write, but would have had a similar underlying influence.

The thermal field $\vec{H}_{th}$ fluctuates stochastically, but with well-defined statistical properties. The first of these properties states that the time average of the component in each direction must be zero.

$$\langle H_{th,i}(t)\rangle = 0 \qquad \text{F.6}$$

The time averaged product of any two components of the field is taken to be the following

$$\langle H_{th,i}(t)H_{th,j}(t')\rangle = \frac{2k_BT\kappa}{M_sV_m\gamma}\delta_{i,j}\delta(t-t') \qquad \text{F.7}$$

The Kroneker delta $\delta_{i,j}$ simply indicates that for different components (i.e. when $i \neq j$), the time average of the product should vanish. If this were not the case, the components of $\vec{H}_{th}$ would be spatially correlated. The Dirac delta $\delta(t-t')$ with reference to an arbitrary future or past time t' similarly indicates that $\vec{H}_{th}$ is uncorrelated in time.

For the purpose of numerical propagation, it was helpful to recast equation F.1 in units more natural to the timescale of precession than seconds. One such possible choice is to divide Equation F.1 throughout by γH_0 and define the units of time such that $\gamma\mu_0 H_0 = 1$.

$$\frac{d\alpha}{dt_P} = \frac{2\pi}{1+\kappa}\left\{\vec{\alpha}\times\frac{(\vec{H}_{eff}+\vec{H}_{th})}{H_0} + \kappa\vec{\alpha}\times\left[\frac{\vec{\alpha}\times(\vec{H}_{eff}+\vec{H}_{th})}{H_0}\right]\right\} \qquad \text{F.8}$$

The thermal field was generated by calling function that generates pseudorandom values with a Gaussian distribution, $N[\mu,\sigma]$, where μ is the mean and σ is the standard deviation.

$$\vec{H}_{th} = H_{th0} * N[0,1] \qquad \text{F.9}$$

Where H_{th0} comes from Equation F.7, but of necessity must also depend on the timestep in its normalized units indicated above.[148]

$$H_{th0} = \sqrt{\frac{2k_BT\kappa}{M_sV_m\gamma}} * \sqrt{\frac{\gamma\mu_0H_0\Delta\mathrm{t}}{2\pi}} \rightarrow H_{th0} = \sqrt{\frac{2k_BT\kappa}{M_sV_m\gamma}} * \sqrt{\frac{\Delta\mathrm{t}}{2\pi}} \qquad \text{F.10}$$

Appendix G Differing Predictions for the Feasibility of Magnetothermal Multiplexing

It is reasonable to question what is truly gained by adopting models such as dynamic hysteresis in place of linear response theory, because the decision comes at the expense of additional complexity. This thesis provides a partial answer to that question because linear response theory predicts that multiplexing is infeasible, whereas improved models that account for the influence of an external field on the barrier to magnetization reversal predict that it is. This appendix supports this assertion in greater detail than the main text of Section 2.8.

Suppose that SLP is considered at the maximum allowable field amplitude at various frequencies as determined by a constraint such as the $H_0 f$ product, calling it $SLP_c(f)$ for clarity. Section 2.8 argues that applying this kind of constraint results in a unique maximum at some frequency, $SLP_c(f_{max}) = SLP_{c,max}$. When considering the predictions of linear response theory, the possibility of normalizing the $SLP_c(f)$ curve to this value as in Figure 2.8 conveniently allows for many of the constants in Equation D.13 to be neglected, focusing instead on the functional dependence arising from H and f. The dependence may be reduced to the following.

$$SLP_c \propto H_0 L(\xi) f \frac{2\pi f\tau}{1+(2\pi f\tau)^2} \tag{G.1}$$

In order to make general assertions about this dependence without assuming MNP properties, it is possible to approximate the action of the Langevin function. Since operating at the maximum allowable field amplitude will tend to saturate MNPs that heat well, it can be approximated that $L(\xi) \to 1$, only losing generality at the highest frequencies, where loss powers have already fallen below their maximum value. Additionally, consistent with the constraint being applied, a substitution can be made for H_0 in terms of the $H_0 f$ product:

$$H_0 = \frac{5\times 10^9 \mathrm{Am^{-1}s^{-1}}}{f} \to H_0 \propto \frac{1}{f} \tag{G.2}$$

The result is that, for this particular constraint, SLP_c is proportional to $\mathrm{Im}(\tilde{\chi})$.

$$SLP_c \propto \frac{2\pi f\tau}{1+(2\pi f\tau)^2} \tag{G.3}$$

As discussed in Section 2.3, this function will be maximized by selecting MNPs such that the timescale of stochastic reversal corresponds to the frequency of the applied field. This dictates the approach taken to imagine sets of MNPs with distinctly different optimal driving conditions in the context of linear response theory shown in Figure 2.8(a).

An analogous analysis can be made of the results of dynamic hysteresis modeling. This is a numerical model without closed form analytical solutions, but we can momentarily circumvent this by defining a numerical function for the area of a hysteresis loop, $A = A(\xi, \sigma, f)$. Equation E.21 relates A to SLP. Just as in the case of linear response theory, considering selectivity allows for normalization of SLP_c to some maximum value that causes constants to cancel.

$$SLP_c \propto A(\xi, \sigma, f) f \qquad \text{G.4}$$

While the curves for A do not have an analytical form, they do have a shape that can be readily interpreted approximately. They are rounded step functions. Figure G.1(a) shows curves for A assuming constant σ = 40 for two frequencies. Figure G.1(b)-(c) shows how these curves are less sensitive to distributions in σ than distributions in H_k, an important point for materials design.

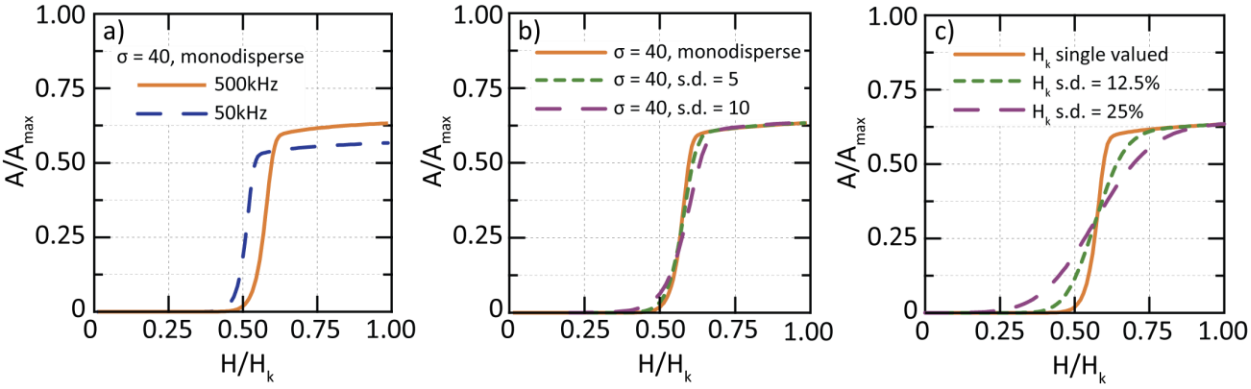

Figure G.1 (a) Area of hysteresis loops produced by a dynamic hysteresis model for uniaxial easy aligned MNPs as described in Appendix E for 50kHz and 500kHz assuming σ = 40. This value of σ ensures that the MNPs are in the "ferromagnetic" regime at both frequencies. (b) The influence of assuming a Gaussian distribution of values in σ is shown. The effect is not very pronounced since σ does not play the same role as in linear response theory. (c) The effect of considering Gaussian distributions in H_k with comparable standard deviations is far more marked, offering a possible explanation for why the onset of plateaus in SLE vs H_0 tend to be more gradual experimentally than is predicted in dynamic hysteresis.

A substitution for ξ can be made that incorporates the $H_0 f$ product constraint in an intuitive way:

$$\xi = \frac{\mu_0 m\ (5 \times 10^9 \text{A m}^{-1}\text{s}^{-1})}{k_B T f} = 2\sigma \frac{(5 \times 10^9 \text{A m}^{-1}\text{s}^{-1})}{H_k f} \qquad \text{G.5}$$

For maximizing SLPs, H_k is less important than the effective coercive field H_c of the squarelike loops, where the onset of the plateau occurs. For $\sigma = 40$, the A versus H curves are relatively independent of frequency, an observation consistent with the experimental results in Section 4.7. The apparent H_c can be related back to H_k as some fraction of its value determined from Figure G.1(a).

$$H_c \approx 0.6 H_k \rightarrow H_k \approx \frac{H_c}{0.6} \quad \text{G.6}$$

For a response favored at 50kHz, the maximum allowable amplitude should be approximately equal to H_c:

$$H_c \approx \frac{5 \times 10^9 \text{A m}^{-1}\text{s}^{-1}}{50\text{kHz}} = 100\text{kA m}^{-1} \quad \text{G.7}$$

And this indicates how ξ should be scaled

$$\xi = 2\sigma \frac{0.6\ (5 \times 10^9 \text{A m}^{-1}\text{s}^{-1})}{(1 \times 10^5 Am) f} = 2\sigma \frac{30\text{kHz}}{f} \quad \text{G.8}$$

The same can be done for a response favored at 500kHz.

$$H_c \approx \frac{5 \times 10^9 \text{A m}^{-1}\text{s}^{-1}}{500\text{kHz}} = 10\text{kA m}^{-1} \quad \text{G.9}$$

$$\xi = 2\sigma \frac{0.6\ (5 \times 10^9 \text{A m}^{-1}\text{s}^{-1})}{(1 \times 10^4 Am) f} = 2\sigma \frac{300\text{kHz}}{f} \quad \text{G.10}$$

Figure 2.8 represents idealized optimization subject to a realistic constraint for both linear response theory and dynamic hysteresis models. Producing maxima for linear response theory unsurprisingly required "tuning" σ. In contrast, dynamic hysteresis permitted the assumption of constant σ, calling instead for appropriate "tuning" of H_k.

Appendix H Justifying the Magnetoquasistatic Approximation for AMF Setups

Some confusion exists in the literature as to the nature of the fields that typically heat MNPs, with some authors going so far as to assert that their MNPs are being heated with "radio waves." Throughout this document, it has been assumed, often tacitly, that it is more appropriate to consider the fields to which samples are exposed as magnetoquasistatic. For instance, this allowed the use of finite element simulations at magnetostatic conditions to be reasonably extrapolated to their operating frequency. A magnetoquasistatic approximation is appropriate when the displacement current term in Maxwell's equations can be safely neglected, giving the field more the character of a magnetostatic field that happens to vary in time rather than the inherently electrodynamic character of a free space wave solution. There are several logical routes to justify this assumption for the setups described in this thesis. The following reasoning is based on Haus pp.71-74,[149] and focuses on estimating the magnitude of the error field, H_{error}, which results from the neglecting the displacement current term.

H will result primarily from the current density J, such that

$$\nabla \times \vec{H} \approx \vec{J} \tag{H.1}$$

Without treating the detailed geometry, it is possible to estimate the magnitude of H as a function of current J and ℓ, a characteristic length scale of the dimensions of the coil, such as diameter of one of the resonant tank circuits described in Chapter 3. The action of the curl can be approximated as $1/\ell$.

$$\frac{H}{\ell} \approx J \quad \Longrightarrow \quad H \approx J\ell \tag{H.2}$$

Estimating H permits a prediction of the order of magnitude of the induced electric field $\vec{E}$.

$$\nabla \times \vec{E} = \frac{\partial \mu_0 \vec{H}}{\partial t} \quad \Longrightarrow \quad \frac{E}{\ell} \approx \frac{\mu_0 H}{\tau} = \frac{\mu_0 J \ell}{\tau} \tag{H.3}$$

Here, τ is a characteristic timescale that estimates the action of the partial derivative in time. It is now possible to estimate the magnitude of the error field that results from neglecting the time varying electric field.

$$\nabla \times \vec{H}_{error} = \frac{\partial \epsilon_0 \vec{E}}{\partial t} \quad \Longrightarrow \quad H_{error} \approx \frac{\mu_0 \epsilon_0 J \ell^3}{\tau^2} \tag{H.4}$$

The absolute magnitude of H_{error} is less useful for the purpose of assessing the quality of the approximation than a fractional error normalized to H, the magnetoquasistatic field.

$$\frac{H_{error}}{H} = \frac{\mu_0 \epsilon_0 \ell^2}{\tau^2} \tag{H.5}$$

Recalling that the speed of light in free space can be written in terms of μ_0 and ϵ_0,

$$c^2 = \frac{1}{\mu_0 \epsilon_0} \tag{H.6}$$

Substituting into Equation H.5,

$$\frac{H_{error}}{H} = \left(\frac{\ell}{c\tau}\right)^2 \tag{H.7}$$

If the error is small, then $H_{error}/H \ll 1$, such that

$$\frac{\ell}{c} \ll \tau \tag{H.8}$$

If the characteristic timescale is taken to be the frequency, f, the comparison can be made in terms of the wavelength of electromagnetic radiation in free space,

$$f\lambda = c \quad \Longrightarrow \quad \frac{\ell}{\lambda} \ll 1 \tag{H.9}$$

For a stringent case, let L be the diameter of the largest AMF coil setup represented in this thesis, ~10cm, and assume a frequency of 10MHz, which is at least an order of magnitude larger than the typical operating frequencies.

$$\frac{10^{-1}\ \mathrm{m}\ * 10^6\ 1/s}{3 \times 10^8\ \mathrm{m/s}} = 0.00\overline{3} \ll 1 \tag{H.10}$$

Clearly the use of the term "alternating magnetic field" is justified, though it should be noted that the magnetostatic simulations employed in this thesis do not account for proximity and skin effects, which do not originate from displacement current and can also significantly impact expected magnetic field profiles in some cases.

Appendix I The Magnetic Field Magnitude of a Gapped Toroidal Electromagnet

Soft ferromagnetic flux paths with an air gap can be described as acting to focus magnetic flux into that gap, although this terminology is somewhat imprecise. Fortunately, the simple case of a gapped toroid lends itself to straightforward analysis and can provide a more complete sense of how this geometry and similar gapped flux paths can lead to strong fields in the gap. A magnetostatic toroidal coil with a small gap of width w and N turns of a wire carrying a current I is shown in Figure I.1.

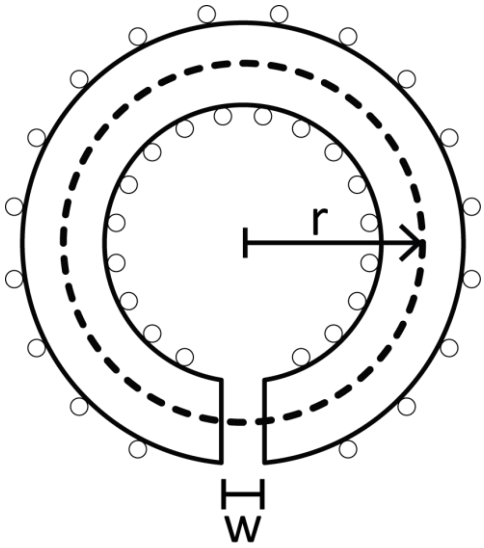

Figure I.1 A sketch of the basic geometry for a gapped toroidal electromagnet with N turns is shown. r corresponds to the radius of a circular Amperian loop passing through the core and the gap. w represents the width of the gap.

The Amperian loop around the circumference of a circular path of radius r that falls within the core relates the magnetic field H to the current I,

$$\oint \vec{H} \cdot \overrightarrow{dl} = NI \approx H_g w + H_c(2\pi r - w) \qquad \text{I.1}$$

Here, H_g is the magnitude of the magnetic field in the gap and H_c is the magnitude of the field in the core, both assumed to be tangential and vary only with r, which is the case for an intact toroid. Magnetic flux is locally conserved, and in the limit of small gap width relative to the cross sectional area of the core A, the fringing behavior of the field in the gap may be neglected such that a statement of flux conservation reads

$$B_g A \approx B_c A \qquad \text{I.2}$$

$$A\mu_0 H_g = A\mu_c H_c \qquad \text{I.3}$$

Here, μ_0 and μ_c are the permeability of free space and the core, respectively. Likewise, $B_g$and B_c are the magnetic flux density in the gap and the core, respectively. This allows for the substitution

$$\frac{\mu_0}{\mu_c} H_g = \frac{1}{\mu_r} H_g = H_c \qquad \text{I.4}$$

Where relative permeability $\mu_r \equiv {}^{\mu_c}/_{\mu_0}$. Substituting Equation I.4 into I.1 and solving for H_g yields

$$H_g = \frac{NI}{w\left[1 + \frac{1}{\mu_r}\left(\frac{2\pi r}{w} - 1\right)\right]} \approx \frac{NI}{w} \qquad \text{I.5}$$

In the limit $\mu_r \gg \left(\frac{2\pi r}{w} - 1\right)$ the dependence reduces to the simple approximation shown in Equation 3.1. For perspective, $\mu_r \approx 2000$ for Ferroxcube 3F3, and a typical electromagnet of the kind used for calorimetry would have $r \approx 2.5\text{cm}$ and $w = 0.75\text{cm}$. Since $2000 \gg 20$, the approximation is clearly applicable.

Appendix J Core Selection for Electromagnets

One significant decision involved in engineering the electromagnets described in Section 3.3 is core material selection. Identifying a material that dissipates minimal waste heat under the required magnetic flux conditions is not only necessary to mitigate the need for active cooling, but more fundamentally is required to justify the use an electromagnet with a core to produce an alternating magnetic field, as indicated by Figure 3.7(a). Numerous core materials and geometries were investigated, with only a small subset of these documented in this thesis. Of the metal powder core materials tested, only Mag. Inc. MPP material was suitable for operation at high fluxes, and even it was limited to a frequency of 15kHz. Other metal powder materials and metal glass cores from several suppliers (e.g. Metglas, Micrometals, Mag. Inc.) were eliminated from consideration based on obvious deficiencies such as reaching only limited amplitudes or producing so much waste heat they melted plastic surfaces beneath them. Ferrite ceramic materials proved most effective and relevant for meeting the $H_0 f$ limit discussed in Section 1.3. Comparisons of various core materials from several manufacturers are made in literature,[82] though these comparisons are typically focused on energy transfer or storage capability at higher frequencies than the range of greatest interest.

Manufacturers of toroidal ferrite ceramic cores include Epcos, Ferroxcube, and Fair-Rite. To assess the available options, a methodical comparison of these materials was undertaken. Toroidal cores with similar dimensions were procured and cut with a diamond saw to incorporate a 7.5mm gap. Two kinds of measurements were made to compare their performance: IR thermography of the cores during operation at comparable fluxes and effective resistance measurements. Figure J.1 summarizes the result. Both types of measurements indicate that the best choice from the options tested is Epcos N87, which exhibits an effective resistance approximately half of the next best material, Ferroxcube 3F3. (Figure J.1(d)).

Although the gapped toroidal geometries served well as electromagnets for the purposes of the experiments described in this thesis, improved geometries are possible. For instance electromagnets made from two E-cores modified to include a gap (Figure J.2) may offer a superior alternative for two main reasons:

1. If an electromagnet is limited by saturation, then ideally the region of highest flux should be near the gap. This will ensure that the highest field magnitudes are reached.
2. A well designed flux path that splits the flux introduced in the center region between two symmetric return paths could, in principle, operate at a lower flux density in the majority of the material comprising the core, reducing dissipated power in the case of AMFs.

A logical extension would be to use a sufficiently large pot core geometry that is gapped in the center. However, it is difficult to find such cores with suitable dimensions and accessibility of the gap is a necessary feature to maintain in order to easily perform experiments.

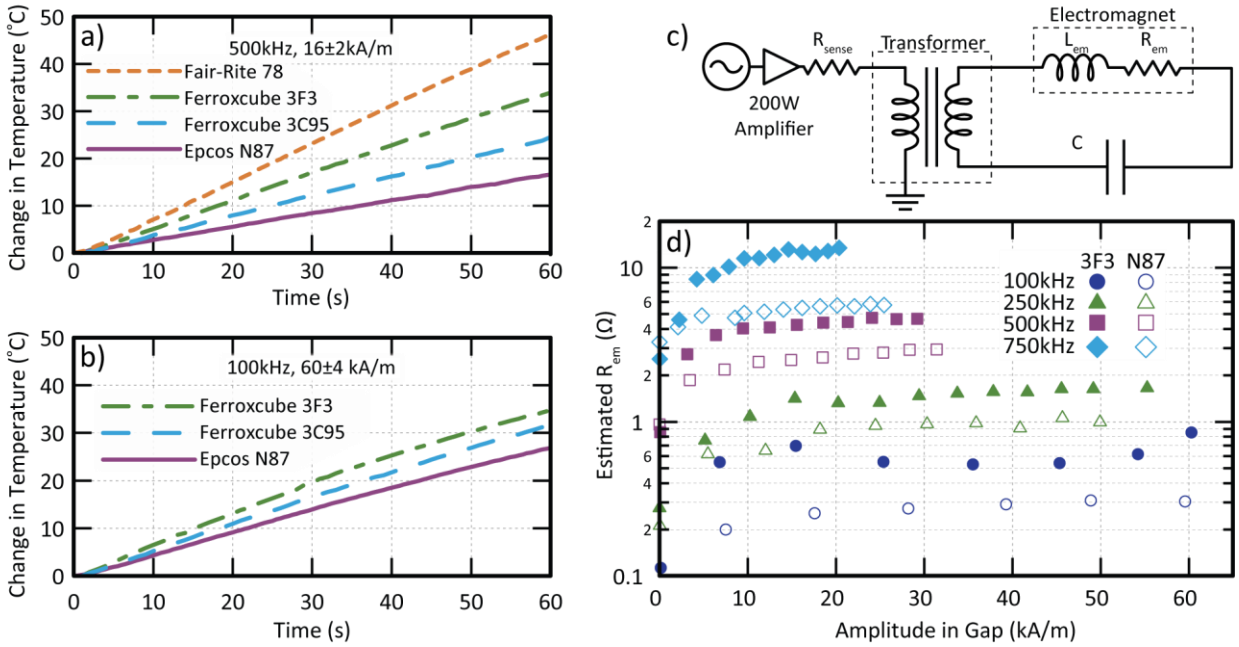

Figure J.1 (a) and (b) Change in temperature versus time is shown for uncooled cores with 7.5mm gaps operated at the indicated conditions in the gap, as determined from IR thermography. (Part numbers: Ferroxcube TX51/32/19-3F3, Ferroxcube TX51/32/19-3C95, Epcos B64290L82X87, Fair-Rite 5978003801.) (c) A schematic of the series resonant circuit powering the electromagnet is shown for reference. Equivalent series resistance of the electromagnet R_{em} is determined from the voltage drop across the sense resistor and known ratio of the transformer. (d) R_{em} is plotted as a function of alternating magnetic field amplitude in the gap for various frequencies for the best performing ferrites.

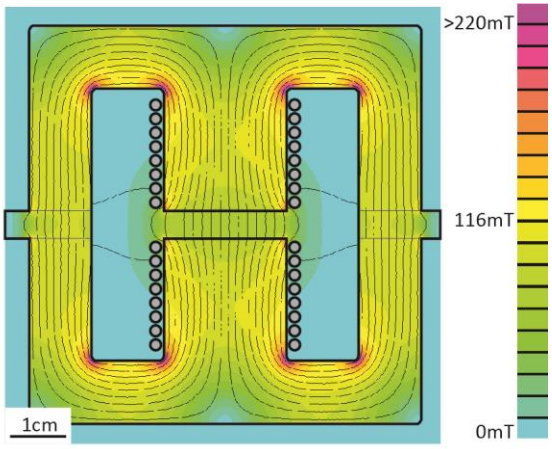

Figure J.2 A magnetostatic finite element simulation of an E-core electromagnet is shown, assuming a current of 20A and the material properties of Epcos N87. Note the highly symmetric distribution of flux in the core and refer to Figure 3.3(a) for a comparison with a gapped toroid.

Appendix K Reasoning for Influence of Coercivity on Expected Interparticle Interactions

Part of the reasoning that suggests the favorability of higher coercivity materials for a preliminary demonstration of magnetothermal multiplexing relates to the expected dependence of interparticle interactions on coercivity. Consider two kinds of MNPs with different coercivity that are constrained to have the same σ values, a supposition fully consistent with Section 2.8 and Appendix G. The energy of magnetic dipole interactions between MNPs is proportional to the square of their moments, such that the ratio of the new energy of interaction U' and old energy of interaction U can be related to the ratio of the new and old individual MNP moments m' and m, respectively.

$$\frac{U'}{U} = \left(\frac{m'}{m}\right)^2 \tag{K.1}$$

m will be proportional to magnetized volume V_m, which can be expressed in terms of σ by rearranging the definition of σ (Equation 2.13).

$$V_m = \frac{\sigma k_B T}{K_{eff}} \tag{K.2}$$

Using this equation and the relationship between magnetization and moment for a uniformly magnetized sphere, $m = M_s V_m$, and recalling that all quantities kept constant will vanish, Equation K.1 can be rewritten.

$$\frac{U'}{U} = \left(\frac{M_s{}' V_m{}'}{M_s V_m}\right)^2 = \left(\frac{M'_s K_{eff}}{K'_{eff} M_s}\right)^2 \tag{K.3}$$

From Equation 2.16,

$$H_k \equiv \frac{2K_{eff}}{\mu_0 M_s} \tag{K.4}$$

This allows Equation K.3 to be rewritten in terms of H_k and H'_k

$$\frac{U'}{U} = \left(\frac{H_k}{H'_k}\right)^2 \tag{K.5}$$

It would usually be inadvisable to conflate the ratio of anisotropy fields with the ratio of coercive fields in the dynamic hysteresis model, especially considering the disparate behavior of MNPs in the superparamagnetic and ferromagnetic regimes. Constraining σ to remain constant or approximately constant in the ferromagnetic regime represents a special case where this may be justified. Under these circumstances, the unperturbed state of the anisotropy barrier tends to trap moments and the instantaneous rate of reversal spikes when the effective barrier reaches some reduced value, as shown in Appendix G. (This is the origin of square-like loops.) Although the coercive field will often be considerably less than H_k, exactly the same barrier is being perturbed

in this thought experiment with constant σ, just with a different scaling factor relating H to ξ. An approximate correlation can therefore be drawn at high field amplitudes, where the hysteresis loops of both MNP types are square like:

$$\frac{U'}{U} \approx \left(\frac{H_c}{H'_c}\right)^2 \qquad \text{K.6}$$

This energy of interaction matters for at least two reasons:

1. It will influence the tendency of the MNPs to aggregate and settle out of solution, with higher energies of interaction driving this behavior.

2. Large interactions between MNPs can dominate reversal behavior rather than intrinsic anisotropy. Obviously this is an undesirable outcome when attempting to engineer MNPs capable of multiplexing that is not strongly dependent on factors such as concentration.

Appendix L Fitting Vibrating Sample Magnetometry Curves for MNP Moments

Using a room temperature magnetometry technique on certain kinds of samples, it is possible to estimate the magnetic moment of the MNPs from the M vs H curve, even without knowing concentration. The suggested approach essentially consists of determining the MNP moment that fits the Langevin function to the low field susceptibility of the sample. The Langevin function is derived from a classical statistical mechanics treatment that considers only the Zeeman energy of moments that are able to assume any angle with respect to the field direction (Figure L.1). The result is as follows:

$$\frac{M}{M_s} = L(\xi) = \coth \xi - \frac{1}{\xi} \qquad \text{L.1}$$

Where

$$\xi \equiv \frac{\mu_0 m H}{k_B T} \qquad \text{L.2}$$

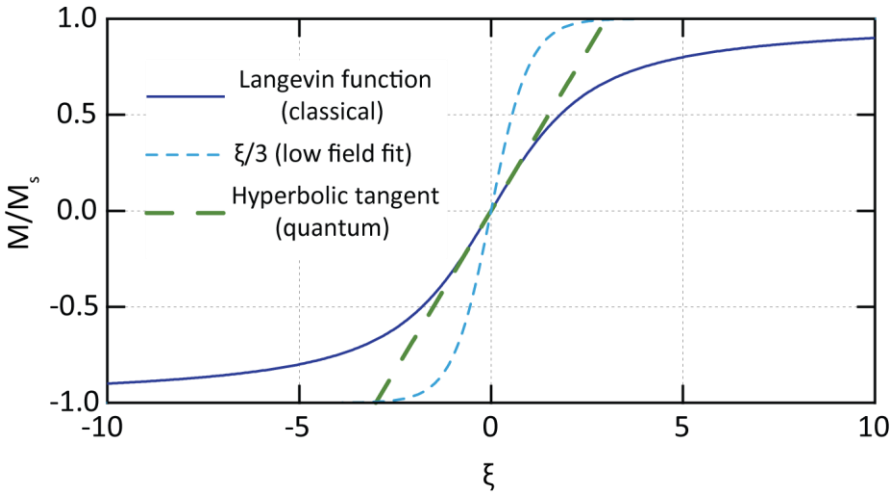

Figure L.1 The Langevin function is shown with its linear fit in the limit $\xi \to 0$, along with the hyperbolic tangent function.

Real MNPs exhibit anisotropy, so the Langevin function is almost never a good fit for an *entire* M vs H curve. Convergence is expected only in the limit of low field amplitudes for randomly oriented anisotropic MNPs.[68] This fit is expected to work well for samples that exhibit the following characteristics:

1) **Dilute and well suspended**
   This minimizes interparticle interactions. If the sample is too dilute, the signal will be small, so a balance must be struck. A typical example is 100uL of 1-2mg/mL Fe for VSM.

2) **Free to physically rotate**

Fitting the linear susceptibility assumes equilibrium. To conduct a measurement in a reasonable timeframe without observing hysteresis, it is best to choose a system known to equilibrate through physical rotation more rapidly than the several seconds required for measurement at each point along the curve.

3) **Reasonably monodisperse**
It is possible to integrate over a known distribution of volumes derived from TEM, but generally the approach being describes is used to produce a rough estimate that will be most accurate with narrow size distributions.

The M vs H curve should be normalized to its saturation value, producing an M/M_s vs. H curve. Note that this curve is independent of concentration, since normalizing the sample moment to its observed saturation value produces the same curve.

The next step is to fit the linear portion of the curve in the vicinity of zero field magnitude. If the curve is not linear, a higher resolution of points may be needed in the vicinity of zero field, especially for MNPs with large moments. If hysteresis is evident, it is not appropriate to apply this fitting technique and it may be worthwhile to consider diluting the sample or pursing strategies that improve suspension of the MNPs.

An estimate of the moment is given by the following equation:

$$m = \frac{3k_B T}{\mu_0}\left(\frac{dM/M_s}{dH}\right)_{H\to 0} \qquad \text{L.3}$$

To justify this assertion, it is possible to find an expression for χ both in terms of a fit to the linear portion of the Langevin function and in terms of experimentally measured quantities, and to set these expressions for χ equal to each other.

Consider the approximate form of the Langevin function in the limit of zero field amplitude, where it is linear.

$$\lim_{\xi\to 0} L(\xi) = \frac{\xi}{3} \quad \therefore \quad \lim_{\xi\to 0} \frac{dL(\xi)}{d\xi} = \frac{1}{3} \qquad \text{L.4}$$

To find χ in terms of m, the chain rule can be used to expand the derivative that defines χ.

$$\chi = \frac{dM}{dH} = \left(\frac{dM}{d\xi}\right)\left(\frac{d\xi}{dH}\right) = \left(M_s \frac{dL(\xi)}{d\xi}\right)\left(\frac{\mu_0 m}{k_B T}\right) = \left(\frac{M_s}{3}\right)\left(\frac{\mu_0 m}{k_B T}\right) \qquad \text{L.5}$$

Various experimental methods permit experimental observation of M vs H, from which χ can be readily determined.

$$\chi = \left(\frac{dM}{dH}\right)_{H\to 0} = M_s\left(\frac{dM/M_s}{dH}\right)_{H\to 0} \qquad \text{L.6}$$

Equating the two expressions for χ,

$$M_s\left(\frac{dM/M_s}{dH}\right)_{H\to 0} = M_s\frac{\mu_0 m}{3k_B T} \quad \text{L.7}$$

Solving for m produces Equation L.3.

Occasionally is it useful to translate the magnitude of the moment into a physical dimension of a uniformly magnetized object with the bulk saturation magnetization. This facilitates comparison to expected moment magnitude. Since the bulk saturation magnetization value should be greater than or equal to the magnetization of MNPs, this dimension derived from the moment should be less than or equal to physical dimensions measured by e.g. TEM.

An example employed during this thesis work for spherical iron oxide MNPs is "magnetic diameter." For a uniformly magnetized object with bulk saturation magnetization,

$$m = M_{s,bulk}V_m \quad \text{L.8}$$

Here, V_m is the magnetized volume, $M_{s,bulk}$ is the bulk saturation magnetization. (E.g., for magnetite, ~92 $\mathrm{Am^2kg^{-1}}$ per mass Fe_3O_4 or ~127 $\mathrm{Am^2kg^{-1}}$ per mass Fe at 290K.)[54] For a sphere,

$$d_m = \sqrt[3]{\frac{6V_m}{\pi}} \quad \text{L.9}$$

Solving Equation L.8 for V_m and substituting Equation L.3 for m,

$$d_m = \sqrt[3]{\frac{6V_m}{\pi}} = \left[\frac{18k_B T}{\pi M_{s,bulk}\mu_0}\left(\frac{dM/M_s}{dH}\right)_{H\to 0}\right]^{\frac{1}{3}} \quad \text{L.10}$$

Appendix M Details of AMF Calorimetry

The description of the techniques used for AMF calorimetry in Sections 4.4 and 4.5 is intended to offer an overview with sufficient detail to reproduce these methods. Additional explanation of some subtleties exceeded the scope of the main text, yet might benefit the keen reader.

1. Some infrared temperature probes require a correction factor when fitting the slope.

Careful study of the data in Figure 4.4(a) will reveal small discreet jumps in the temperature versus time curve. These are not physical, but rather are artifacts of the temperature probe that consistently occur at particular temperature values. Perhaps they result from rounding errors within a digital lookup table or some other mysterious source. Regardless of their origin, they can alter the apparent dT/dt slope, particularly if the change in temperature is sufficiently small or the duration of measurement is sufficiently short that a linear fit would not transect multiple jumps. Fortunately, it is straightforward to correct the slope for these jumps.

Let δT be the size of the jump and ΔT be the temperature difference between jumps (Figure M.1). If the slope were fit within part of a curve that did not transect any of these jumps, the change in temperature would be underestimated in the numerator. A correction factor α that multiplies the apparent slope to arrive at the true slope would be written as follows

$$\alpha = \frac{\Delta T + \delta T}{\Delta T} \qquad \text{M.1}$$

This assumes that the temperature probe is calibrated to match the true temperature on average. In practice, ΔT and δT can be observed either from the data itself or control trials with slow heating. α can be calculated to have a value of about 1.10.

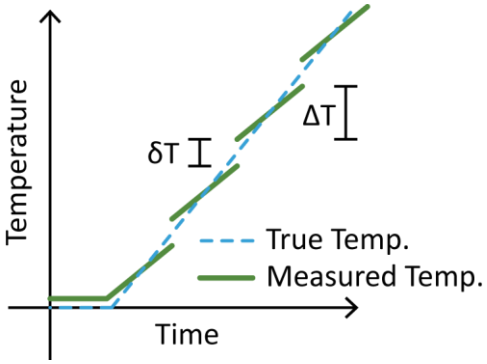

Figure M.1 A sketch illustrates the discreet temperature jumps that are measurement artifacts associated with the infrared temperature probe used for liquid AMF calorimetry samples. The scale of the jumps has been exaggerated for clarity.

2. Differential scanning calorimetry can be used to determine the specific heat of solid samples.

A necessary step in performing calorimetry measurements on solid samples, particularly composites comprised of materials without well-known reference values, is to determine specific heat. One possible method to do this makes use of differential scanning calorimetry (DSC),

which should not be confused with AMF calorimetry. (The term "calorimetry" simply implies that a heat flow is being measured.) In the case of DSC, a sample and an empty sample holder are scanned through a temperature curve at constant rate. The difference in heat flow between the empty holder and the holder with the sample is measured. DSC is perhaps most often used to precisely observe the onset of phase transitions, but it is also possible to measure specific heat.[150]

This can be accomplished by measuring heat flow for a sample of the material of interest with known mass as well as a reference sample, such as sapphire. An example specific heat versus temperature curve determined by this method is shown in Figure M.2. A suitable reference should have slowly varying and well characterized specific heat versus temperature characteristics. For each case,

$$\left(\frac{dQ}{dt}\right)_{sample} = m_{sample}\, C_{sample} \left(\frac{dT}{dt}\right)_{sample} \qquad \text{M.2}$$

And

$$\left(\frac{dQ}{dt}\right)_{sapphire} = m_{sapphire}\, C_{sapphire} \left(\frac{dT}{dt}\right)_{sapphire} \qquad \text{M.3}$$

$\frac{dQ}{dt}$ is heat flow, m is mass, C is specific heat, and $\frac{dT}{dt}$ is the preset temperature ramp rate. Subscripts indicate the relevant sample or standard. Since both curves were measured with the same temperature ramp, a ratio between Equations M.2 and M.3 causes the $\frac{dT}{dt}$ to cancel, leaving

$$C_{sample} = C_{sapphire} \frac{\left(\frac{dQ}{dt}\right)_{sample} m_{sapphire}}{\left(\frac{dQ}{dt}\right)_{sapphire} m_{sample}} \qquad \text{M.4}$$

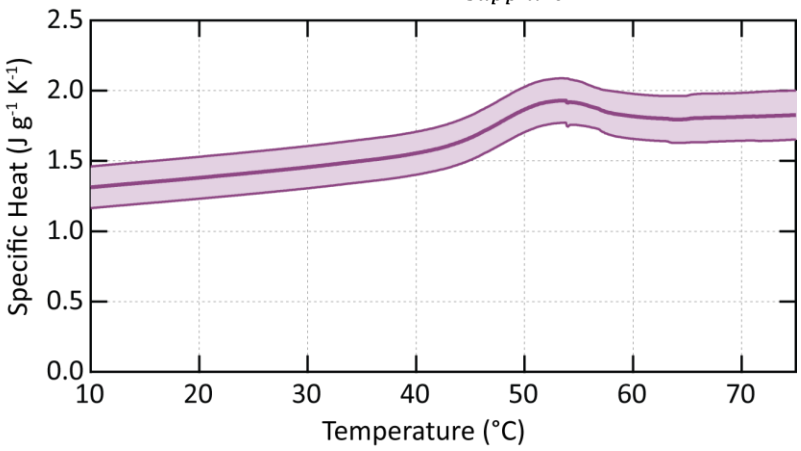

Figure M.2 Specific heat calculated from DSC data is shown for a set of 16 samples of shape memory composites. The bold line represents the average, and the shaded area represents ± one standard deviation. For the purpose of calculating SLP from AMF calorimetry, the average specific was used and assumed to remain approximately constant over the measured temperature range.

Appendix N Solving Bulk Heat Transport Equations for a Heat Dissipating Sphere

In order to clarify the way in which nanoscale heating effects represent a significant departure from the expectations of bulk heat transport equations, it is useful to treat the simple case of an idealized sphere uniformly dissipating heat into its surroundings. (See Figure 6.1.)

$$C_p \frac{\partial T}{\partial t} = -\vec{\nabla} \cdot \overrightarrow{J_Q} \qquad \text{N.1}$$

Here, T is temperature, t is time, C_p is specific heat at constant pressure, and $\overrightarrow{J_Q}$ is heat flux. Heat flux can be expressed in terms of thermal conductivity K and temperature gradient $\vec{\nabla}T$

$$\overrightarrow{J_Q} = -K\vec{\nabla}T \qquad \text{N.2}$$

Substituting,

$$\frac{\partial T}{\partial t} = \frac{K}{C_p}\nabla^2 T \qquad \text{N.3}$$

Assuming a steady state solution, which is predicted to be a reasonable assumption for timescales longer than a few hundred nanoseconds,[110] this reduces to Laplace's equation. Spherical symmetry of the idealized particle will produce a spherically symmetric solution, $T = T(r)$, allowing for further simplification.

$$\nabla^2 T = \frac{1}{r^2}\frac{d}{dr}\left(r^2 \frac{dT}{dr}\right) = 0 \qquad \text{N.4}$$

This is a second order differential equation with the solution

$$T(r) = \frac{A}{r} + B \qquad \text{N.5}$$

Here, A and B are constants determined by the application of appropriate boundary conditions. In the limit of $r \to \infty$, $T \to B$. For an idealized isolated particle, the solution would not be expected to heat far away, such that B can be set equal to the far field temperature and the equation can be rewritten in terms of the change in temperature, ΔT.

$$\Delta T(r) = \frac{A}{r} \qquad \text{N.6}$$

A can be found by setting the heat flux at the surface of the sphere equal to the average heat dissipated per MNP, as estimated by calorimetry measurements and physical dimensions. Applying constant temperature conditions at the surface of the nanoparticle is inadvisable because it does not take the magnitude of the rate dissipated energy per particle into account.

Evaluating $\overrightarrow{J_Q}$ at the boundary,

$$\overrightarrow{J_Q} = -K\vec{\nabla}T\big|_{r=R} = \frac{KA}{R^2}\hat{r} \qquad \text{N.7}$$

The integrated heat flux over surface of the spherical boundary should not exceed the population averaged power dissipation of each nanoparticle (individual particle loss power, IPLP) as estimated by bulk measurements.

$$J_Q 4\pi R^2 = \frac{4\pi}{3}R^3 * (\text{SLP}) * \rho_m = \text{IPLP} \qquad \text{N.8}$$

Time and population averaged IPLP, can estimated from bulk SLP measurements in combination with information about the physical diameter of the particles d in nanometers as follows.

$$\text{IPLP} \approx \text{SLP} * \left(\frac{5.25\text{gFe3O4}}{\text{cm}^3\ \text{Fe3O4}}\right)\left(\frac{0.724\text{gFe}}{1\ \text{g Fe3O4}}\right)\left(\frac{1cm}{10^7 nm}\right)^3 * \frac{\pi}{6}d^3 \qquad \text{N.9}$$

Equations N.7 and N.8 can be combined to solve for A in terms of known quantities. Substituting back into Equation N.6, for $r \geq R$ (i.e. outside the nanoparticle),

$$\Delta T(r) = \frac{R^3(\text{SLP})\rho_m}{3Kr} = \frac{\text{IPLP}}{4\pi Kr} \qquad \text{N.10}$$

As discussed at length in Section 6.1, substituting realistic values predicts that the temperature at the surface of a nanoparticle should not differ significantly from its surroundings.

Appendix O Explaining Clustering Behavior of MNPs Binding to Amyloid β Aggregates

The content of this appendix is closely based on the supplementary materials of Loynachan et al.[133] In that work, it was observed that MNPs tended to occur in clusters when bound to Aβ aggregates. This raised the question of whether these clusters form before binding to the Aβ, casting doubt on their stability in solution, or whether the clusters form during the process of binding to the Aβ. While DLS data contradicted the hypothesis that the magnetic nanoparticles in this study spontaneously form large clusters in solution, a simple model was developed to explain why superparamagnetic nanoparticles might cluster upon binding. The topic is illustrative of the considerations that go into working with MNPs in these kinds of systems, but sufficiently tangential to the points in the main text that it was included in the form of an appendix.

The model begins by assuming a two dimensional grid of available binding sites, arranged in a pattern originating from a thresholded TEM Aβ fibrils, as shown in Figure O.1(a). To prevent overlapping particles, the grid spacing was taken to be the physical diameter d_{phys} of the nanoparticles, 22.0nm (±0.7), measured by TEM. A bound MNP has both a position on the grid and an orientation of its moment. The Zeeman energy of a trial dipole $\vec{m}_t$ in the field of a source dipole $\vec{m}_s$ can be written as follows:

$$U_{Zeeman} = \frac{-\mu_0}{4\pi}\left\{\vec{m}_t \cdot \left[\frac{3(\vec{m}_s \cdot \vec{r})\vec{r}}{|\vec{r}|^5} - \frac{\vec{m}_s}{|\vec{r}|^3}\right]\right\} \quad \text{O.1}$$

Where μ_0 is the permeability of free space (which is essentially unchanged in water) and $\vec{r}$ is the position of the trial dipole relative to $\vec{m}_s$. Relative position $\vec{r}$ is expressible in terms of the grid positions of the trial dipole $\vec{r}_t$and source dipole $\vec{r}_s$:

$$\vec{r} = \vec{r}_t - \vec{r}_s \quad \text{O.2}$$

If the moments of the source and trial dipoles are both equal to $|\vec{m}|$ and the trial dipole is assumed to be locally aligned with the source dipole's field, its minimal energy configuration, then equation 1 reduces to:

$$U_{Zeeman} = \frac{-\mu_0 m^2}{4\pi}\left[\frac{3(\hat{m}_s \cdot \hat{r}) - 1}{|\vec{r}|^3}\right] \quad \text{O.3}$$

In this case, the magnitude of the MNP moments could be estimated in the manner described in Appendix L. The magnetic diameter d_m of the particles used for all data shown in the main text was found to be smaller than the physical diameter, or approximately 18.8nm, assuming a saturation magnetization of magnetite, $4.7 \times 10^5 Am^{-1}$. Dividing U_{Zeeman} by the ambient thermal energy and converting the units of distance on the grid into meters suggests a convenient unitless prefactor ς.

$$\frac{U_{Zeeman}}{k_B T} = \frac{-\mu_0 {M_s}^2}{4\pi k_B T}\left(\frac{\pi {d_m}^3}{6}\right)^2 \left(\frac{1 \text{ grid unit}}{d_{phys}}\right)^3 \left[\frac{3(\hat{m}_s \cdot \hat{r}) - 1}{|\vec{r}|^3}\right] \quad \text{O.4}$$

$$\varsigma = \frac{\mu_0 {M_s}^2}{4\pi k_B T}\left(\frac{\pi {d_m}^3}{6}\right)^2 \left(\frac{1 \text{ grid unit}}{d_{phys}}\right)^3 \quad \text{O.5}$$

Suppose that an ensemble of MNPs is built up one by one, with particles remaining irreversibly bound to the sites where they are added. These MNPs could be added randomly to available sites, as in the example shown in Figure O.1(b). Alternatively, the pseudorandom addition of MNPs can be weighted according to a scheme motivated by statistical mechanics in order to take into account the relative influence of magnetic interaction versus thermal fluctuation. The total energy of a test dipole at any grid site $U_{i,j}$ is just a sum of the dipole interactions with all the particles presently on the grid. If the weighting scheme assumed for the addition of particles follows a Maxwell distribution, then the probability of adding a new particle to an available site $p_{i,j}$ is given by:

$$p_{i,j} = \frac{\exp\left(-\frac{U_{i,j}}{k_B T}\right)}{Q} \quad \text{O.6}$$

Where Q is a partition function.

$$Q = \sum_{i,j}^{all\ available\ i,j} \exp\left(-\frac{U_{i,j}}{k_B T}\right) \quad \text{O.7}$$

Figures O.1(b), (d), and (f) show that the energy of magnetic interaction predicted for sites close to particles on the grid is attractive and of comparable or larger magnitude to the ambient thermal energy. (I.e., for sites close to particles, $U_{i,j}/k_B T \leq -1$).

One additional nuance to consider is the influence of the particles upon the orientation of the moments of their neighbors. Neighbors will exert torques upon each other and thereby influence the overall profile of the magnetic field. In a real system, one can imagine that the orientation of moments would fluctuate, but exhibit correlation with the local field. Rather than account for this complexity directly, it is possible to consider two comparatively simple limiting cases: randomized moments with no correlation and fully correlated moments.

In order to consider the second case, an algorithm was employed that began by randomly sampling different moment orientations to coarsely determine a minimal energy configuration. After this, the moments are finely relaxed into alignment with the local field. Both the uncorrelated and fully correlated cases lead to clustering when magnetic interactions are taken into account, as shown in Figures O.1(c) and (e). Assuming interaction with uncorrelated and randomized moments, a single cluster was typically formed, and hence a lower median

interparticle distance was predicted (Figure O.1(c)). In the case of fully correlated moments, the formation of chains was predicted, demonstrated quantitatively by comparing the distance of each particle from the line defined by the two particles previously added, or "chain departure distance" (Figure O.1(e)**)**. That these chains tend to form horizontally and vertically is likely an artifact, a consequence of the fact that the mesh is rectangular and the distance between grid points is minimal in these directions. The correlated moments often form multiple clusters because the superposition of dipole fields from a chain of aligned dipoles results in large magnitudes at the ends, and comparatively small magnitudes near the middle of the chain. This, in combination with the possibility that a site at the end of an existing chain might be unavailable for binding, provides an explanation for the frequent occurrence of multiple clusters in the simulations with correlated moments.

It should be emphasized that this model is highly simplified in order to illustrate that magnetic interaction could plausibly account for clustering behavior of ideally superparamagnetic particles as they bind to Aβ, even though they are stably suspended in solution. Though relevant features are physically motivated, it is not intended to be fully rigorous. For instance, the presence of binding sites would be determined by protein structure, rather than assuming the whole Aβ surface is available. Binding would likely be reversible, which could lead to additional mechanisms for clustering. A more computationally intensive approach might model MNPs as undergoing simultaneous 3D weighted random walk in solution, with each step influenced by both binding and magnetic interactions.

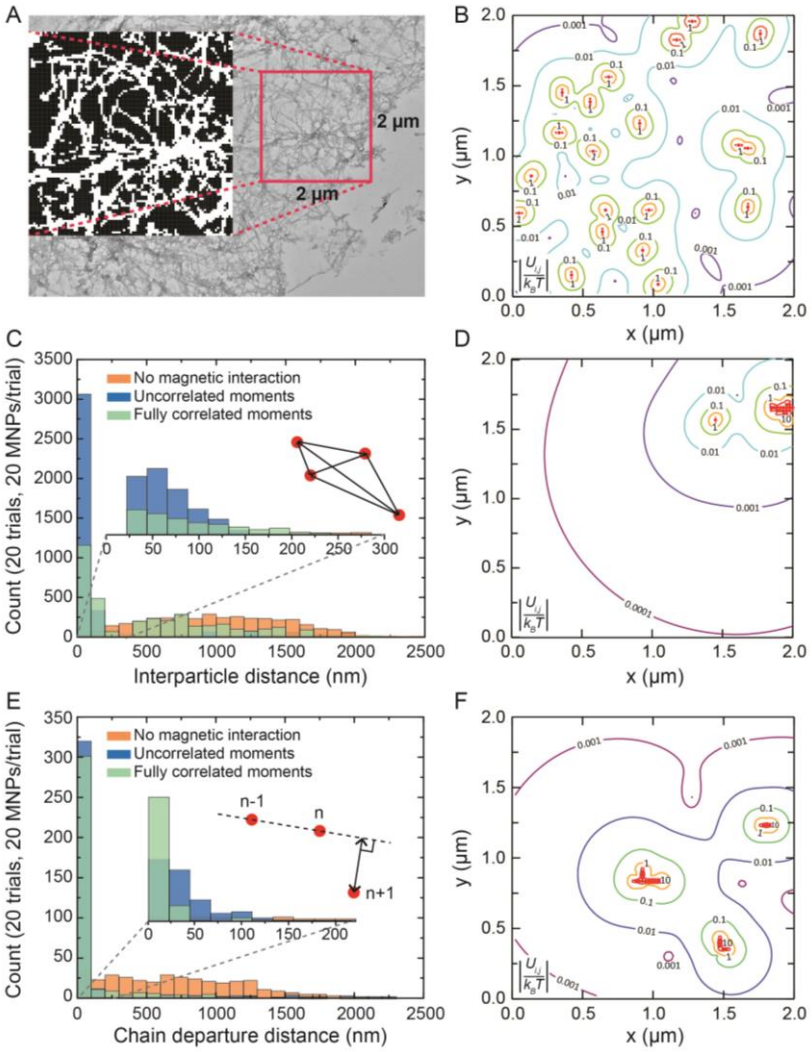

Figure O.1 (a) A TEM image and the corresponding grid (inset), produced by setting thresholds for Aβ fibrils. White pixels denote available binding sites. (b) A representative example of a contour plot of the energy of a test dipole locally aligned with the field and normalized to ambient thermal energy is shown for a distribution of pseudorandomly placed MNPs on the grid in (a). (c) A histogram illustrates the distribution of interparticle distances (inset graphic: black lines connecting the MNPs shown with red circles) for MNPs placed onto the Aβ grid with different kinds of interaction. Inset: The histogram with 22 nm bins resolves the distribution of distances < 300 nm. (d) A representative contour plot illustrates clustering of MNPs on an Aβ grid in the presence of magnetic interaction with uncorrelated moments. (e) A histogram illustrating the distribution of chain-departure distances (inset graphic: black arrow orthogonally connecting an MNP to a dashed line between MNPs forming a chain) for MNPs with different types of interaction. Taking a local correlation between moments in the MNP ensemble into account yields a strong preference for the formation of chains. Inset: The histogram with 22 nm bins resolves the distribution of distances < 220 nm. (f) An example contour plot similar to the ones in (b) and (d) illustrates chain formation of MNPs on Aβ grid in the presence of magnetic interaction with moments fully correlated with the local magnetic field. From Loynachan et al.[133]

References

1. G. Deuschl, C. Schade-Brittinger, P. Krack, J. Volkmann, H. Schäfer, K. Bötzel, C. Daniels, A. Deutschländer, U. Dillmann, W. Eisner, D. Gruber, W. Hamel, J. Herzog, R. Hilker, S. Klebe, M. Kloß, J. Koy, M. Krause, A. Kupsch, D. Lorenz, S. Lorenzl, H. M. Mehdorn, J. R. Moringlane, W. Oertel, M. O. Pinsker, H. Reichmann, A. Reuß, G.-H. Schneider, A. Schnitzler, U. Steude, V. Sturm, L. Timmermann, V. Tronnier, T. Trottenberg, L. Wojtecki, E. Wolf, W. Poewe, and J. Voges, *New England Journal of Medicine* **355** (9), 896-908 (2006).
2. H. S. Mayberg, A. M. Lozano, V. Voon, H. E. McNeely, D. Seminowicz, C. Hamani, J. M. Schwalb, and S. H. Kennedy, *Neuron* **45** (5), 651-660 (2005).
3. B. Rosin, M. Slovik, R. Mitelman, M. Rivlin-Etzion, S. N. Haber, Z. Israel, E. Vaadia, and H. Bergman, *Neuron* **72** (2), 370-384 (2011).
4. M. I. Hariz, *Movement Disorders* **17** (S3), S162-S166 (2002).
5. O. Yizhar, L. E. Fenno, T. J. Davidson, M. Mogri, and K. Deisseroth, *Neuron* **71** (1), 9-34 (2011).
6. Y. Wang and L. Guo, *Frontiers in Neuroscience* **10**, 69 (2016).
7. R. Chen, A. Canales, and P. Anikeeva, *Nature Reviews Materials* **2**, 16093 (2017).
8. C. P. Richter, A. I. Matic, J. D. Wells, E. D. Jansen, and J. T. Walsh, *Laser & Photonics Reviews* **5** (1), 68-80 (2011).
9. Y. Tufail, A. Matyushov, N. Baldwin, M. L. Tauchmann, J. Georges, A. Yoshihiro, S. I. H. Tillery and W. J. Tyler, *Neuron* **66** (5), 681-694 (2010).
10. Z. Manoli, N. Grossman, and T. Samaras, presented at the 2012 Annual International Conference of the IEEE Engineering in Medicine and Biology Society, 2012.
11. M. A. Wheeler, C. J. Smith, M. Ottolini, B. S. Barker, A. M. Purohit, R. M. Grippo, R. P. Gaykema, A. J. Spano, M. P. Beenhakker, S. Kucenas, M. K. Patel, C. D. Deppmann, and A. D. Guler, Nat Neurosci **19** (5), 756-761 (2016).
12. H. Huang, S. Delikanli, H. Zeng, D. M. Ferkey, and A. Pralle, *Nature Nanotechnology* **5** (8), 602-606 (2010).
13. T. Perera, M. S. George, G. Grammer, P. G. Janicak, A. Pascual-Leone, and T. S. Wirecki, *Brain Stimulation* **9** (3), 336-346 (2016).
14. E. M. Wassermann and S. H. Lisanby, *Clinical Neurophysiology* **112** (8), 1367-1377 (2001).
15. X. Long, J. Ye, D. Zhao, and S.-J. Zhang, *Science Bulletin* **60** (24), 2107-2119 (2015).
16. A. Kargol, G. Caruntu, and L. Malkinski, *Biomedical applications of multiferroic nanoparticles*, INTECH Open Access Publisher (2012).
17. R. Guduru, P. Liang, J. Hong, A. Rodzinski, A. Hadjikhani, J. Horstmyer, E. Levister, and S. Khizroev, *Nanomedicine* **10** (13), 2051-2061 (2015).
18. K. Yue, R. Guduru, J. Hong, P. Liang, M. Nair, and S. Khizroev, *PLOS ONE* **7** (9), e44040 (2012).
19. S. A. Stanley, J. E. Gagner, S. Damanpour, M. Yoshida, J. S. Dordick, and J. M. Friedman, *Science* **336** (6081), 604-608 (2012).
20. R. Chen, G. Romero, M. G. Christiansen, A. Mohr, and P. Anikeeva, *Science* **347** (6229), 1477-1480 (2015).
21. R. K. Gilchrist, R. Medal, W. D. Shorey, R. C. Hanselman, J. C. Parrott, and C. B. Taylor, *Annals of Surgery* **146** (4), 596-606 (1957).

22. Q. A. Pankhurst, J. Connolly, S. K. Jones, and J. Dobson, *Journal of Physics D: Applied Physics* **36** (13), R167 (2003).
23. Q. A. Pankhurst, N. T. K. Thanh, S. K. Jones, and J. Dobson, *Journal of Physics D: Applied Physics* **42** (22), 224001 (2009).
24. I. A. Brezovich, W. J. Atkinson, and D. P. Chakraborty, *Medical Physics* **11** (2), 145-152 (1984).
25. T. K. Jain, M. K. Reddy, M. A. Morales, D. L. Leslie-Pelecky, and V. Labhasetwar, *Molecular Pharmaceutics* **5** (2), 316-327 (2008).
26. M. Johannsen, U. Gneveckow, L. Eckelt, A. Feussner, N. Waldöfner, R. Scholz, S. Deger, P. Wust, S. A. Loening, and A. Jordan, *International Journal of Hyperthermia* **21** (7), 637-647 (2005).
27. K. Maier-Hauff, R. Rothe, R. Scholz, U. Gneveckow, P. Wust, B. Thiesen, A. Feussner, A. von Deimling, N. Waldoefner, R. Felix, and A. Jordan, *Journal of Neuro-Oncology* **81** (1), 53-60 (2007).
28. D. Silvio and H. Rudolf, *Nanotechnology* **25** (45), 452001 (2014).
29. A. Senyei, K. Widder, and G. Czerlinski, *Journal of Applied Physics* **49** (6), 3578-3583 (1978).
30. C. Gosse and V. Croquette, *Biophysical Journal* **82** (6), 3314-3329 (2002).
31. J. J. Abbott, K. E. Peyer, M. C. Lagomarsino, L. Zhang, L. Dong, I. K. Kaliakatsos, and B. J. Nelson, *The International Journal of Robotics Research* **28** (11-12), 1434-1447 (2009).
32. A. Servant, F. Qiu, M. Mazza, K. Kostarelos, and B. J. Nelson, *Advanced Materials* **27** (19), 2981-2988 (2015).
33. J. L. Kirschvink, A. Kobayashi-Kirschvink, and B. J. Woodford, *Proceedings of the National Academy of Sciences* **89** (16), 7683-7687 (1992).
34. J. Dobson, *Nature Nanotechnology* **3** (3), 139-143 (2008).
35. M. J. Caterina, M. A. Schumacher, M. Tominaga, T. A. Rosen, J. D. Levine, and D. Julius, *Nature* **389** (6653), 816-824 (1997).
36. R. Munshi, S. Parker, I. Castellanos-Rubio and A. Pralle, *Biophysical Journal* **112** (3), 286a (2017).
37. S. A. Stanley, J. Sauer, R. S. Kane, J. S. Dordick, and J. M. Friedman, *Nature Medicine* **21** (1), 92-98 (2015).
38. S. A. Stanley, L. Kelly, K. N. Latcha, S. F. Schmidt, X. Yu, A. R. Nectow, J. Sauer, J. P. Dyke, J. S. Dordick, and J. M. Friedman, *Nature* **531** (7596), 647-650 (2016).
39. M. Meister, *eLife* **5**, e17210 (2016).
40. K. Pang, H. You, Y. Chen, P. Chu, M. Hu, J. Shen, W. Guo, C. Xie, and B. Lu, *Frontiers in Neural Circuits* **11** (11) (2017).
41. L. Pauling and C. D. Coryell, *Proceedings of the National Academy of Sciences of the United States of America* **22** (4), 210-216 (1936).
42. N. T. Gorham, T. G. S. Pierre, W. Chua-Anusorn, and G. M. Parkinson, *Journal of Applied Physics* **103** (5), 054302 (2008).
43. F. Brem, A. M. Hirt, M. Winklhofer, K. Frei, Y. Yonekawa, H.-G. Wieser, and J. Dobson, *Journal of The Royal Society Interface* **3** (11), 833-841 (2006).
44. R. Hergt and S. Dutz, *Journal of Magnetism and Magnetic Materials* **311** (1), 187-192 (2007).
45. P. A. Bottomley and E. R. Andrew, *Physics in Medicine and Biology* **23** (4), 630 (1978).

46. J. I. Rodriguez and S. B. Leeb, *IEEE Transactions on Power Electronics* **21** (6), 1607-1617 (2006).
47. R. Mohr, K. Kratz, T. Weigel, M. Lucka-Gabor, M. Moneke, and A. Lendlein, *Proceedings of the National Academy of Sciences of the United States of America* **103** (10), 3540-3545 (2006).
48. S. H. Noh, W. Na, J. T. Jang, J. H. Lee, E. J. Lee, S. H. Moon, Y. Lim, J. S. Shin, and J. Cheon, *Nano Letters* **12** (7), 3716-3721 (2012).
49. M. Kallumadil, M. Tada, T. Nakagawa, M. Abe, P. Southern, and Q. A. Pankhurst, *Journal of Magnetism and Magnetic Materials* **321** (10), 1509-1513 (2009).
50. G. T. Landi and A. F. Bakuzis, *Journal of Applied Physics* **111** (8), 083915 (2012).
51. M. G. Christiansen, A. W. Senko, R. Chen, G. Romero, and P. Anikeeva, *Applied Physics Letters* **104** (21), 213103 (2014).
52. L. Néel, Reviews of Modern Physics **25** (1), 293-295 (1953).
53. C. A. Ross, Annual Review of Materials Research **31** (1), 203-235 (2001).
54. R. C. O'Handley, *Modern magnetic materials : principles and applications*. (Wiley, New York, 2000).
55. D. Peddis, M. V. Mansilla, S. Mørup, C. Cannas, A. Musinu, G. Piccaluga, F. D'Orazio, F. Lucari, and D. Fiorani, *The Journal of Physical Chemistry B* **112** (29), 8507-8513 (2008).
56. W. Williams and D. J. Dunlop, *Journal of Geophysical Research: Solid Earth* **100** (B3), 3859-3871 (1995).
57. K. M. Krishnan, *IEEE Transactions on Magnetics* **46** (7), 2523-2558 (2010).
58. W. Wernsdorfer, E. B. Orozco, K. Hasselbach, A. Benoit, B. Barbara, N. Demoncy, A. Loiseau, H. Pascard, and D. Mailly, *Physical Review Letters* **78** (9), 1791-1794 (1997).
59. M. Tachiki, *Progress of Theoretical Physics* **23** (6), 1055-1072 (1960).
60. N. A. Usov and J. M. Barandiarán, *Journal of Applied Physics* **112** (5), 053915 (2012).
61. R. Yanes, O. Chubykalo-Fesenko, H. Kachkachi, D. A. Garanin, R. Evans, and R. W. Chantrell, *Physical Review B* **76** (6), 064416 (2007).
62. L. Neél, *Annales de Geophysique* **5** (2), 99-136 (1949).
63. R. E. Rosensweig, *Journal of Magnetism and Magnetic Materials* **252**, 370-374 (2002).
64. Y. L. Raikher and V. I. Stepanov, *Journal of Magnetism and Magnetic Materials* **320** (21), 2692-2695 (2008).
65. M. Varón, M. Beleggia, T. Kasama, R. J. Harrison, R. E. Dunin-Borkowski, V. F. Puntes and C. Frandsen, *Scientific Reports* **3**, 1234 (2013).
66. R. E. Dunin-Borkowski, T. Kasama, A. Wei, S. L. Tripp, M. J. Hÿtch, E. Snoeck, R. J. Harrison, and A. Putnis, *Microscopy Research and Technique* **64** (5-6), 390-402 (2004).
67. W. Kauzmann, *Reviews of Modern Physics* **14** (1), 12-44 (1942).
68. J. Carrey, B. Mehdaoui, and M. Respaud, *Journal of Applied Physics* **109** (8), 083921 (2011).
69. W. F. B. Jr., *Journal of Applied Physics* **30** (4), S130-S132 (1959).
70. W. F. Brown, *Physical Review* **130** (5), 1677-1686 (1963).
71. N. A. Usov, *Journal of Applied Physics* **107** (12), 123909 (2010).
72. N. A. Usov and O. N. Serebryakova, *AIP Advances* **6** (7), 075315 (2016).
73. S. Ruta, R. Chantrell, and O. Hovorka, *Scientific Reports* **5**, 9090 (2015).
74. R. P. Tan, J. Carrey, and M. Respaud, *Physical Review B* **90** (21), 214421 (2014).

75. E. Garaio, J. M. Collantes, J. A. Garcia, F. Plazaola, S. Mornet, F. Couillaud, and O. Sandre, *Journal of Magnetism and Magnetic Materials* **368**, 432-437 (2014).
76. V. Connord, B. Mehdaoui, R. P. Tan, J. Carrey, and M. Respaud, *Review of Scientific Instruments* **85** (9), 093904 (2014).
77. E. C. Stoner and E. P. Wohlfarth, *Philosophical Transactions of the Royal Society of London. Series A, Mathematical and Physical Sciences* **240** (826), 599-642 (1948).
78. J. P. Fortin, C. Wilhelm, J. Servais, C. Ménager, J. C. Bacri, and F. Gazeau, *Journal of the American Chemical Society* **129** (9), 2628-2635 (2007).
79. C. R. Thomas, D. P. Ferris, J. H. Lee, E. Choi, M. H. Cho, E. S. Kim, J. F. Stoddart, J. S. Shin, J. Cheon and J. I. Zink, *Journal of the American Chemical Society* **132** (31), 10623-10625 (2010).
80. U. Gneveckow, A. Jordan, R. Scholz, V. Brüß, N. Waldöfner, J. Ricke, A. Feussner, B. Hildebrandt, B. Rau and P. Wust, *Medical Physics* **31** (6), 1444-1451 (2004).
81. D. J. Griffiths, *Introduction to electrodynamics*, 3rd ed. (Prentice Hall, Upper Saddle River, N.J., 1999).
82. A. J. Hanson, J. A. Belk, S. Lim, D. J. Perreault, and C. R. Sullivan, presented at the 2015 IEEE Energy Conversion Congress and Exposition (2015).
83. L.-M. Lacroix, J. Carrey and M. Respaud, *Review of Scientific Instruments* **79** (9), 093909 (2008).
84. A. Rand, *IEEE Transactions on Component Parts* **10** (1), 31-35 (1963).
85. D. J. Perreault, J. Hu, J. M. Rivas, Y. Han, O. Leitermann, R. C. N. Pilawa-Podgurski, A. Sagneri, and C. R. Sullivan, presented at the IEEE Applied Power Electronics Conference and Exposition, (2009).
86. C. R. Sullivan, B. A. Reese, A. L. F. Stein, and P. A. Kyaw, presented at the International Symposium on 3D Power Electronics Integration and Manufacturing, (2016).
87. C. R. Sullivan, *IEEE Transactions on Power Electronics* **14** (2), 283-291 (1999).
88. C. P. Steinmetz, *Transactions of the American Institute of Electrical Engineers* **IX** (1), 1-64 (1892).
89. American Radio Relay League, in *The ARRL Handbook for Radio Communications No. 19*, ARRL, Newington, CT, (2013).
90. R. Chen, M. G. Christiansen, A. Sourakov, A. Mohr, Y. Matsumoto, S. Okada, A. Jasanoff, and P. Anikeeva, *Nano Letters* **16** (2), 1345-1351 (2016).
91. R. Chen, M. G. Christiansen, and P. Anikeeva, *ACS Nano* **7** (10), 8990-9000 (2013).
92. S. Schuerle, J. S. Dudani, M. G. Christiansen, P. Anikeeva, and S. N. Bhatia, *Nano Letters* **16** (10), 6303-6310 (2016).
93. A. A. Fallah, S. S. Saei-Dehkordi, A. Nematollahi, and T. Jafari, *Microchemical Journal* **98** (2), 275-279 (2011).
94. S. A. Gudoshnikov, B. Y. Liubimov, and N. A. Usov, *AIP Advances* **2** (1), 012143 (2012).
95. G. Romero, M. G. Christiansen, L. Stocche Barbosa, F. Garcia, and P. Anikeeva, *Advanced Functional Materials* **26** (35), 6471-6478 (2016).
96. T. W. Chen, T. J. Wardill, Y. Sun, S. R. Pulver, S. L. Renninger, A. Baohan, E. R. Schreiter, R. A. Kerr, M. B. Orger, V. Jayaraman, L. L. Looger, K. Svoboda, and D. S. Kim, *Nature* **499** (7458), 295-300 (2013).
97. S. P. Hunt, A. Pini, and G. Evan, *Nature* **328** (6131), 632-634 (1987).
98. M. Sheng and M. E. Greenberg, *Neuron* **4** (4), 477-485 (1990).

99. Z.-D. Deng, S. H. Lisanby, and A. V. Peterchev, *Brain Stimulation* **6** (1), 1-13 (2013).
100. M. Marcus, M. Karni, K. Baranes, I. Levy, N. Alon, S. Margel, and O. Shefi, *Journal of Nanobiotechnology* **14** (1), 37 (2016).
101. J. W. Jeong, G. Shin, S. I. Park, K. J. Yu, L. Xu, and J. A. Rogers, *Neuron* **86** (1), 175-186 (2015).
102. G. Lind, C. E. Linsmeier, and J. Schouenborg, *Scientific Reports* **3**, 2942 (2013).
103. F. K. H. van Landeghem, K. Maier-Hauff, A. Jordan, K. T. Hoffmann, U. Gneveckow, R. Scholz, B. Thiesen, W. Brück, and A. von Deimling, *Biomaterials* **30** (1), 52-57 (2009).
104. M. G. White, M. Emery, D. Nonner, and J. N. Barrett, *Journal of Neurochemistry* **87** (4), 958-968 (2003).
105. C. Liu, H. Qin, and P. Mather, *Journal of Materials Chemistry* **17** (16), 1543-1558 (2007).
106. K. Yu, Q. Ge, and H. J. Qi, *Nature Communications* **5**, 3066 (2014).
107. C. M. Yakacki, N. S. Satarkar, K. Gall, R. Likos, and J. Z. Hilt, *Journal of Applied Polymer Science* **112** (5), 3166-3176 (2009).
108. Q. Ge, A. H. Sakhaei, H. Lee, C. K. Dunn, N. X. Fang, and M. L. Dunn, *Scientific Reports* **6**, 31110 (2016).
109. J. I. Rodriguez and S. B. Leeb, *IEEE Transactions on Industrial Electronics* **57** (9), 3095-3108 (2010).
110. P. Keblinski, D. G. Cahill, A. Bodapati, C. R. Sullivan, and T. A. Taton, *Journal of Applied Physics* **100** (5), 054305 (2006).
111. S. R. Milner and A. P. Chattock, *Philosophical Magazine Series 5* **48** (290), 46-64 (1899).
112. A. Riedinger, P. Guardia, A. Curcio, M. A. Garcia, R. Cingolani, L. Manna, and T. Pellegrino, *Nano Letters* **13** (6), 2399-2406 (2013).
113. J. Dong and J. I. Zink, *ACS Nano* **8** (5), 5199-5207 (2014).
114. M. Honda, Y. Saito, N. I. Smith, K. Fujita, and S. Kawata, *Optics Express* **19** (13), 12375-12383 (2011).
115. G. Chen, *Journal of Nanoparticle Research* **2** (2), 199-204 (2000).
116. Y. Terada, H. Masuda, and T. Watanabe, *Journal of Natural Products* **78** (8), 1937-1941 (2015).
117. L. R. Desnoyers, O. Vasiljeva, J. H. Richardson, A. Yang, E. E. M. Menendez, T. W. Liang, C. Wong, P. H. Bessette, K. Kamath, S. J. Moore, J. G. Sagert, D. R. Hostetter, F. Han, J. Gee, J. Flandez, K. Markham, M. Nguyen, M. Krimm, K. R. Wong, S. Liu, P. S. Daugherty, J. W. West, and H. B. Lowman, *Science Translational Medicine* **5** (207), 207ra144-207ra144 (2013).
118. H. Hua, M. Li, T. Luo, Y. Yin and Y. Jiang, *Cellular and Molecular Life Sciences* **68** (23), 3853-3868 (2011).
119. K. Y. Choi, M. Swierczewska, S. Lee and X. Chen, *Theranostics* **2** (2), 156-178 (2012).
120. G. A. Kwong, G. von Maltzahn, G. Murugappan, O. Abudayyeh, S. Mo, I. A. Papayannopoulos, D. Y. Sverdlov, S. B. Liu, A. D. Warren, Y. Popov, D. Schuppan, and S. N. Bhatia, *Nature Biotechnology* **31** (1), 63-70 (2013).
121. M. A. Miller, L. Barkal, K. Jeng, A. Herrlich, M. Moss, L. G. Griffith, and D. A. Lauffenburger, *Integrative Biology* **3** (4), 422-438 (2011).
122. J. S. Dudani, P. K. Jain, G. A. Kwong, K. R. Stevens, and S. N. Bhatia, *ACS Nano* **9** (12), 11708-11717 (2015).

123. P. Yingchoncharoen, D. S. Kalinowski, and D. R. Richardson, *Pharmacological Reviews* **68** (3), 701-787 (2016).
124. V. Torchilin, *Advanced Drug Delivery Reviews* **63** (3), 131-135 (2011).
125. G. A. Kwong, J. S. Dudani, E. Carrodeguas, E. V. Mazumdar, S. M. Zekavat, and S. N. Bhatia, *Proceedings of the National Academy of Sciences* **112** (41), 12627-12632 (2015).
126. E. Amstad, J. Kohlbrecher, E. Müller, T. Schweizer, M. Textor, and E. Reimhult, *Nano Letters* **11** (4), 1664-1670 (2011).
127. W. T. Al-Jamal and K. Kostarelos, *Accounts of Chemical Research* **44** (10), 1094-1104 (2011).
128. J. Hardy and D. J. Selkoe, *Science* **297** (5580), 353-356 (2002).
129. M. J. Kogan, N. G. Bastus, R. Amigo, D. Grillo-Bosch, E. Araya, A. Turiel, A. Labarta, E. Giralt, and V. F. Puntes, *Nano Letters* **6** (1), 110-115 (2006).
130. M. Li, X. Yang, J. Ren, K. Qu, and X. Qu, *Advanced Materials* **24** (13), 1722-1728 (2012).
131. C. E. Tedford, S. DeLapp, S. Jacques, and J. Anders, *Lasers in Surgery and Medicine* **47** (5), 466-466 (2015).
132. A. Vander Vorst, A. Rosen and Y. Kotsuka, *RF/Microwave Interaction with Biological Tissues*, John Wiley & Sons, (2006).
133. C. N. Loynachan, G. Romero, M. G. Christiansen, R. Chen, R. Ellison, T. T. O'Malley, U. P. Froriep, D. M. Walsh, and P. Anikeeva, *Advanced Healthcare Materials* **4** (14), 2100-2109 (2015).
134. C. Soto, E. M. Sigurdsson, L. Morelli, R. Asok Kumar, E. M. Castano, and B. Frangione, *Nature Medicine* **4** (7), 822-826 (1998).
135. D. Brambilla, R. Verpillot, B. Le Droumaguet, J. Nicolas, M. Taverna, J. Kóňa, B. Lettiero, S. H. Hashemi, L. De Kimpe, M. Canovi, M. Gobbi, V. Nicolas, W. Scheper, S. M. Moghimi, I. Tvaroška, P. Couvreur, and K. Andrieux, *ACS Nano* **6** (7), 5897-5908 (2012).
136. M. Bourhim, M. Kruzel, T. Srikrishnan and T. Nicotera, *Journal of Neuroscience Methods* **160** (2), 264-268 (2007).
137. A. Lomakin, D. S. Chung, G. B. Benedek, D. A. Kirschner and D. B. Teplow, *Proceedings of the National Academy of Sciences* **93** (3), 1125-1129 (1996).
138. R. Paparcone and M. J. Buehler, *Biomaterials* **32** (13), 3367-3374 (2011).
139. C. Haass and D. J. Selkoe, *Nature Reviews Molecular Cell Biology* **8** (2), 101-112 (2007).
140. D. G. Le Couteur, S. Hunter, and C. Brayne, *BMJ* **355** (2016).
141. H. F. Iaccarino, A. C. Singer, A. J. Martorell, A. Rudenko, F. Gao, T. Z. Gillingham, H. Mathys, J. Seo, O. Kritskiy, F. Abdurrob, C. Adaikkan, R. G. Canter, R. Rueda, E. N. Brown, E. S. Boyden, and L.-H. Tsai, *Nature* **540** (7632), 230-235 (2016).
142. S. E. Lee, D. Y. Sasaki, Y. Park, R. Xu, J. S. Brennan, M. J. Bissell, and L. P. Lee, *ACS Nano* **6** (9), 7770 (2012).
143. H. De Puig, A. C. Rius, D. Flemister, S. H. Baxamusa, and K. Hamad-Schifferli, *PLOS ONE* **8** (7), e68511 (2013).
144. G. Salazar-Alvarez, J. Qin, V. Šepelák, I. Bergmann, M. Vasilakaki, K. N. Trohidou, J. D. Ardisson, W. A. A. Macedo, M. Mikhaylova, M. Muhammed, M. D. Baró, and J. Nogués, *Journal of the American Chemical Society* **130** (40), 13234-13239 (2008).
145. Y. Suzuki, G. Hu, R. B. van Dover, and R. J. Cava, *Journal of Magnetism and Magnetic Materials* **191** (1–2), 1-8 (1999).

146. W. F. Brown and A. H. Morrish, *Physical Review* **105** (4), 1198-1201 (1957).
147. M. Beleggia, M. D. Graef and Y. T. Millev, *Journal of Physics D: Applied Physics* **39** (5), 891 (2006).
148. K. Segall, D. Schult, U. Ray, and T. Ohsumi, arXiv:1110.0172 (2011).
149. H. A. Haus and J. R. Melcher, *Electromagnetic Fields and Energy,* Prentice Hall, Englewood Cliffs, N.J., (1989).
150. K. L. Ramakumar, M. K. Saxena and S. B. Deb, *Journal of Thermal Analysis and Calorimetry* **66** (2), 387-397 (2001).